catalysts

MDPI

Review

Advanced Two-Dimensional Heterojunction Photocatalysts of Stoichiometric and Non-Stoichiometric Bismuth Oxyhalides with Graphitic Carbon Nitride for Sustainable Energy and Environmental Applications

Kishore Sridharan [1,*], Sulakshana Shenoy [2], S. Girish Kumar [3], Chiaki Terashima [4], Akira Fujishima [4] and Sudhagar Pitchaimuthu [5,*]

[1] Department of Nanoscience and Technology, University of Calicut, Thenhipalam 673635, India
[2] Department of Physics, National Institute of Technology Karnataka, Mangalore 575025, India; shenoy26sulakshana@gmail.com
[3] Department of Chemistry, School of Engineering & Technology, CMR University, Bangalore 562149, India; girichem@yahoo.co.in
[4] Photocatalysis International Research Center, Research Institute for Science and Technology, Tokyo University of Science, 2641 Yamazaki, Noda Chiba 278-8510, Japan; terashima@rs.tus.ac.jp (C.T.); fujishima_akira@rs.tus.ac.jp (A.F.)
[5] Multifunctional Photocatalyst and Coatings Group, SPECIFIC, Materials Research Centre, Faculty of Science and Engineering, Swansea University, Swansea SA1 8EN, UK
* Correspondence: sridharankishore@uoc.ac.in or sridharankishore@gmail.com (K.S.); s.pitchaimuthu@swansea.ac.uk or vedichi@gmail.com (S.P.)

Citation: Sridharan, K.; Shenoy, S.; Kumar, S.G.; Terashima, C.; Fujishima, A.; Pitchaimuthu, S. Advanced Two-Dimensional Heterojunction Photocatalysts of Stoichiometric and Non-Stoichiometric Bismuth Oxyhalides with Graphitic Carbon Nitride for Sustainable Energy and Environmental Applications. *Catalysts* **2021**, *11*, 426. https://doi.org/10.3390/catal11040426

Academic Editor: Juan Matos Lale

Received: 9 March 2021
Accepted: 23 March 2021
Published: 26 March 2021

Abstract: Semiconductor-based photocatalysis has been identified as an encouraging approach for solving the two main challenging problems, viz., remedying our polluted environment and the generation of sustainable chemical energy. Stoichiometric and non-stoichiometric bismuth oxyhalides (BiOX and $Bi_xO_yX_z$ where X = Cl, Br, and I) are a relatively new class of semiconductors that have attracted considerable interest for photocatalysis applications due to attributes, viz., high stability, suitable band structure, modifiable energy bandgap and two-dimensional layered structure capable of generating an internal electric field. Recently, the construction of heterojunction photocatalysts, especially 2D/2D systems, has convincingly drawn momentous attention practicably owing to the productive influence of having two dissimilar layered semiconductors in face-to-face contact with each other. This review has systematically summarized the recent progress on the 2D/2D heterojunction constructed between BiOX/$Bi_xO_yX_z$ with graphitic carbon nitride (g-C_3N_4). The band structure of individual components, various fabrication methods, different strategies developed for improving the photocatalytic performance and their applications in the degradation of various organic contaminants, hydrogen (H_2) evolution, carbon dioxide (CO_2) reduction, nitrogen (N_2) fixation and the organic synthesis of clean chemicals are summarized. The perspectives and plausible opportunities for developing high performance BiOX/$Bi_xO_yX_z$-g-C_3N_4 heterojunction photocatalysts are also discussed.

Keywords: 2D materials; photocatalysis; heterojunction; bismuth oxyhalides; graphitic carbon nitride

1. Introduction

Excessive demand for pharmaceutical, personal care, agricultural and industrial products driven by the continued growth of the world population has inevitably escalated the discharge of organic contaminants into the environment [1]. The steadily increasing concentration of organic contaminants primarily originating from pharmaceutical and personal care products in municipal wastewaters of many urban cities globally is making microorganisms resistant to drugs [2]. Undoubtedly, these organic contaminants pose a huge threat to the environment and human health as they have demonstrated severe ecological risk for mutagenesis, teratogenesis and carcinogenicity [3]. Therefore, in addition to finding sustainable solutions to our global energy crisis and eliminating the steadily increasing CO_2 concentration from the environment, the removal of these organic contaminants with high chemical stability is another highly challenging task [4]. Several methods based on chemical [5] and biological [6] techniques and advanced oxidation processes [7] have been employed for the complete removal of organic contaminants from wastewater. However, almost all strategies failed to achieve complete degradation, and the search for a green, efficient and economically viable technology continued. In 1972, pioneering work reported by Fujishima and Honda revealed that UV light irradiated on the surface of a TiO_2 electrode generated free radicals for the decomposition of water into hydrogen and oxygen. Later on, it was revealed that the photogenerated free radicals emanating from semiconductors under UV/Visible light excitation could also cleavage the chemical bonds in the molecular organic contaminants adsorbed on their surfaces [8]. In this regard, heterogeneous semiconductor photocatalysis—categorized as another form of advanced oxidation process—has received an overwhelming research interest as a “one-step solution” for addressing the energy and environmental issues, viz., the generation of hydrogen gas through light-water splitting reaction, the reduction of CO_2 into hydrocarbons and to completely break down organic contaminants through redox reactions involving the radical species [9]. Despite nanostructured TiO_2 being a robust and chemically stable semiconductor, its wide bandgap energy (3.2 eV) demands UV light for its excitation. Since the visible light is predominant in the solar spectrum and with UV light being insignificant (just ~4%), researchers swiftly moved to utilize nanostructured semiconductors with a narrower bandgap energy (such as CdS, Fe_2O_3, WO_3, etc.) for efficiently utilizing the inexhaustible sunlight energy [10,11].

Since the discovery of graphene, semiconductors with 2D layered structures have greatly influenced the researchers to study them for applications in photocatalysis due to their unique sheet-like morphology with one-dimensionally confined electrons producing exceptional physio-chemical, optical and electronic properties [12]. In addition to the ease of fabrication, other interesting features of 2D semiconductors exclusively for photocatalytic applications are their large specific surface area with many photoactive sites and customizable thickness leading to easy adjustments to the bandgap energy and light absorption efficiency. Further, the atomically thin 2D layered morphology enables strong in-plane bond formation, facilitating easy heterostructure construction (on substrates or with other 2D semiconductors through weak van der Waals interaction) and enhancing the rate of the photocatalytic reactions due to the shortened transport path [13].

Among the various 2D semiconductors for photocatalysis applications, bismuth oxyhalides (referred to hereafter as BiOX, where X = Cl, Br and I)—a group of V-VI-VII ternary compounds with stoichiometric form—have become the prime choice for researchers owing to their nontoxicity, layered morphology, unique crystal structure, suitable band structure, variable bandgap energy and excellent chemical stability ensuring corrosion resistance in the solution medium for long term operations [14]. The stoichiometric BiOX possessing tetragonal matlockite polymorph (PbFCl-type; space group—$P4/nmm$) crystallize into layered structures consisting of patterned [X-Bi-O-Bi-X] slices stacked together by the nonbonding van der Waals interaction through the halogen atoms along the c-axis, as depicted in Figure 1. In each [X-Bi-O-Bi-X] layer, the central Bi atom is surrounded by four oxygen and four halogen atoms, generating an asymmetric decahedral geometry [15]. The open crystalline structure, indirect bandgap, strong covalent bonding combined with weak interlayer van der Waals interaction, and excellent electrical, optical and mechanical properties are the features that endow BiOX as a promising candidate for light induced redox reactions [16]. However, poor light absorption, restricted utilization and limited chemical stability are some of the shortcomings of BiOX.

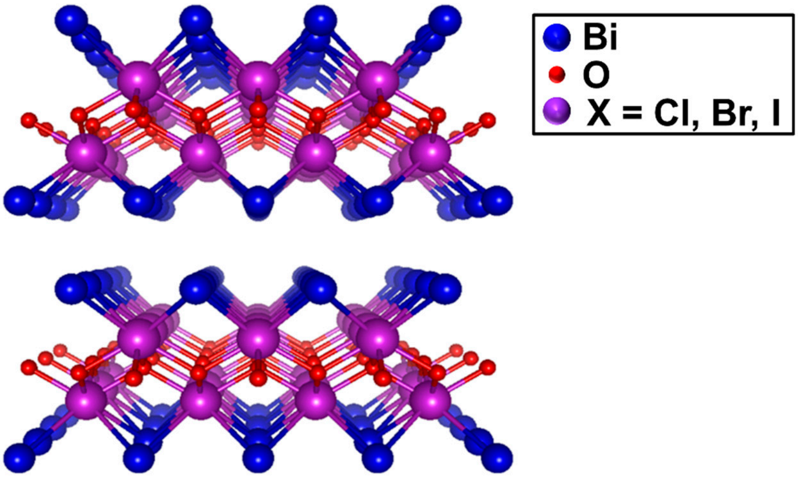

Figure 1. Crystal structure of the BiOX systems (space group *P*4/*nmm*, D_{4h} symmetry) with stoichiometric X-Bi-O-Bi-X Bi-layers stacked along the c axis. Bismuth, oxygen, and halide ions are denoted by purple, red and blue spheres, respectively.

On the other hand, bismuth rich-bismuth oxyhalides (referred to hereafter as $Bi_xO_yX_z$) with non-stoichiometric form also have a layered structure similar to BiOX, with strong covalent bonding and weak interlayer van der Walls interactions. Generally, the band structure of a semiconductor is governed by its chemical components to a great extent. In non-stoichiometric $Bi_xO_yX_z$, the replacement of the halogen atoms in its lattice correspondingly led to modified band structure and subsequently the optical absorption edge and band redox potentials [17]. Most importantly, the negative conduction band positions of $Bi_xO_yX_z$ facilitate its widespread utilization for photocatalytic applications [18].

Graphitic carbon nitride (g-C_3N_4) is another exquisite 2D semiconductor that has been flourishing in the recent years for applications in photocatalysis due to its tri-s-triazine ring structure, appealing electronic band structure, medium bandgap (2.7 eV), and excellent chemical and thermal stability [19]. In addition, the earth-abundant carbon and nitrogen elements in g-C_3N_4 can be easily prepared via one-step polymerization of abundantly available inexpensive nitrogen-rich precursors, such as urea, thiourea, melamine, cyanamide and dicyandiamide [20,21]. Nevertheless, pristine g-C_3N_4 also suffers from shortcomings such as high excitation energy, low charge carrier mobility, the rapid recombination of photogenerated charge carriers, and narrow visible light absorption efficiency [22].

Thus, integrating BiOX/$Bi_xO_yX_z$ with g-C_3N_4 would be an ideal strategy to overcome many of the demerits associated with individual components. The 2D layered structures of both BiOX/$Bi_xO_yX_z$ and g-C_3N_4 conveniently promote the construction of a heterojunction and, furthermore, the favourable band energy between them can facilitate enhanced photocatalytic performance [23–29]. Several review articles on single component 2D semiconductor photocatalysts concentrating primarily on BiOX, $Bi_xO_yX_z$ and g-C_3N_4 have been published [15,30–58]. Nonetheless, a review article accounting the progress of heterojunction photocatalysts based on BiOX and $Bi_xO_yX_z$ with g-C_3N_4 is rarely reported. Since there is a consistent upsurge in the research trend on BiOX based photocatalysts as evidenced from the literature survey presented in Figure 2, a review article is needed to fill the gaps and to account the recent progress. Therefore, in this review, we have presented a summary on the band structure of $Bi_xO_yX_z$ and have furnished information on the various methods of coupling BiOX/Bi_xO_yX and g-C_3N_4 to fabricate heterojunction photocatalysts for organic contaminant degradation, H_2 generation, CO_2 reduction, N_2 fixation and organic synthesis applications. Further, the various strategies for improving the performance of g-C_3N_4-BiOX/$Bi_xO_yX_z$ heterojunction photocatalysts, viz., the creation of defects, the role of facets, integration with other semiconductors, metals and carbon materials are discussed.

Additionally, the future prospects of BiOX/$Bi_xO_yX_z$-g-C_3N_4 heterojunction photocatalysts for broader energy and environmental applications are deliberated.

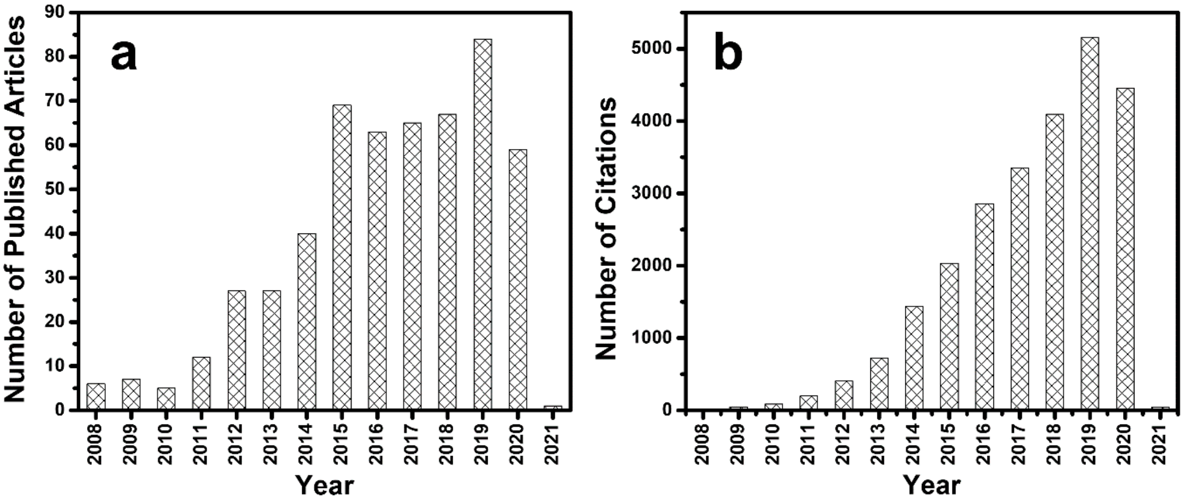

Figure 2. (**a**) Number of articles published and (**b**) number of citations since 2008 with topic keywords "BiOX" and "photocatal*" adapted from the Web of Science, dated 17 November 2020.

2. Electronic Band Structure of BiOX, $Bi_xO_yX_z$ and g-C_3N_4

The band structure of the material is the crucial parameter that dictates the light absorption capacity, charge carrier dynamics and generation of free radicals. In the case of BiOX, O 2p and X *n*p states (n = 3, 4 and 5 for X = Cl, Br, and I, respectively) constitute the valance band minimum (VBM), while the conduction band maximum (CBM) is derived from Bi 6s and the Bi 6p states. The largely dispersed Bi 6s orbital facilitates the mobility of photoinduced holes in the VB (valence band) and is beneficial for the oxidation reaction. The energy bandgap values and the redox potentials of BiOX are vastly related to the atomic numbers of X and the composition of the layered structure [59]. Therefore, the optical absorption in BiOX can be tailored via varying the halogen species or Bi/X ratios. Increasing the atomic number of X leads to a change in the colour and bandgap energy of BiOX from white (BiOCl, 3.2 eV) to yellow (BiOBr, 2.7 eV) and red (BiOI, 1.7 eV), thus maximizing their light absorption capacities [60]. The open crystalline structure has a layered Sillen–Aurivillius related oxide structure composed of [Bi_2O_2] layers sandwiched between two slabs of [X] ions, and the electrostatic potential difference between the slabs generates a static internal electric field (IEF). The static IEF in BiOX can effectively split and transit the photogenerated electrons and holes [61–63]. However, BiOX as a photocatalyst could be employed for the degradation of organic pollutants alone as its positive CB (conduction band) potential restricts it from being used for other photocatalytic applications such as H_2 generation, CO_2 reduction, N_2 fixation and organic synthesis.

On the other hand, non-stoichiometric $Bi_xO_yX_z$ with increased Bi content are reported to promote the reduction power of photogenerated electrons and increase the thermodynamic force for initiating many reduction reactions that were impossible to be carried out using BiOX [64,65]. For instance, compared with BiOX, the changes in the Bi, O, and X proportions result in the variation of orbital hybridization and uplifting of the bottom of the CB, leading to the water splitting for H_2 generation as was reported in $Bi_4O_{5 \times 2}$ (X = Br and I) [66,67]. In addition to H_2 generation, the increased CB also promoted photocatalytic molecular oxygen activation in $Bi_{24}O_{31}Cl_{10}$. Further, the Bi-rich $Bi_xO_yX_z$ possesses enhanced light-harvesting ability that is attributed to the modulated band structure, thus breaking the bottleneck of limited photoabsorption caused from the wide bandgap energy of BiOCl and BiOBr [68]. The higher photon absorption efficiency of $Bi_xO_yX_z$ in comparison to BiOX induces greater electric field intensity, which in turn leads to large dipole moment. The larger dipole moment and wider interlayer spacing in $Bi_xO_yX_z$ boosted by the large polarization force and polarization space lead to increased IEF, which in turn enhances the separation efficiency of the photogenerated charge carriers.

Electronic band structure, redox levels of the CB and VB and the bandgap energy of g-C_3N_4 were studied both theoretically and experimentally. Theoretical calculations estimated the bandgap energy of the melem molecule, polymeric melon and fully condensed g-C_3N_4 to be 3.5, 2.6 and 2.1 eV, respectively [69–71]. The bandgap energy value of 2.6 eV calculated for polymeric melon was consistent with the experimentally measured value of 2.7 eV for defect containing bulk g-C_3N_4 [70]. The CBM and VBM positions for g-C_3N_4 estimated through the density functional theory were -1.12 and $+1.57$ eV, respectively. Interestingly, the experimental investigations through the valence band X-ray photoelectron spectroscopy confirmed the VBM position of g-C_3N_4 at +1.53 eV, which was almost consistent with the theoretical calculations [72]. Therefore, the position of the CBM (-1.12 eV) is predicted to be satisfactory for H_2 generation, while that of the VBM provides a thermodynamic driving force for O_2 evolution reaction. Wavefunction studies revealed that the VB and CB of g-C_3N_4 serving as independent sites for the oxidation and reduction reactions during water splitting are mainly driven by the nitrogen P_z orbitals and carbon P_z orbitals, respectively. Further, the redox potential levels of water calculated by ab initio thermodynamics indicated that both the reduction and oxidation level of water splitting are located within the bandgap of g-C_3N_4 [69]. Another theory using the many-body Green's function reported that lone pair electrons of nitrogen atoms are mainly responsible for the formation of the VB and electronic structure [20,73]. Additionally, it was proposed that the N 2p orbital overlapping the C 2p orbital mainly contributes to the VB and CB of g-C_3N_4, respectively [74]. As observed from Figure 3, the CB position of g-C_3N_4 and many of the $Bi_xO_yX_z$ are suitable for photocatalytic H_2 generation, CO_2 reduction, N_2 fixation and molecular oxygen activation in addition to their potential to be utilized in the degradation of organic pollutants. Further, it is evident from Figure 3 that the VB and CB levels of g-C_3N_4 match well with those of BiOX and $Bi_xO_yX_z$ for the fabrication of efficient 2D/2D heterojunction photocatalysts.

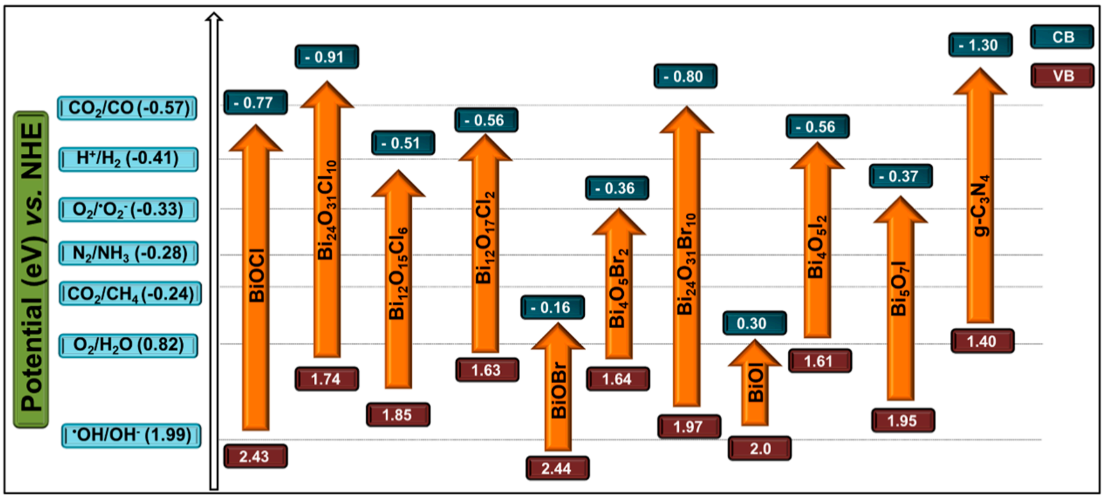

Figure 3. Conduction and valence band (CB and VB) positions of g-C_3N_4, BiOX, and some of the $Bi_xO_yX_z$ photocatalysts *vs.* Normal Hydrogen Electrode (NHE) at pH = 7. The redox potentials of different chemical reactions are compared in this figure.

3. Fabrication of BiOX/$Bi_xO_yX_z$-g-C_3N_4 Heterojunction Photocatalysts

Fabrication is a significant step involved in tailoring the band structure of photocatalysts due to its dependence on the chemical composition. Morphology, shape, size and surface area are some of the critical parameters that play a determinant role in the adsorption properties and photocatalytic activity. Benefiting from the large specific surface area, 2D semiconductors can provide abundant surface active sites. More importantly, the greatly reduced thickness of 2D semiconductors relative to bulk counterparts shortens the bulk carrier diffusion distance and improves the charge separation. Further, the surface charge separation efficiency is enhanced by the creation of surface defects such as oxygen vacancies during the fabrication of the 2D semiconductors.

The typical bismuth metal precursors utilized for synthesizing BiOX and $Bi_xO_yX_z$ are $Bi(NO_3)_3 \cdot 5H_2O$, $NaBiO_3 \cdot 2H_2O$, Bi_2O_3, $BiCl_3$ and BiI_3, while the halogen precursors include KX, NaX, HX, CTAX (X = Cl, Br or I) and ionic liquids containing halogen elements. Various solution based fabrication techniques such as the electrostatic self-assembly approach, the hydrothermal method, the ionic liquid-assisted method, the impregnation method, the solid-phase calcination step, the solvothermal method, precipitation, the reflux process and the ultrasound-assisted water bath technique are used in the synthesis of BiOX and $Bi_xO_yX_z$. On the other hand, the precursors used for synthesizing g-C_3N_4 through the most typical thermal polycondensation method are urea, thiourea, melamine and dicyandiamide. The fabrication of g-C_3N_4-BiOX/$Bi_xO_yX_z$ as 2D-2D heterojunction photocatalysts is usually achieved by growing BiOX/$Bi_xO_yX_z$ on the surface of pre-synthesized g-C_3N_4. An overview of the various synthetic methods and the corresponding growth mechanism is presented in detail.

3.1. In Situ Self-Assembly

The effective use of electrostatic forces in the self-assembly and fabrication of nanostructures is gaining significance owing to their flexibility to work at room temperature and also due to their ability to offer rigid interface among the integrated components. For example, Yang et al. synthesized BiOBr/g-C_3N_4 composite through the in situ self-assembly process based on electrostatic interaction between the precursors followed by their precipitation. In a typical process, pre-synthesized g-C_3N_4 was protonated by treating it with HCl solution for converting its surface charge from negative to positive. The protonated g-C_3N_4 was then added to KBr solution such that the Br^- gets attracted to its surface and subsequently undergoes a precipitation reaction to form BiOBr with the addition of $Bi(NO_3)_3 \bullet 5H_2O$ solution [62]. Therefore, the BiOBr layer was favourably formed on the positively charged surface of g-C_3N_4 and led to the formation of a tightly bound 2D-2D semiconductor heterojunction. Similarly, a p-n heterojunction between flower-like BiOI sheets and g-C_3N_4 nanoparticles was constructed through an electrostatic self-assembly of g-C_3N_4 nanoparticles, wherein the zeta potential of BiOI sheets was −11.1 mV and that of the g-C_3N_4 nanoparticles was +21.5 mV [75]. The measured values of zeta potential clearly indicated that the heterojunction formed between them was via the electrostatic self-assembly process.

3.2. Hydrothermal and Solvothermal Synthesis

Hydrothermal synthesis refers to process of heating water above its boiling point in a sealed reaction vessel to create supercritical fluid that in turn facilitates the precipitation or crystallization of inorganic materials under auto-generated pressure. The hydrothermal synthesis of nanostructured materials is similar to the processes governing the formation of minerals under the earth's crust that have been experimentally studied by geologists. The hydrothermal process can be used for dissolving and recrystallizing a substance that is poorly soluble or insoluble under normal conditions. Typically, an aqueous mixture of precursors sealed in a stainless steel autoclave heated above the boiling point of water results in the single-step production of highly crystalline materials due to the synergistic effect of high temperature and pressure [76]. The merits of hydrothermal synthesis are the enhanced crystallinity of synthesized materials without the need for further calcination, and easy control of the morphology and phase composition by controlling the temperature and reaction time. Under hydrothermal conditions, reactants enter the solution in the form of ions and are adsorbed, decomposed and desorbed at the growth interface before crystallizing. Solvothermal synthesis is analogous to the hydrothermal synthesis process, except for the fact that water is replaced by an organic solvent such as ethanol, ethylene glycol, etc. Adjusting the thermodynamic and kinetic parameters of the solvothermal synthesis reaction such as the concentration of the reactant precursors, reaction time, pH and temperature aids in controlling the size, shape, uniformity, dimensionality, phase and facets of the inorganic materials [77]. Therefore, the hydrothermal and solvothermal reactions can possibly ensure the intimate interface contact between BiOX/$Bi_xO_yX_z$ and g-C_3N_4 for promoting the rapid transport of photogenerated charge carriers across the interface.

Xiao et al. reported the synthesis of thirteen kinds of BiOX and $Bi_xO_yX_z$, viz., BiOI, $Bi_4O_5I_2$, $Bi_7O_9I_3$, Bi_5O_7I, BiOBr, $Bi_4O_5Br_2$, $Bi_{24}O_{31}Br_{10}$, Bi_3O_4Br, BiOCl, $Bi_{12}O_{15}Cl_6$, $Bi_{24}O_{31}Cl_{10}$, Bi_3O_4Cl, and $Bi_{12}O_{17}Cl_2$ through a general one-pot hydrothermal route by reacting different compositions of Bi_2O_3 and KX (X = Cl, Br and I) with nitric acid, and it was the first of its kind [78]. Since then, hydrothermal synthesis for the fabrication of BiOX and $Bi_xO_yX_z$ with various morphologies such as microspheres, microflowers, and microdisks (3D hierarchical structures) was achieved and comprised of three main growth steps: (i) the creation of BiOX nuclei, (ii) the growth of 2D nanosheets through the dissolution-renucleation process, and (iii) the formation of 3D nanostructures from the oriented attachment of 2D nanosheets under the influence of an electrostatic multipole field [79,80]. The hydrothermal method with L-lysine as a bio-template was employed in the fabrication of BiOBr/g-C_3N_4 semiconductor heterojunction. Flake-like g-C_3N_4 was pre-synthesized by the thermal polycondensation of melamine followed by sonochemical treatment in NH_4Cl solution and subsequent sintering at 550 °C. BiOBr microspheres with various mass ratios (5, 10, 15, 20 and 25%) were grown in situ on flake-like g-C_3N_4 under hydrothermal conditions with $Bi(NO_3)_3 \bullet 5H_2O$, NaBr as precursors and L-lysine as the bio-template. Experimental investigation using TEM revealed that BiOBr microspheres synthesized with L-lysine as the template exhibited a loose structure with a larger percentage of exposed nanosheets that enhanced the amount of active sites for the degradation of organic pollutants in comparison to those synthesized without L-lysine [81]. Similarly, the hierarchical nanostructures of $Bi_xO_yX_z$ synthesized hydro/solvothermally with interconnected porous networks were reported to accelerate molecular diffusion/transport, enhance the overall light utilization efficiency, possess a large accessible surface area and provide better permeability, which could not only furnish adequate active adsorption sites and photocatalytic reaction sites, but also contributed to uniformly distributing the active sites in the fabricated photocatalysts [82]. The solvothermal method employed for synthesizing Bi_5O_7Br nanotubes using oleylamine as the solvent exhibited good visible light absorption and created oxygen vacancies on the surface that were beneficial for the stable photoreduction process [83]. Liu et al. reported the solvothermal synthesis of a 3D hierarchical structure of g-C_3N_4@Bi/BiOBr with ternary heterojunction employing ethylene glycol as the solvent and reducing agent, which exhibited notably high photocatalytic activity for degrading organic pollutants [84]. Similarly, ethylene glycol assisted solvothermal synthesis reported by Ji et al. for the fabrication of ultrathin $Bi_4O_5Br_2$ nanosheets dispersed over layered g-C_3N_4 also exhibited higher photocatalytic activity for ciprofloxacin decomposition under visible light irradiation [85]. Another report on solvothermal synthesis was reported for the synthesis of g-C_3N_4/I^{3-}-BiOI heterojunction semiconductor using self-stabilized I_3^-/I^- as a redox mediator that efficiently strengthened the interaction between porous g-C_3N_4 and ultrathin BiOI, thereby enhancing their photocatalytic activity in CH_3SH oxidation [63].

3.3. *Ionic Liquid-Assited Method*

Solvent plays a prominent role in controlling the morphology of the nanostructured materials synthesized through the liquid phase synthesis techniques. Though organic solvents employed in various synthetic techniques are immensely useful in the shape and size controlled synthesis of nanostructured materials, some of their drawbacks such as poor solubility of inorganic precursors, low boiling point, high vapor pressure, high toxicity and flammable/explosive nature make them unpopular. Therefore, ionic liquids are gaining significant attention as a green medium for the synthesis of inorganic materials due to the growing environmental awareness. Low melting point, high chemical and thermal stability, high polarity for solubilizing a wide range of compounds, and ability to act as an ionic halide source are the attractive properties of ionic liquids. Various semiconductor photocatalysts have been synthesized using ionic liquid as solvent, and since they possess halogens in their functional groups, they are more suited to the preparation of BiOX/$Bi_xO_yX_z$ [86]. For example, Xia et al. reported the synthesis of ultrathin g-C_3N_4/$Bi_4O_5I_2$ layered nanojunctions using [Hmim]I (1-hexyl-3-methylimidazolium iodide) ionic liquid. Highly reactive ionic liquid acted as the iodine source, also served as the capping agent for the formation of ultrasmall $Bi_4O_5I_2$ nanosheets and facilitated the wide distribution over ultrathin g-C_3N_4. The growth of ultrasmall $Bi_4O_5I_2$ and their wide distribution over the ultrathin g-C_3N_4 promoted the construction of a tight heterojunction under hydrothermal conditions [87].

Similarly, g-C_3N_4/BiOBr microspheres were synthesized by the dispersion of g-C_3N_4 to a solution made by dissolving $Bi(NO_3)_3{\bullet}5H_2O$ in ethanol containing a stoichiometric amount of ionic liquid [C_{16}mim]Br (1-hexadecyl-3-methylimidazolium bromide). During the reaction, the ionic liquid [C_{16}mim]Br acted as the solvent, reactant, template and most importantly as a dispersing agent, which ensured the better dispersion of g-C_3N_4 in the aqueous solution due to electrostatic attraction. As observed from Figure 4, the FESEM and TEM micrographs of the solvothermally synthesized g-C_3N_4/BiOBr composites exhibited relatively uniform 3D flower-like microspheres with self-assembled nanosheets on their surface, indicating the wide distribution of g-C_3N_4 on the surface of BiOBr [88,89].

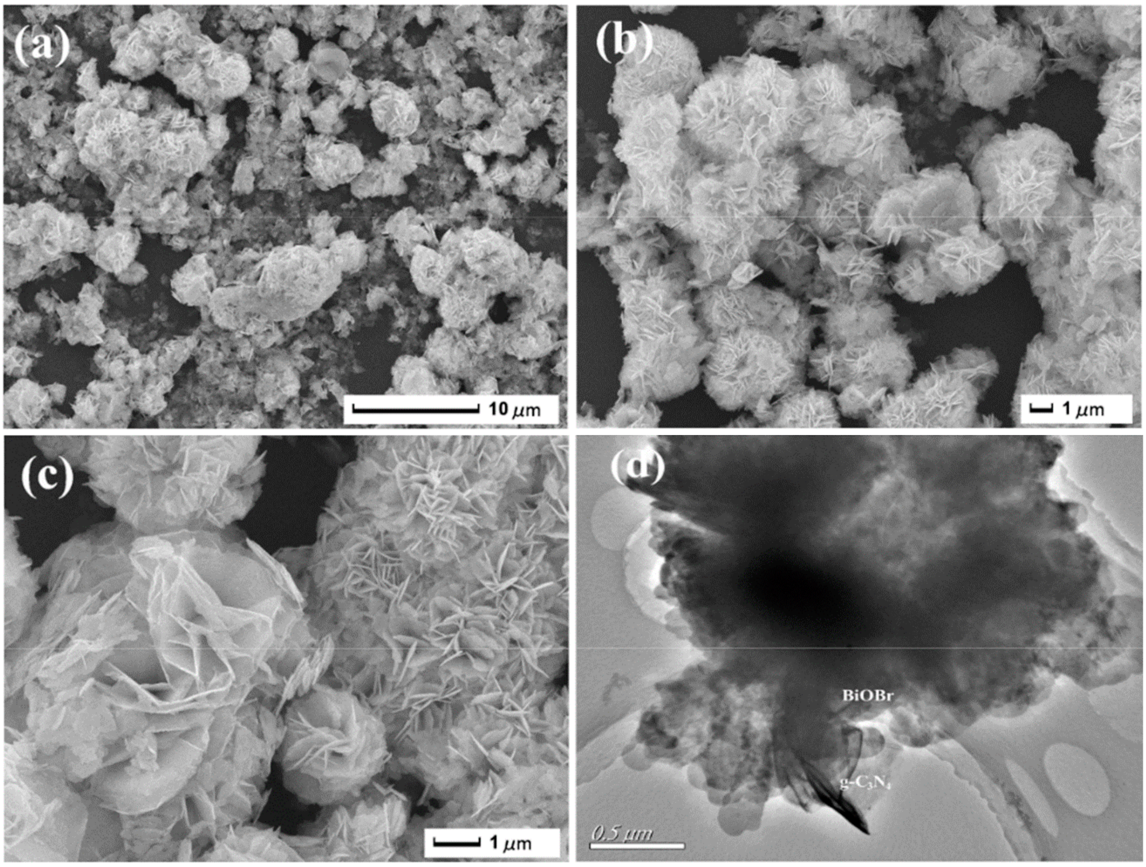

Figure 4. (**a**) Low magnification and (**b**,**c**) magnified FESEM and (**d**) TEM micrographs of g-C_3N_4/BiOBr microspherical composites synthesized by ionic liquid assisted solvothermal method. Reprinted from Ref. [88] with permission from The Royal Society of Chemistry.

3.4. Precipitation Technique

Precipitation is a simple, cost-effective and rapid process of synthesizing semiconductor photocatalysts that can be easily replicated on a larger scale for industrial applications. Further, it is an eco-friendly route that hardly requires any hazardous organic solvents and treatments under high pressure or temperature [90]. The precipitation synthesis of BiOX typically involves the dropwise addition of halide (KX or NaX, where X = Cl, Br and I) solution into a solution of bismuth salt ($BiCl_3$, $Bi(NO_3)_3$ or Bi_2O_3) under acidic conditions. For instance, Ren et al. reported the preparation of three series of $BiOM_xR_{1-x}$ (M, R = Cl, Br, I) solid solutions with 3D nanostructured morphology and adjustable bandgap energy through a low-temperature precipitation technique [59]. Appropriately, adjusting the amount of solute and the solvent in the solid solutions led to the formation of $BiOM_xR_{1-x}$ photocatalysts that could absorb visible light in the range 359–675 nm with a bandgap energy ranging from 3.3–1.7 eV. Composite heterojunctions of g-C_3N_4/$Bi_{12}O_{17}Cl_2$ were prepared by dispersing pre-synthesized g-C_3N_4 into an ethanol solution of $BiCl_3$ at pH 2. The dropwise addition of freshly prepared aqueous NaOH solution into the ethanol solution containing the mixture led to the formation of g-C_3N_4/$Bi_{12}O_{17}Cl_2$ while the pH reached 14 [60]. Chen et al. reported the synthesis of hierarchical hexagonal plates of $Bi_{24}O_{31}Br_{10}$ through co-precipitation and subsequent solvothermal treatment in ethylene glycol, which produced a hierarchical structure by the process of dissolution-recrystallization of 1D $Bi_{24}O_{31}Br_{10}$ nanobelts [61]. In another study, a BiOI-BiOCl/g-C_3N_4 ternary composite was synthesized by a template-free precipitation method using NH_3 solution as the precipitating agent, wherein thin layers of g-C_3N_4 acted as a bed for anchoring BiOI and BiOCl nanosheets for the formation of an efficient heterojunction semiconductor [91].

3.5. Reflux Process

Reflux based synthesis is based on the thermal energy supplied for the progress of the reaction over long periods of time. The phase and morphology of the synthesized nanostructured materials are directly dependent on parameters, viz., the order in which the precursors are added, reflux time and cooling rate [47]. Mousavi et al. employed the reflux technique for the fabrication of g-C_3N_4/Fe_3O_4/BiOI nanocomposites. As the first step, Fe_3O_4 nanoparticles were deposited on the surface of pre-synthesized g-C_3N_4 to form g-C_3N_4/Fe_3O_4. Next, BiOI was synthesized over the surface of g-C_3N_4/Fe_3O_4 by a precipitation reaction between $Bi(NO_3)_3 \bullet 5H_2O$ and NaI, followed by refluxing for 30 min at 96 °C [92]. Similarly, the fabrication of g-C_3N_4/carbon dots/BiOCl and g-C_3N_4/carbon dots/BiOBr heterojunction photocatalysts was also reported by employing the reflux process [93,94].

3.6. Solid-State Calcination

Solid-state calcination is a viable method for the preparation of materials without the utilization of water. Weak van der Waals interaction existing between halogen atoms results in the phase transition from BiOX to $Bi_xO_yX_z$ during the process of calcination due to the removal of unstable halogen. Therefore, $Bi_xO_yX_z$ materials are prepared by the high temperature treatment of the precursors mixed with appropriate stoichiometric ratio. For example, Di et al. reported the preparation of $Bi_{12}O_{17}Cl_2$ by calcining a mixture of Bi_2O_3 and BiOCl in stoichiometric proportions at 650 °C for 10 h [65]. A similar process was reported for synthesizing Bi_3O_4Br by the calcination of Bi_2O_3 and BiOBr mixture at 650 °C for 10 h [95]. Additionally, the solid-state calcination method was employed in the fabrication of Bi_3O_4Cl/g-C_3N_4 heterojunction that was reported to have a tight face-to-face connection between the semiconductors for improved photocatalytic activity [96].

3.7. Sonochemical Synthesis

Sonochemical (also known as ultrasound-assisted) synthesis is a versatile approach that utilizes the high intensity ultrasound for the production of nanostructured inorganic materials in a controllable fashion, which are often unattainable through the conventional methods [97]. Water and ionic liquids are typically used as replacements for volatile and toxic organic solvents [98]. In comparison to the chemical reactions progressing through the supply of common energy sources (such as heat, light, electric potential, radiation, etc.), the ultrasonic irradiation provides an unusual reaction condition that leads to acoustic cavitation (i.e., the formation, growth and implosive collapse of bubbles in liquids), which drives the rapid nucleation and growth of the inorganic materials. For example, Liu et al. reported the synthesis of a g-C_3N_4/BiOBr heterojunction photocatalyst through the sonochemical synthesis technique [99]. A solution of $Bi(NO_3)_3•5H_2O$ dissolved in ethylene glycol was mixed with DI water containing pre-synthesized g-C_3N_4 under ultrasound irradiation at 40 °C for 2 h to form a uniform suspension, to which a stoichiometric proportion of NaBr and PVP were added dropwise and heated to 80 °C for 3 h. TEM micrographs of the pristine g-C_3N_4, pristine BiOBr and sonochemically synthesized g-C_3N_4/BiOBr are shown in Figure 5. A schematic representation of the 2D-2D heterojunction (Figure 5g) and the elemental maps (Figure 5h) confirming the deposition of BiOBr over g-C_3N_4 is also shown in Figure 5.

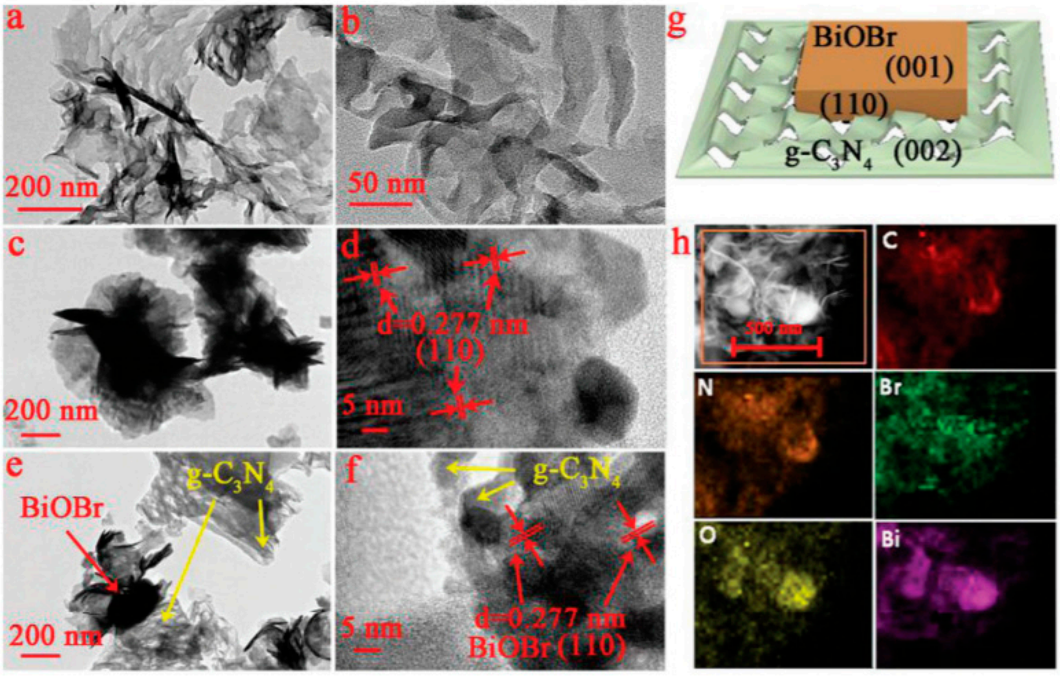

Figure 5. TEM micrographs of (**a**,**b**) pristine g-C_3N_4, (**c**,**d**) pristine BiOBr and (**e**,**f**) g-C_3N_4/BiOBr; (**g**) schematic representation of growth of BiOBr layer over the surface of g-C_3N_4 forming the heterojunction photocatalyst and (**h**) elemental maps confirming the growth of BiOBr over g-C_3N_4. Reprinted from Ref. [99] with permission from The Royal Society of Chemistry.

4. Photocatalytic Activity

4.1. Photocatalytic Degradation of Organic and Inorganic Contaminats

BiOX/$Bi_xO_yX_z$ photocatalysts have demonstrated admirable performance in the degradation of various organic and inorganic contaminants such as methyl orange, rhodamine B, methylene blue, acid orange, microcystin-LR, 2,4 dichlorophenol, bisphenol-A, tetracycline hydrochloride, phenol, carbamazepine, levofloxacin, metronidazole, fuchsine, methyl mercapton, sulfamethoxazole, mercury, chromium, etc. In general, the photocatalytic reaction for the degradation of organic contaminants involves three simultaneous steps, viz., photoexcitation for the generation of charge carriers (e^- and h^+) at the CB and VB, the separation of charges and their transfer to the active sites on the semiconductor surface, the formation of radical species by the ionization of water, i.e., reaction of the holes (h^+) with hydroxyl ions (OH^-) to produce hydroxyl radicals ($^•OH$) and reaction of the electrons (e^-) with the superoxide anion radicals ($^•O_2{}^-$), which subsequently react with the organic contaminants adsorbed on the photocatalyst surface [100,101]. Di et al. synthesized ultrathin $Bi_4O_5Br_2$ and BiOBr nanosheets and studied their capability to degrade ciprofloxacin under visible light. Lower energy bandgap (2.33 eV) and a more negative CB position of ultrathin $Bi_4O_5Br_2$ nanosheets facilitated the improved electronic transition, the generation of extra charge carriers and the formation of more $^{\bullet}O_2^-$ radicals that collectively enabled it to display a maximum rate constant of 0.0113 min^{-1}, which was 1.9 times higher than ultrathin BiOBr nanosheets [102]. Wang et al. synthesized $Bi_{24}O_{31}Br_{10}$ nanosheets with thicknesses of 40, 85 and 130 nm through the solvothermal method and utilized them for the photodegradation of tetracycline hydrochloride under visible light irradiation. The three $Bi_{24}O_{31}Br_{10}$ nanosheets with 40 nm thickness demonstrated 95% degradation of tetracycline hydrochloride within 90 min, in comparison to the thicker counterparts. The enhanced photocatalytic activity of $Bi_{24}O_{31}Br_{10}$ nanosheets with 40 nm thickness was attributed to lattice defects formed by bromine vacancies that subsequently improved the charge carrier density, charge separation and transportation [103]. A BiOBr-g-C_3N_4 heterojunction photocatalyst synthesized through a single-step chemical bath method exhibited enhanced photodegradation of 10 ppm rhodamine B under visible light in comparison to pristine g-C_3N_4, pristine BiOBr and a composite formed by mixing g-C_3N_4 and BiOBr in 1:1 weight ratio. The enhanced performance of the BiOBr-g-C_3N_4 photocatalyst was attributed to the perfect coupling between the BiOBr-{001} and g-C_3N_4-{002} facets, which facilitated the unhindered transport of the photogenerated charges while curbing their recombination [104]. Sphere-like g-C_3N_4/BiOI composite photocatalysts synthesized using ionic liquids exhibited excellent photocatalytic activity in the degradation of rhodamine B, methylene blue, methyl orange, bisphenol A and 4-chlorophenol under visible light irradiation. Among the various composite photocatalysts, the 15 wt% g-C_3N_4/BiOI exhibited optimal performance in comparison to pristine BiOI, which was attributed to the heterojunction formed between g-C_3N_4 and BiOI that effectively separated the photogenerated charge carriers and enhanced the interfacial charge transfer as evidenced through its photocurrent response [105]. Liu et al. reported the fabrication of g-C_3N_4/Bi_5O_7I composite photocatalysts by the thermolysis of melamine with pre-synthesized BiOI at 520 °C for 4 h [106]. Interestingly, during thermolysis BiOI was transformed to Bi_5O_7I and a strong interfacial contact was established with g-C_3N_4 due to in situ co-crystallization, which enabled it to exhibit excellent performance in the photodegradation of rhodamine B and phenol under visible light irradiation due to faster charge migration and separation over the heterojunction. The results revealed that h^+ and $^{\bullet}O_2^-$ were the primary active species, and the rate of photodegradation of rhodamine B using 30 wt% g-C_3N_4/Bi_5O_7I at 1.12 h^{-1} was ~15 and 3 times higher than that of pristine g-C_3N_4 and Bi_5O_7I, respectively. In another study, microspheres of g-C_3N_4/Bi_5O_7I synthesized through the hydrothermal method using ethylene glycol as the solvent exhibited enhanced photodegradation of methyl orange and rhodamine B with rate constants 0.084 min^{-1} and 0.197 min^{-1}, respectively. The results of scavenger studies and electron spin resonance spectroscopy confirmed that $^{\bullet}O_2^-$ was the primary active species, which could only have been generated if the transfer mechanism was based on the Z-scheme heterojunction [107]. The visible light photocatalytic oxidation of hazardous gas-phase mercury (Hg^0) to divalent mercury (Hg^{2+}) for its easy removal was reported using g-C_3N_4/Bi_5O_7I nanosheets doped with Yb^{3+} [108]. As observed from Figure 6a, the mercury removal efficiency of g-C_3N_4/Bi_5O_7I doped with Yb^{3+} was 79.01% and 42.02%, respectively, under visible and near infrared light radiation, while the efficiency under near infrared light was just 13.3% without Yb^{3+} doping. Scavenger studies and electron spin resonance spectroscopy revealed that $^{\bullet}O_2^-$ and $^{\bullet}OH$ were the primary active species responsible for the oxidation of gas phase Hg^0, while the mechanism of charge transfer was based on the Z-scheme heterojunction with enhanced separation of electrons due to the formation of a new energy band below the CB of Bi_5O_7I as a result of doping Yb^{3+}, as depicted in Figure 6b.

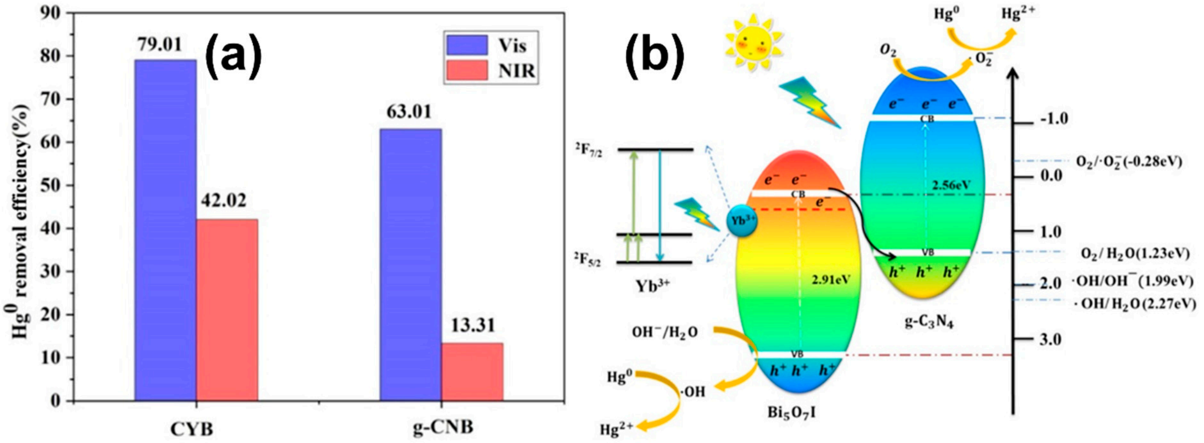

Figure 6. (**a**) Mercury removal efficiency under visible and near infrared light excitation in the presence of g-C_3N_4/Yb^{3+}-Bi_5O_7I (CYB) and g-C_3N_4-Bi_5O_7I (g-CNB) as photocatalysts, (**b**) schematic depicting the mechanism of charge transfer in the Z-scheme heterojunction g-C_3N_4/Yb^{3+}-Bi_5O_7I during the photocatalytic oxidation of Hg^0. Reprinted from Ref. [108] with permission from American Chemical Society.

Zhang et al. reported the fabrication of a heterojunction photocatalyst by the in situ hydrothermal growth of $Bi_7O_9I_3$ on ultrathin g-C_3N_4 for the degradation of doxycycline hydrochloride under visible light. Microspheres of $Bi_7O_9I_3$/g-C_3N_4 exhibited a photodegradation efficiency of ~80% that was ~2 and 5.4 times greater than pristine $Bi_7O_9I_3$ and g-C_3N_4, respectively, which could be attributed to their large surface area (68.55 m^2 g^{-1}) and enhanced charge generation/separation in the heterojunction. Scavenger studies and electron spin resonance spectroscopy revealed that $^\bullet O_2{}^-$ and $^\bullet OH$ were the primary active species that were predominantly involved in breaking the stable structure of doxycycline hydrochloride, while all the experimental data and characterization evidence confirmed that the mechanism of photodegradation followed direct Z-scheme heterojunction [109]. In another study, a g-C_3N_4 modified $Bi_4O_5I_2$ composite prepared in situ by the thermal treatment of a g-C_3N_4/$Bi_4O_5I_2$ precursor at 400 °C for 3 h exhibited enhanced photocatalytic performance in the degradation of methyl orange under visible light with a degradation rate of 0.164 min^{-1}, which was 3.2 and 82 times enhanced in comparison to pristine $Bi_4O_5I_2$ and g-C_3N_4, respectively [110]. A summary of the typical synthesis methods and photocatalytic performance of BiOX/$Bi_xO_yX_z$-g-C_3N_4 heterojunction photocatalysts involved in the degradation of various organic pollutants is presented in Table 1. Further, the details corresponding to the mechanism of photogenerated charge transfer during the degradation of organic pollutants are briefly explained in Section 5.5.

Table 1. Summary of the degradation of organic contaminants in the presence of BiOX/$Bi_xO_yX_z$-g-C_3N_4 heterojunction photocatalysts reported in the literature.

Synthesis Method	Precursors	Morphology	Contaminant Parameters	Light Source	Heterojunction Type	Significance of the Result	Ref.
			BiOX-g-C_3N_4				
			BiOI-g-C_3N_4				
Solid-phase calcination	Bi$(NO_3)_3$·5H_2O, KI and $C_3H_6N_6$	Layers of g-C_3N_4 grown on the surface of BiOI microspheres	Microcystin-LR (5 ppm)	350 W Xe lamp (λ > 420 nm)	Direct solid-state Z-scheme	Optimized content of g-C_3N_4 over BiOI for high activity was found to be 4 wt%	[111]
Electrostatic self-assembly	Bi$(NO_3)_3$·5H_2O, KI, $C_3H_6N_6$, H_2SO_4, HNO_3, and $C_2H_6O_2$	g-C_3N_4 nanoparticles on flower-like BiOI nanosheets	Methyl orange (10 ppm)	300 W Xe lamp (λ > 420 nm)	p-n	Surficial dispersive heterojunctions were beneficial for degradation of MO	[75]

Table 1. *Cont.*

Synthesis Method	Precursors	Morphology	Contaminant Parameters	Light Source	Heterojunction Type	Significance of the Result	Ref.
Simple precipitation	$Bi(NO_3)_3{\cdot}5H_2O$, KI, $C_3H_6N_6$, $C_2H_6O_2$ and CTAB	Thin nanosheets of BiOI lie on the surface of g-C_3N_4	2,4-dichlorophenol (10 ppm) Bisphenol A (10 ppm) Rhodamine B (100 ppm) Tetracycline hydrochloride (10 ppm)	300 W Xe lamp ($\lambda > 420$ nm)	p-n	Top-top facets of BiOI (001)/g-C_3N_4 (002) promoted generation of $^1O_2$ and $^{\bullet}O_2{}^-$ accounting for excellent photocatalytic activity	[112]
In situ precursor transformation	$CO(NH_2)_2$, $Bi(NO_3)_3{\cdot}5H_2O$, KI and $C_2H_6O_2$	Numerous quantum-sized nanoparticles are uniformly dispersed across the g-C_3N_4 nanosheets	Phenol (100 ppm)	60 W LED lamp ($\lambda > 420$ nm)	Direct Z-scheme	Increase in the electron density on BiOI led to internal electric field formation favouring Z-scheme configuration	[113]
Solvothermal	$Bi(NO_3)_3{\cdot}5H_2O$, KI, $C_3H_6N_6$ and $C_2H_6O_2$	BiOI nanoplates are irregularly dispersed over the surface of g-C_3N_4 nanosheets	Rhodamine B (20 ppm)	300 W Xe lamp ($\lambda > 420$ nm)	p-n	Charge transfer mode in the BiOI/g-C_3N_4 followed the double-transfer mechanism	[114]
Solvothermal	$Bi(NO_3)_3{\cdot}5H_2O$, KI, HNO_3, $C_3H_6N_6$ and CH_4N_2S	Thin nanosheets of BiOI composited with wrinkled nanosheets of g-C_3N_4	Methylene blue (20 ppm)	50 W, 410 nm LED light arrays	Direct Z-scheme	Strong IEF at interface occurred due to difference in their Fermi energies was proved by DFT calculations	[115]
Ultrasonication-assisted	$C_3H_6N_6$, $Bi(NO_3)_3{\cdot}5H_2O$, KI, C_2H_5OH	BiOI particles are grown over the surface of g-C_3N_4 sheets	Cr (VI) (10 ppm)	500 W Xe lamp	Z-scheme	The non-radiative recombination process of photoinduced carriers at the interface was confirmed by photoluminescence and ESR	[116]
			BiOCl-g-C_3N_4				
Simple calcination	$Bi(NO_3)_3{\cdot}5H_2O$, CH_4N_2O, $C_6H_{14}O_6$ and NaCl	g-C_3N_4 nanosheets acted as substrate for compactly anchoring BiOCl nanoplates	Methyl orange (10 ppm)	300 W Xe lamp	Binary heterojunction	Large contact surface of 2D hybrid structure was efficient in solving detrimental photoinduced carrier recombination	[117]
Solvothermal	$Bi(NO_3)_3{\cdot}5H_2O$, NaCl, PVP, K-30, CH_4N_2O and $C_3H_8O_3$	Ultrathin nanosheets of BiOCl are covered by 2D g-C_3N_4 layers stacked in the form of multi-slice structure	4-chlorophenol (10 ppm)	300 W short-arc Xe lamp	Binary heterojunction	Introduction of oxygen vacancies brings a new defect level for increased photoabsorption	[118]
Hydrothermal	$C_3H_6N_6$, NH_4Cl, $Bi(NO_3)_3{\cdot}5H_2O$ and KCl	Smooth surface of BiOCl nanodiscs turned rough after loading ultrathin g-C_3N_4 nanosheets	Rhodamine B (10 ppm)	300 W Xe lamp	p-n	Photosensitization of RhB played critical role in degradation process over BiOCl under visible light	[119]

Table 1. *Cont.*

Synthesis Method	Precursors	Morphology	Contaminant Parameters	Light Source	Heterojunction Type	Significance of the Result	Ref.
Ionic liquid-assisted	$C_2H_4N_4$, $C_2H_6O_2$, $Bi(NO_3)_3{\cdot}5H_2O$ and $[C_{16}mim]Cl$	Spherical microstructures with large number of smaller nanosheets of BiOCl and g-C_3N_4	Rhodamine B (10 ppm)	300 W Xe lamp	p-n	$[C_{16}mim]Cl$ having positive polarity improved the dispersity of g-C_3N_4	[89]
In situ surfactant-free	$C_3H_6N_6$, $Bi(NO_3)_3{\cdot}5H_2O$, HCl and C_2H_5OH	Irregular elliptical BiOCl nanosheets are grown over the surface of g-C_3N_4 sheets	Rhodamine B (10 ppm)	300 W Xe lamp	Binary heterojunction	The appropriate proportion of BiOCl in heterojunction and large surface area with higher adsorption capacity provided larger photoactive sites for photodegradation of RhB	[120]
Microwave-assisted	$Bi(NO_3)_3{\cdot}5H_2O$, KCl, $C_2H_6O_2$, $C_2H_4N_4$	Microspheres assembled by nanosheets	Carbamazepine (2.5 ppm)	LED lamp (λ > 420 nm)	n-p	Oxygen vacancies can be assessed by reactions using ethylene glycol as a solvent at a high temperature	[121]
Microwave-assisted	$C_3H_6N_6$, $Bi(NO_3)_3{\cdot}5H_2O$, KCl, HNO_3	BiOCl microplates were grown over the surface of g-C_3N_4 nanosheets	Nizatidine (5 ppm)	Mic-LED-365	Binary heterojunction	pH of the solution was adjusted to match the isoelectric point of the complex materials for enhancing the photocatalytic activity	[122]
			BiOBr-g-C_3N_4				
Reflux process in oil bath	CH_4N_2O, $C_2H_6O_2$, $Bi(NO_3)_3{\cdot}5H_2O$, KBr and C_2H_5OH	BiOBr nanoplates are deposited on the surface of larger g-C_3N_4 nanosheets	Rhodamine B (10 ppm) Bisphenol A (5 ppm)	300 W Xe lamp	Z-scheme	More reactive sites and enhanced mass transfer resulting from larger specific surface area and mesoporosity led to higher activity	[123]
Hydrothermal	$C_3H_6N_6$, $C_2H_6O_2$, $Bi(NO_3)_3{\cdot}5H_2O$ and CTAB	Nanoflakes of g-C_3N_4 and BiOBr are observed	Bisphenol A (10 ppm) Methyl orange (10 ppm) Rhodamine B (10 ppm)	300 W Xe lamp	Binary heterojunction	Surface functional groups of g-C_3N_4 provided nucleation sites for reaction by inhibiting the formation of BiOBr assembly	[124]
Electrostatic self-assembly	$Bi(NO_3)_3{\cdot}5H_2O$, KBr, $C_3H_6N_6$, HCl, CH_3COOH and $C_2H_3NaO_2$	3D hierarchical flower-like structures of BiOBr are attached to surface of pg-C_3N_4 consisting of nanostructures and plicate shapes.	Carbamazepine (5 ppm)	500 W Xe lamp	Binary heterojunction	Presence of low concentration of bicarbonate accelerated the carbamazepine degradation while nitrate and chloride inhibited its efficiency	[62]
Solvothermal	$Bi(NO_3)_3{\cdot}5H_2O$, CTAB, $C_3H_8O_3$, PVP and $C_3H_6N_6$	Flower-like microspheres of BiOBr are grown over g-C_3N_4 nanosheets	Methyl orange (10 ppm) Rhodamine B (10 ppm)	500 W Xe lamp	Z-scheme	Optimum content of g-C_3N_4 was found to be 5 wt% over the BiOBr nanosheets	[125]

Table 1. *Cont.*

Synthesis Method	Precursors	Morphology	Contaminant Parameters	Light Source	Heterojunction Type	Significance of the Result	Ref.
Ultrasound-assisted water-bath deposition	$Bi(NO_3)_3·5H_2O$, PVP, $C_2H_6O_2$, NaBr, C_2H_5OH and CH_4N_2O	BiOBr nanoflakes are dispersed over the surface of g-C_3N_4 nanosheets	Rhodamine B (20 ppm) *E. coli* (1.0 × 10^6 CFU mL^{-1})	Visible light	Z-scheme	Z-scheme photocatalytic mechanism was evidenced from Tafel curve analysis	[99]
Solvothermal	$Bi(NO_3)_3·5H_2O$, $C_3H_6N_6$, CTAB and $C_2H_6O_2$	g-C_3N_4 nanosheets are compactly combined with BiOBr nanosheets	Rhodamine B (10 ppm)	500 W Xe lamp	Binary heterojunction	Holes and superoxide radicals played dominant role in the RhB removal	[126]
Template-assisted hydrothermal	$Bi(NO_3)_3·5H_2O$, NaBr, $C_2H_6O_2$, NaOH, C_2H_5OH and NH_4Cl	BiOBr microspheres are randomly dispersed on the surface of g-C_3N_4	Tetracycline (20 ppm) Rhodamine B (15 ppm)	500 W Xe lamp	Direct Z-scheme	L-lysine with polar functional groups of amino and hydroxyl, served as bio-template for controlling the crystal growth and self-assembly process of BiOBr	[81]
Hydrothermal	$C_3H_6N_6$, $Bi(NO_3)_3·5H_2O$, HCl, NaOH, CH_4N_2O, CH_4N_2S and KBr	BiOBr nanolayers are distributed on the surface of porous g-C_3N_4 nanosheets	Methylene blue (10 ppm)	50 W 410 nm LED light	Binary heterojunction	Optimized content of Pg-C_3N_4 in the binary composite for high activity was found to be 20 wt%	[127]
Polycondensation and precipitation	$C_3H_6N_6$, $Bi(NO_3)_3·5H_2O$ and CTAB	Mesoporous flower-like BiOBr are grown over porous sheets of g-C_3N_4	Reactive blue 198 (50 ppm) Reactive black 5 (50 ppm) Reactive yellow 145 (50 ppm)	500 W tungsten lamp	Z-scheme	Degradation pathways were proposed to follow pseudo-first-order kinetics with 30% pGCN-BiOBr	[128]
Reflux process	TEOS, C_2H_5OH, NH_4OH, $C_2H_4N_4$, NH_4HF_2, $Bi(NO_3)_3·5H_2O$, CH_4N_2O and KBr	BiOBr nanoparticles are uniformly loaded on the surface of IO CN	Levofloxacin (10 ppm) Rhodamine B (20 ppm)	300 W Xe lamp	Z-scheme	Combination of Z-scheme and inverse opal structure influenced the visible light absorption ability and photocatalytic performance	[129]
$Bi_xO_yX_z$-g-C_3N_4							
$Bi_7O_9I_3$-g-C_3N_4							
Hydrothermal	$Bi(NO_3)_3·5H_2O$, $C_3H_6N_6$, NaI, CN_2H_4S and CH_3COONa	Flower-like nanospheres of $Bi_7O_9I_3$ are grown over the surface of g-C_3N_4 nanosheets	Doxycycline hydrochloride	Xe lamp	Z-scheme	In situ growth of $Bi_7O_9I_3$ on ultrathin g-C_3N_4 via mild and simple hydrothermal means without any toxic reagents	[109]
Bi_5O_7I-g-C_3N_4							
Hydrothermal	NH_3, C_2H_5OH, TEOS, C18TMOS, CH_2N_2, NH_4HF_2, $Bi(NO_3)_3·5H_2O$, $C_2H_6O_2$ and KI	Bi_5O_7I nanoparticles are grown over surface of porous g-C_3N_4	Phenol (10 ppm)	CEL-HXF300	p-n	Silica templates were used to obtain lamellar and porous g-C_3N_4 in GCN-Bi_5O_7I composite	[130]

Table 1. *Cont.*

Synthesis Method	Precursors	Morphology	Contaminant Parameters	Light Source	Heterojunction Type	Significance of the Result	Ref.
Hydrothermal	$Bi(NO_3)_3{\cdot}5H_2O$, KI, $C_2H_6O_2$ and $C_3H_6N_6$	Irregular shaped layers of g-C_3N_4 are covered on the surface of microspheres consisting of self-assembled thin platelets of Bi_5O_7I	Methyl orange (10 ppm) Rhodamine B (10 ppm)	300 W Xe lamp	Z-scheme Heterojunction	g-C_3N_4-Bi_5O_7I-10 showed better performance towards dye degradation in acidic conditions	[107]
Hydrolysis and thermal condensation	$C_2H_4N_4$ $Bi(NO_3)_3{\cdot}4H_2O$, $C_2H_6O_2$, NaOH, HCl, $C_6H_{15}N$, KH_2PO_4 and KI	Rod-like patterns of Bi_5O_7I are embedded on D-g-C_3N_4	Metronidazole (15 ppm)	300 W Xe lamp	Binary heterojunction	Charge carrier separation in the composite was evidenced from photocurrent response measurements	[131]
$Bi_4O_5I_2$-g-C_3N_4							
Mixed calcination	$C_3H_6N_6$ $Bi(NO_3)_3{\cdot}4H_2O$, NaOH and KI	$Bi_4O_5I_2$ nanoflakes are grown on g-C_3N_4 nanosheets	Rhodamine B (1×10^{-5} M) NO removal	300 W tungsten halogen lamp	n-n	Super oxide radicals and holes are active species during the degradation	[132]
Ionic liquid-assisted solvothermal	$C_6H_{14}O_6$, $C_{10}H_{19}IN_2$, $Bi(NO_3)_3{\cdot}4H_2O$, NaOH and KI	$Bi_4O_5I_2$ nanosheets are dispersed on g-C_3N_4 nanosheets	Rhodamine B (10 ppm) Bisphenol A (10 ppm)	300 W Xe lamp	Binary hetrojunction	[Hmim]I played multiple roles during the synthesis which was propitious for heterojunction formation	[87]
Hydrothermal and heating	$C_3H_6N_6$, $Bi(NO_3)_3{\cdot}4H_2O$, $C_2H_6O_2$ and KI	Hierarchical microspheres of $Bi_4O_5I_2$ are grown on the surface of g-C_3N_4	Methyl orange (20 ppm)	350 W Xe lamp	Type-II	The in situ transformation endowed the composite with good contact between the semiconductors in construction of tight heterojunction	[110]
Bi_3O_4Cl-g-C_3N_4							
Mixing and heating	$Bi(NO_3)_3{\cdot}5H_2O$, HCl, Bi_2O_3 and $C_3H_6N_6$	Irregular blocks consisting of a lot of nanoflakes of Bi_3O_4Cl attached onto the surface of g-C_3N_4	Rhodamine B (10 ppm)	350 W Xe lamp	Binary heterojunction	Coupling Bi_3O_4Cl on g-C_3N_4 improved the specific surface area and charge carrier separation	[133]
Solid phase calcination	$Bi(NO_3)_3{\cdot}5H_2O$, CH_4N_2O, NH_4Cl and $C_2H_6O_2$	Bi_3O_4Cl nanoflakes are grown on g-C_3N_4 nanosheets	Rhodamine B (10 ppm) Tetracycline (10 ppm) Hexavalent chromium (10 ppm)	250 W Xe lamp	Z-scheme	Shorter fluorescent lifetime (0.952 ns) attributed to additional nonradioactive decay channel for electron transfer from Bi_3O_4Cl to g-C_3N_4	[96]
$Bi_{12}O_{17}Cl_2$-g-C_3N_4							
Chemical precipitation	CH_4N_2O, $BiCl_3$, C_2H_5OH and NaOH	$Bi_{12}O_{17}Cl_2$ nanosheets are grown on surface of g-C_3N_4	Rhodamine B (5 ppm) Methyl orange (10 ppm)	300 W Xe lamp	Binary heterojunction	Hydroxyl radicals and holes main active species during the reaction as evidenced from electron spin resonance technique	[60]

Table 1. *Cont.*

Synthesis Method	Precursors	Morphology	Contaminant Parameters	Light Source	Heterojunction Type	Significance of the Result	Ref.
$Bi_4O_5Br_2$-g-C_3N_4							
Ionic liquid-assisted solvothermal	[C_{16}mim]Br, $C_3N_3(NH_2)_3$, C_2H_3N, $C_3N_3Cl_3$, $Bi(NO_3)_3{\cdot}5H_2O$, $C_6H_{14}O_6$ and NaOH	Rod-like g-C_3N_4 has closely combined with sheet-like $Bi_4O_5Br_2$	Ciprofloxacin (10 ppm) Rhodamine B (10 ppm)	300 W Xe lamp	Binary heterojunction	Ionic liquid [C_{16}mim]Br served as solvent, dispersing agent and reactant for the distribution of $Bi_4O_5Br_2$ over g-C_3N_4	[134]
Precipitation	$C_3H_6N_6$, C_2H_5OH, $BiBr_3$ and NaOH	Irregular nanosheets of $Bi_4O_5Br_2$ were stacked with g-C_3N_4 sheets	Rhodamine B (10 ppm) Tetracycline (10 ppm)	72 W LED lamp	Binary heterojunction	Improved adsorptive nature in BBO/CN-75 is due to generation of more Lewis base sites as confirmed by Zeta potential studies	[135]
Solvothermal	$C_3H_6N_6$, $Bi(NO_3)_3{\cdot}5H_2O$, [C_{16}mim]Br, $C_6H_{14}O_6$, NaOH and C_2H_5OH	Ultrathin $Bi_4O_5Br_2$ nanosheets are dispersed on the graphene-like g-C_3N_4 nanosheets	Ciprofloxacin (10 ppm) Rhodamine B (10 ppm)	300 W Xe lamp	Binary heterojunction	Red shift in the bandgap absorption was observed with introduction of graphene-like g-C_3N_4	[85]
Noble metal coupled BiOX-g-C_3N_4							
BiOI/Pt/g-C_3N_4							
Two-step (reduction and stirring)	CH_4N_2O, $NaBH_4$, $H_2PtCl_6{\cdot}6H_2O$, $C_2H_6O_2$, $Bi(NO_3)_3{\cdot}5H_2O$ and KI	Pt nanoparticles and BiOI hierarchical structure grew on the g-C_3N_4 sheets	Phenol (25 ppm) Tetracycline hydrochloride (20 ppm)	Visible light	Solid-state Z-scheme	Unobstructed Z-scheme charge carrier transfer pathways in BiOI/Pt/g-C_3N_4 composite are discussed in relevance to phenol and tetracycline oxidation	[136]
g-C_3N_4/Eu/$Bi_{24}O_{31}Cl_{10}$ (BOC)							
Impregnation-calcination	$Bi(NO_3)_3{\cdot}5H_2O$, $C_3H_6N_6$, NH_4Cl, $C_6H_8O_7$, HNO_3, $NH_3{\cdot}H_2O$ and $Eu(NO_3)_3.6H_2O$	g-C_3N_4 nanosheets were coated on the surface of irregular shaped smaller sized crystal particles of Eu-doped BOC	Rhodamine B (10 ppm)	250 W Xe lamp	Binary heterojunction	CN/Eu-BOC exhibited higher performance than CN/BOC suggesting that Eu (III) could be used as cocatalyst	[137]
g-C_3N_4/Au/BiOBr							
Hydrothermal and in situ reduction	$C_3H_6N_6$, $Bi(NO_3)_3{\cdot}5H_2O$, KBr, C_2H_5OH, $C_8H_{11}NO_2$ and $HAuCl_4{\cdot}4H_2O$	Au nanoparticles are decorated over the surface of lamellar structure of g-C_3N_4 and BiOBr sheets	Phenol (10 ppm)	300 W Xe lamp	Plasmonic Z-scheme	Strong surface plasmon resonance caused by Au NPs contributed to extension of visible light absorption in the ternary composite	[138]
Chemical reduction	$Bi(NO_3)_3{\cdot}5H_2O$, KBr, CH_4N_2S, CTAB, $Na_3C_6H_5O_7$, $AuCl_3$ and C_2H_5OH	Au nanoparticles were uniformly distributed over the surface of g-C_3N_4/BiOBr	Rhodamine B (10 ppm) CO_2 reduction	300 W Xe lamp	Surface plasmon resonance and Z-scheme	Correlation between size of Au NPs and wavelength dependent photocatalytic activity associated with Au-GCN-BiOBr composite is described	[139]

Table 1. *Cont.*

Synthesis Method	Precursors	Morphology	Contaminant Parameters	Light Source	Heterojunction Type	Significance of the Result	Ref.
Carbon material coupled BiOX-g-C_3N_4							
g-C_3N_4/CDs/BiOI							
Precipitation	CN_2H_2, $C_3H_6N_6$, $C_6H_8O_7$, $Bi(NO_3)_3{\cdot}4H_2O$ and NaI	CDs and BiOI nanoparticles are grown in intimate contact with gCN nanosheets	Rhodamine B (2.5×10^{-5} M) Methylene blue (2.5×10^{-5} M) Methyl orange (2.5×10^{-5} M) Fuchsine (9.20×10^{-6} M)	50 W LED lamp	Ternary heterojunction	Co-operative effects of CQDs and g-C_3N_4 promoted the activity of BiOI towards the degradation of organic dyes	[140]
GO/g-C_3N_4/BiOI							
In situ generation	CH_4N_2O, $Bi(NO_3)_3{\cdot}4H_2O$, $C_2H_6O_2$, KI and GO	Flower-like BiOI nanosheets are overlapped with lamellar structure of CN and sheet-like GO.	Methyl orange (10 ppm) Tetracycline (20 ppm) E. coli (50 ppm) S. aureus (50 ppm)	LED lamp	Ternary heterojunction	Loading GO over CN/BiOI resulted in double-charge-transfer at the interface	[141]
g-C_3N_4/MCNTs/BiOI							
Solvothermal	CN_2H_2, KI, $Bi(NO_3)_3{\cdot}4H_2O$ and $C_2H_6O_2$	BiOI nanoparticles are uniformly loaded on surface of g-C_3N_4- MCNTs.	Methylene blue (10 ppm)	300 W Xe lamp	Z-scheme	MCNTs facilitated the electron transfer from BiOI to g-C_3N_4 resulting in Z-scheme charge transfer pathway	[142]
g-C_3N_4/BiOI/rGO immobilized on Ni foam							
Hydrothermal and reduction	CH_4N_2O, $C_2H_4N_4$, $NaSO_4$, $Bi(NO_3)_3{\cdot}5H_2O$, $C_2H_6O_2$, C_2H_6O, NH_3, $H_4N_2{\cdot}H_2O$, Ni foam, GO and NaI	Laminar structures of g-C_3N_4, BiOI and sheet-like rGO form the ternary sheet-like hybrids and are immobilized on the surface of Ni foam.	Methyl orange (5 ppm) CO_2	300 W Xe lamp	Hybrid Z-scheme	rGO functioned as both electron mediator and binder while Ni foam improved the reusability of the composite	[143]
g-C_3N_4/CDs/BiOCl							
Refluxing	$C_3H_6N_6$, $Bi(NO_3)_3{\cdot}5H_2O$, NaCl, CH_4N_2O and $C_6H_8O_7$	Smaller spherical particles of CDs and rod-like particles of BiOCl are grown on the surface of g-C_3N_4 nanosheets	Rhodamine B (1×10^{-5} M) Methylene blue (1×10^{-5} M) Methyl orange (1×10^{-5} M) Fuchsine (0.77×10^{-5} M) Phenol (5×10^{-5} M)	50 W LED lamp	Ternary heterojunction	Formation of g-C_3N_4/CDs/BiOCl composite influenced the optical properties and photocatalytic performance	[93]
BiOBr/rGO/pg-C_3N_4							
Solvothermal	CH_4N_2O, HCl, rGO, $C_2H_6O_2$, $Bi(NO_3)_3{\cdot}5H_2O$ and CTAB	BiOBr and rGO nanosheets are dispersed simultaneously on the surface of pg-C_3N_4	Rhodamine B (10 ppm) Tetracycline (10 ppm)	300 W Xe lamp	Ternary Z-scheme	Optimized content of BiOBr in ternary composite for high activity was found to be 10 wt%	[144]

Table 1. *Cont.*

Synthesis Method	Precursors	Morphology	Contaminant Parameters	Light Source	Heterojunction Type	Significance of the Result	Ref.
			$BiOBr/CDs/g\text{-}C_3N_4$				
Hydrothermal	$Bi(NO_3)_3 \cdot 5H_2O$, KBr, HNO_3, CH_4N_2O, NH_4Cl, $C_6H_8O_7$ and $C_2H_4N_4$	Ultrathin nanosheets	Ciprofloxacin (10 ppm) Tetracycline (20 ppm)	300 W Xe lamp	Z-scheme	Up-converted PL character and short charge transport distance of CDs were beneficial towards broadened light absorption and remarkable interfacial charge transfer	[145]
			CNNs/CDs/BiOBr				
Refluxing	$C_3H_6N_6$, $C_6H_8O_7$, CH_4N_2O, $Bi(NO_3)_3 \cdot 5H_2O$ and NaBr	CDs and BiOBr nanoparticles are accumulated on the surface of carbon nitride nanosheets (CNNs)	Rhodamine B (1×10^{-5} M) Methylene blue (1×10^{-5} M) Methyl orange (1×10^{-5} M) Cr(VI) (100 ppm)	50 W LED lamp	Ternary Z-scheme	CNNs/CDs/BiOBr was stable even after five consecutive cycles towards the degradation of pollutants with fresh dye solution each time	[94]
			$g\text{-}C_3N_4/BiOBr\text{-}rGO$				
Two-step hydrothermal assembly route	Graphite powder, $C_8H_{11}NO_2$, H_2SO_4, HNO_3, $KMnO_4$, H_2O_2, $Bi(NO_3)_3 \cdot 5H_2O$, KBr and $C_3H_6N_6$	Flake-like BiOBr are covered by thin layer of $g\text{-}C_3N_4$ film	Rhodamine B (10 ppm)	300 W Xe lamp	p-n	Immobilization of the powder catalyst on 3D RGO aerogel surface collectively contributed to excellent recycling process of the catalyst	[146]
			Carbon Fibers/$g\text{-}C_3N_4$/BiOBr				
Chemical bath deposition	Carbon fibres, CH_4N_2O, $Bi(NO_3)_3 \cdot 5H_2O$, C_4H_9NO and KBr	Growth of $g\text{-}C_3N_4$ nanosheets and BiOBr nanoplates on carbon fibers (CFs)	Tetracycline (20 ppm)	300 W Xe lamp	Ternary heterojunction	Recyclable cloth-shaped CFs/$g\text{-}C_3N_4$/BiOBr bundles had great mechanical strength	[147]
			$BiOBr/CS/g\text{-}C_3N_4$				
Solvothermal	$C_3H_6N_6$, $C_6H_{12}O_6$, $Bi(NO_3)_3 \cdot 5H_2O$, KBr and $C_2H_6O_2$	Spherical carbon spheres are wrapped uniformly with $g\text{-}C_3N_4$ and BiOBr matrix	Rhodamine B (10 ppm)	300 W W halogen lamp	Ternary heterojunction	Carbon spheres were used as interlinking network between $g\text{-}C_3N_4$ and BiOBr matrix for effective electron transfer	[148]
			BiOI/porous $g\text{-}C_3N_4$/graphene hydrogel				
Hydrothermal	$Bi(NO_3)_3 \cdot 5H_2O$, KI, CH_4N_2O, $C_2H_6O_2$,	BiOI and porous $g\text{-}C_3N_4$ were loaded onto 3D cross-linking graphene hydrogel	Methylene blue (40 ppm) Levofloxacin (20 ppm)	300 W Xe lamp	Ternary heterojunction	3D graphene hydrogel played multiple roles: enhanced adsorption ability, provided bulk electron transfer channels, rendered easy separation and recycling	[149]

Table 1. *Cont.*

Synthesis Method	Precursors	Morphology	Contaminant Parameters	Light Source	Heterojunction Type	Significance of the Result	Ref.
Semiconductor coupled BiOX-g-C_3N_4							
Polyacrylonitrile/g-C_3N_4/BiOI nanofibres							
Impregnation	$Bi(NO_3)_3 \cdot 5H_2O$, KI, $C_3H_6N_6$, N,N-dimethylformamide (C_3H_7NO) and polyacrylonitrile $(C_3H_3N)_n$	BiOI nanostructures are uniformly dispersed over PAN/g-C_3N_4 nanofibres	Rhodamine B (10 ppm) Cr (VI) (20 ppm)	300 W Xe lamp	-	Ultralong 1D macroscopic flexible self-supporting floating structures prevented agglomeration and loss of catalyst during recycling	[150]
SiO_2@g-C_3N_4/BiOI nanofibres							
Impregnation	Polyvinylpyrrolidone $(C_6H_9NO)_n$, TEOS ($SiC_8H_{20}O_4$), ethanol, $C_3H_6N_6$, $Bi(NO_3)_3 \cdot 5H_2O$ and KI	BiOI nanosheets are loaded on the surface of ultrathin g-C_3N_4@SiO_2 nanofibres.	Rhodamine B (10 ppm)	150 W Xe lamp	Direct Z-scheme	Depositing SiO_2 NFs at BiOI/g-C_3N_4 interface improved Z-scheme charge carrier separation and recyclability	[151]
BiOI/AgI/g-C_3N_4							
In situ crystallization	$Bi(NO_3)_3 \cdot 5H_2O$, KI, $AgNO_3$ and $C_3H_6N_6$	Irregular nanoparticles of AgI are grown on the surface of g-C_3N_4 covered with BiOI nanoflakes.	Methyl orange (10 ppm) Cr(VI) (50 ppm)	300 W Xe lamp	Ternary heterojunction	Visible light response was tailored from 460 to 560 nm by increasing the content of AgI in the composite	[152]
BiOI/g-C_3N_4/CeO_2							
Calcination and hydrothermal	$Bi(NO_3)_3 \cdot 5H_2O$, KI, $Ce(NO_3)_3.6H_2O$ and $C_3H_6N_6$	BiOI microspheres and CeO_2 nanoparticles are randomly adhered to the surface of g-C_3N_4	Tetracycline (20 ppm)	300 W Xe lamp	Ternary heterojunction	Optimum content of CeO_2 in the ternary hybrid was found to be 3 wt% towards efficient TC degradation	[153]
BiOI@MIL-88A(Fe)@g-C_3N_4							
Hydrothermal	$Bi(NO_3)_3 \cdot 5H_2O$, KI, $C_2H_6O_2$, $C_3H_6N_6$, $FeCl_3 \cdot 6H_2O$ and $C_4H_4O_4$	BiOI flower-like hierarchical microspheres are loaded on the surface of MIL-88A(Fe)@g-C_3N_4 with core@shell structure	Acid blue 92 (10 ppm) Rhodamine B (10 ppm) Phenol (10 ppm)	300 W Xe lamp	Ternary heterojunction	g-C_3N_4 deposited over BiOI@MIL-88A(Fe) via hydrothermal method facilitated carrier separation in the composite	[154]
g-C_3N_4/Fe_3O_4/BiOI							
Reflux and precipitation	$Bi(NO_3)_3 \cdot 4H_2O$, NaI, $C_3H_6N_6$, $FeCl_3 \cdot 6H_2O$, $FeCl_2 \cdot 4H_2O$ and NH_3	Fe_3O_4 particles and BiOI are grown on the surface of g-C_3N_4 sheets	Rhodamine B (1×10^{-5} M) Methylene blue (1.3×10^{-5} M) Methyl orange (1.05×10^{-5} M)	50 W LED source	Ternary heterojunction	g-C_3N_4/Fe_3O_4/BiOI was magnetically separated from the aqueous medium within a short span of time	[92]
g-C_3N_4/I^{3-}-BiOI							
Solvothermal	$C_3H_6N_6$, $Bi(NO_3)_3 \cdot 4H_2O$, $C_4H_6O_6$, $C_4H_{10}O$, EDTA-2Na, $C_6H_8O_6$, $K_2Cr_2O_7$, NaN_3, DMPO and DMSO	Flower-like microspheres containing ultrathin nanosheets of BiOI are loaded g-C_3N_4	Methyl mercaptan (CH_3SH) (70 ppm)	8 W LED	Z-scheme	CH_3SH removal monitored via in situ DRIFTS and the intermediate and conversion pathways were elucidated	[63]

Table 1. *Cont.*

Synthesis Method	Precursors	Morphology	Contaminant Parameters	Light Source	Heterojunction Type	Significance of the Result	Ref.
MoS_2/g-C_3N_4/$Bi_{24}O_{31}Cl_{10}$							
Impregnation-calcination	$Bi(NO_3)_3{\cdot}5H_2O$, $C_3H_6N_6$, NH_4Cl, $C_6H_8O_7$, HNO_3, $NH_3{\cdot}H_2O$, $(NH_4)_6Mo_7O_{24}.4H_2O$ and DMF	Numerous g-C_3N_4 nanosheets and flower-like MoS_2 are grown and combined with irregular block-like shapes of BOC	Tetracycline (20 ppm)	300 W Xe lamp	Dual Z-scheme ternary heterojunction	Carrier lifetime was higher in CN/MS/BOC (3.9782 ns) compared to BOC (1.0163 ns)	[155]
BiOCl/Bi_2MoO_6/g-C_3N_4							
Refluxing	$Bi(NO_3)_3{\cdot}5H_2O$, $Na_2MoO_4{\cdot}2H_2$, HCl and NaOH	Combination of irregular rodlike, platelet-shaped and sheet-shaped morphologies	Rhodamine B (0.5 mM)	350 W Xe lamp	Ternary heterojunction	BiOCl/Bi_2MoO_6 immobilized on g-C_3N_4 surface exhibited dual functionality as photocatalysts and optical limiters	[156]
BiOCl/CdS/g-C_3N_4							
Solvothermal cum co-precipitation	$C_3H_6N_6$, HCl, $C_4H_6CdO_4$, DMSO, $Bi(NO_3)_3{\cdot}5H_2O$, C_3H_8O and NaOH	Growth of hierarchical BiOCl nanoflowers with embedded CdS nanoparticles on g-C_3N_4 nanosheets	Rhodamine B (20 ppm) Phenol	400 W Ne-illuminator	Ternary heterojunction	Presence of two visible light active components led to highly efficient electron transfer in multicomponent heterojunction	[157]
BiOCl/g-C_3N_4/kaolinite							
Two-step layer-by-layer self-assembly	$C_2H_4N_4$, CTAC, $Bi(NO_3)_3{\cdot}5H_2O$, CH_3COOH, HCHO and kaolinite	g-C_3N_4 and BiOCl ultrathin nanosheets are covered on the surface of kaolinite lamellar with single layer	Rhodamine B (10 ppm)	500 W Xe lamp	Ternary heterojunction	Holes dominated the degradation pathways for BiOCl/g-C_3N_4/kaolinite	[158]
g-C_3N_4/g-C_3N_4/BiOBr							
Thermal decomposition and solvothermal	CH_4N_2O, CH_4N_2S, $Bi(NO_3)_3{\cdot}5H_2O$, KBr, $NaC_{12}H_{25}SO_4$ and $C_2H_6O_2$	g-C_3N_4 prepared using thiourea-urea complex was uniformly dispersed on the nanosheets of the flower-like BiOBr	Rhodamine B (20 ppm) Fluorescein isothiocyanate (20 ppm) Tetracycline hydrochloride (20 ppm)	High pressure Xe lamp	Ternary direct Z-scheme + isotype heterojunction	Combined effect of Z-scheme + isotype heterojunction charge transfer pathways was observed in g-C_3N_4/g-C_3N_4/BiOBr	[159]
AgBr/g-C_3N_4/BiOBr							
Hydrothermal and in situ ion-exchange	CH_4N_2O, KBr, $Bi(NO_3)_3{\cdot}5H_2O$, $AgNO_3$ and $C_2H_6O_2$	AgBr nanoparticles are dispersed on the surface of g-C_3N_4/BiOBr nanosheets	Rhodamine B (10 ppm) Tetracycline (10 ppm)	300 W Xe lamp	Ternary heterojunction	Influence of AgBr loading on GCN/BOB composite towards the photocatalytic activity is discussed in detail	[160]
Brookite/g-C_3N_4/BiOBr							
Hydrothermal	$TiCl_4$, $Bi(NO_3)_3{\cdot}5H_2O$, $C_3H_6N_6$, CTAB, NH_4Cl, KBr and NaOH	Spindle shaped brookite are wrapped by the layer structure of BiOBr which are further wrapped by lamellar g-C_3N_4	Rhodamine B (10 ppm)	70 W metal halide lamp	Ternary heterojunction	Ternary composite had ability to destroy the oxygen heteroanthracene ring and chromogenic group of RhB	[161]

Table 1. *Cont.*

Synthesis Method	Precursors	Morphology	Contaminant Parameters	Light Source	Heterojunction Type	Significance of the Result	Ref.
BiOCl/g-C_3N_4@UiO-66							
Solvothermal	$Bi(NO_3)_3 \cdot 5H_2O$, KCl, CH_3COOH, $C_3H_6N_6$, $ZrCl_4$, $C_8H_6O_4$, C_3H_7NO	BiOCl nanoplates and g-C_3N_4 nanosheets were decorated over the surface of UiO-66	Rhodamine B (10 ppm)	250 W Xe lamp	Ternary heterojunction	UiO-66 was proved beneficial to the photocatalytic reaction by enlarging the photoadsorption and preventing the electron-hole recombination	[121]
g-C_3N_4/BiOI/$Bi_2O_2CO_3$							
Simple reflux and in situ ion exchange	$Bi(NO_3)_3 \cdot 5H_2O$, $C_3H_6N_6$, KI, $NaHCO_3$, Na_2SO_4, CH_3CH_2OH, $Kr_2Cr_2O_7$, H_2SO_4, H_3PO_4	Thin nanosheets of BiOI are distributed over g-C_3N_4 layers	Rhodamine B (10 ppm)	250 W Xe lamp	Ternary heterojunction	Based on the matched energy levels, BiOI acted as the charge transmission bridge	[162]
BiOX and BiOY coupled g-C_3N_4							
$Bi_7O_9I_3$/Bi_5O_7I/g-C_3N_4							
Hydrothermal	$C_3H_6N_6$, $Bi(NO_3)_3 \cdot 4H_2O$, $C_2H_6O_2$ and KI	Irregular rods consisting of thin irregular nanosheets	Crystal violet (10 ppm)	150 W Xe lamp	Binary heterojunction	Controlled synthesis of series of BiO_xI_y/g-C_3N_4 composites is reported	[163]
g-C_3N_4/BiOI/BiOBr							
Chemical precipitation	CH_4N_2O, $C_2H_6O_2$, $Bi(NO_3)_3 \cdot 5H_2O$, KBr and KI	Curved g-C_3N_4 nanosheets are attached to the surface of BiOI/BiOBr exhibiting sphere-like structures containing thin nanosheets of BiOI on large plates of BiOBr	Methyl orange (10 ppm) Escherichia coli (ATCC 15597)	300 W Xe lamp	Ternary heterojunction	Presence of BiOI shifted the bandgap to longer wavelength and also suppressed the carrier recombination	[164]
g-C_3N_4@BiOCl/$Bi_{12}O_{17}Cl_2$							
In situ self-assembly	CH_4N_2O, $BiCl_3$, C_2H_5OH and NaOH	Combination of layered and irregular microstructures having smooth nanosheets of different sizes are grown over g-C_3N_4	NO removal (1×10^{-9} ppb)	100 W commercial tungsten halogen lamp	Ternary heterojuncton	Electron spin resonance proved that both hydroxyl and superoxide radicals are active species towards NO removal	[165]
BiOI/BiOCl/g-C_3N_4							
Precipitation	$Bi(NO_3)_3 \cdot 5H_2O$, CH_4N_2O, KI, KCl and NH_3	Nanosheets are stacked densely to form irregular microstructures over thin layers of g-C_3N_4	Acid orange (10 ppm)	400 W Halogen lamp	Ternary heterojuncton	The optimal ratio of ternary hybrid was found to be 5:3:2	[91]

Table 1. *Cont.*

Synthesis Method	Precursors	Morphology	Contaminant Parameters	Light Source	Heterojunction Type	Significance of the Result	Ref.
Quaternary heterojunction							
$BiOCl/g\text{-}C_3N_4/Cu_2O/Fe_3O_4$							
Co-precipitation	$Bi(NO_3)_3{\cdot}5H_2O$, KCl, NaOH, HNO_3, $CuSO_4{\cdot}5H_2O$, C_2H_5OH, $FeCl_3$, $FeCl_2$ CH_4N_2S and $C_2H_6O_2$	Flower shaped BiOCl, spherical Fe_3O_4 and cubical Cu_2O nanoparticles are connected with porous sheets of $g\text{-}C_3N_4$	Sulfamethoxazole (100 µM)	800 W Xe lamp Natural sunlight	Quaternary nano-heterojunction	p-n-p junction functioned well under both artificial visible light and solar light towards sulfamethoxazole degradation	[166]
$g\text{-}C_3N_4/BiOI/BiOBr$							
Solvothermal	$C_2H_4N_4$, $C_2H_6O_2$, $Bi(NO_3)_3{\cdot}5H_2O$, KI and CTAB	$g\text{-}C_3N_4$ was attached to the surface of quadrate BiOBr substrates overlapped with rounded thin pieces of the BiOI	Methylene blue (20 ppm)	500 W Xe lamp	Ternary Z-scheme	Charge carrier dynamics in ternary composite is reviewed based on transient photocurrent response	[167]
Doped $BiOX\text{-}g\text{-}C_3N_4$							
K-doped $g\text{-}C_3N_4/BiOBr$							
In situ synthesis	CH_4N_2O, CTAB, KOH and $Bi(NO_3)_3{\cdot}5H_2O$,	2D nanosheets	Rhodamine B (20 ppm) Tetracycline (10 ppm)	500 W Xe lamp	Binary heterojunction	K was interfaced with $g\text{-}C_3N_4/BiOBr$ for improved migration and transportation of photogenic carriers	[168]
$g\text{-}C_3N_4@Bi/BiOBr$							
Solvothermal	$C_3H_6N_6$, $Bi(NO_3)_3{\cdot}5H_2O$, $C_2H_6O_2$, KBr and C_2H_5OH	3D fluffy and hierarchical structure where Bi/BiOBr nanoplates are embedded on the surface of the layered $g\text{-}C_3N_4$	Rhodamine B (20 ppm) Tetracycline (12 ppm)	Simulated sunlight	Ternary indirect Z-scheme	Ethylene glycol functioned as solvent and a reductant for tuning the morphology and boosting the photocatalytic performance	[84]
$g\text{-}C_3N_4@Polydopamine/BiOBr$							
Solvothermal	$C_3H_6N_6$, HCl, Da.HCl, NaOH, $Bi(NO_3)_3{\cdot}5H_2O$, PVP, $C_2H_6O_2$ and KBr	Flower-like BiOBr are deposited on the surface of sheet-like $g\text{-}C_3N_4@PDA$	Sulfamethoxazole (2.5 ppm)	300 W Xe lamp	Z-scheme	Biomimetic PDA as electron transfer mediator bridging $g\text{-}C_3N_4\text{-}BiOBr$ was reported for the first time	[169]

4.2. Carbon Dioxide Reduction

The rapid increase in the concentration of atmospheric CO_2 as a green-house gas has drawn significant concerns over its huge impact on the global climate. Therefore, the photocatalytic reduction of CO_2 to value-added chemicals such as CO, CH_3OH, HCOOH, CH_4, etc., under direct solar irradiation is pivotal for not only reducing the level of atmospheric CO_2, but also for partly fulfilling the renewable fuel demand that may increase in the future, partly owing to the steadily depleting fossil fuel reserves and also due to our environmental policy on curbing the usage of fossil fuels for inhibiting CO_2 emission. As mentioned earlier, BiOX photocatalysts are mainly employed for the photocatalytic degradation of organic pollutants and are seldom effective in the reduction of CO_2 conversion at neutral condition due to its positive CB position [170]. Therefore, only a few photocatalytic reduction reactions of pristine BiOX for photocatalytic CO_2 conversion have been reported to date [90,171–179]. On the other hand, theoretical studies indicated that the increase in the Bi-content in BiOX could promote the reduction power of photogenerated electrons and increase the thermodynamic force for initiating many reduction reactions that were not possible to be carried out with BiOX. In this regard, non-stoichiometric $Bi_xO_yX_z$ photocatalysts were found to exhibit promising potential in the photoreduction of CO_2 to solar fuels and exhibited good stability and possessed suitable band structures for extended visible light absorption with negative CB positions [180]. For instance, Ye et al. reported an enhanced rate of CO and CH_4 generation by the photocatalytic reduction of CO_2 using $Bi_4O_5Br_2$ microspheres assembled with ultrathin nanosheets in comparison to BiOBr with ultrathin nanosheets and bulk BiOBr. It was proved that Bi-rich $Bi_4O_5Br_2$ with a more negative CB position exhibited enhanced photoreduction of CO_2 in comparison to BiOBr. Further, it was revealed that the ultrathin nanosheet morphology of both $Bi_4O_5Br_2$ and BiOBr considerably reduced the recombination due to IEF generation and supported the generation of CO in comparison to bulk BiOBr [181]. Similarly, ultrathin $Bi_4O_5Br_2$ nanosheets synthesized through the molecular precursor method exhibited enhanced performance towards CO_2 reduction under visible light irradiation in comparison to bulk $Bi_4O_5Br_2$. The amount of CO_2 converted to CO was 63.13 µmol g^{-1} using $Bi_4O_5Br_2$ ultrathin nanosheets, which was ~2.3 times greater than that of bulk of $Bi_4O_5Br_2$ (27.56 µmol g^{-1}) [182]. The reason for the enhanced CO_2 reduction ability using $Bi_4O_5Br_2$ ultrathin nanosheets in comparison to its bulk counterpart was attributed to porous architecture with larger surface area, more negative CB position (−1.19 V), lower rate of recombination of the photogenerated charge carriers and higher photocurrent response. In another study, $Bi_4O_5I_2$ and Bi_5O_7I photocatalysts were successfully synthesized via hydrolyzation and calcination, respectively, using the molecular precursor method. Both $Bi_4O_5I_2$ and Bi_5O_7I exhibited the photocatalytic reduction of CO_2 to selectively generate CO, but the higher CB edge and lower bandgap energy (2.18 eV) of $Bi_4O_5I_2$ enabled it to exhibit enhanced photocatalytic performance that was ~11.5 and ~28.3 times greater than that of Bi_5O_7I and BiOI, respectively [183]. In addition to Bi-rich strategy, the hybridization of $Bi_4O_5I_2$ with g-C_3N_4 was employed for enhancing the photoreduction of CO_2 by the formation of a heterojunction with an I_3^-/I^- redox mediator synthesized through the complex precursor method. The composite exhibited higher photocatalytic activity for CO_2 conversion than pure g-C_3N_4 and $Bi_4O_5I_2$ owing to the I_3^-/I^- redox mediator formed in situ, which assisted the transfer of the photogenerated charge carriers through the Z-scheme heterojunction and suppressed their recombination [184]. The amount of CO generated by the photocatalytic reduction of CO_2 in the presence of g-C_3N_4/$Bi_4O_5I_2$ (20 wt%) with 45.6 µmol g^{-1} h^{-1} was ~7.9 and ~2.3 times greater than pristine g-C_3N_4 and pristine $Bi_4O_5I_2$, respectively. The performance of various BiOX/$Bi_xO_yX_z$-g-C_3N_4 heterojunction photocatalysts for the reduction of CO_2 is summarized in Table 2.

Table 2. Reduction of CO_2 in the presence of BiOX/$Bi_xO_yX_z$-g-C_3N_4 heterojunction photocatalysts reported in the literature.

Photocatalyst	Light Source	Result	Significance	Ref.
g-C_3N_4/$Bi_4O_5I_2$	300 W Xe lamp (λ > 420 nm)	Photoreduction of CO_2 CO—45.6 µmol g^{-1} h^{-1}	I_3^-/I^- redox mediator assisted Z-scheme mechanism enhanced the photocatalytic CO_2 conversion	[184]
g-C_3N_4/BiOI	300 W Xe lamp (λ > 420 nm)	Photoreduction of CO_2, CO—17.9 µmol g^{-1} h^{-1} O_2—9.8 µmol g^{-1} h^{-1}	Reduction in I content in the composite is unfavourable for the reduction of CO_2, implying I_3^- intermediate plays an important role in charge transfer process	[185]
g-C_3N_4/BiOBr/Au	300 W Xe lamp (λ > 420 nm)	Photoreduction of CO_2, CO—6.67 µmol g^{-1} h^{-1} CH_4—0.92 µmol g^{-1} h^{-1}	The size of Au nanoparticles acted as the Z-scheme bridge and SPR centre during the photocatalytic process.	[139]
g-C_3N_4/BiOCl-defect rich	300 W Xe lamp (λ > 420 nm)	Photoreduction of CO_2, CO—28.4 µmol g^{-1} h^{-1} CH_4—4.6 µmol g^{-1} h^{-1}	Interfacial oxygen vacancies provide a transport channel for the interfacial carriers, leading to a built-in electric field promoting enhanced carrier transfer efficiency.	[186]

4.3. Hydrogen Generation

Hydrogen as a fuel is considered a promising alternative for future energy sustainability owing to its high specific energy and eco-friendly combustion products. The positive CB position of BiOX photocatalysts restricts their ability to generate H_2, but precise control of their thickness during fabrication and the addition of defects such as oxygen vacancies were reported to simultaneously enhance the visible light absorption and intensity of the self-generated IEF [187–190]. For instance, Ye et al. synthesized black coloured ultrathin BiOCl nanosheets enriched with oxygen vacancies while glycerol reacted with the oxygen exposed on the (001) surface under hydrothermal conditions. The amount of H_2 generated using the black coloured ultrathin BiOCl (~2.51 μmol h^{-1}) under visible light irradiation was about 21 and 15 times higher than bulk BiOCl (0.12 μmol h^{-1}) and TiO_2 (0.16 μmol h^{-1}), respectively [191].

Li et al. reported the growth of BiOCl crystal with 18 facets, 24 vertices and 40 edges through a one-pot hydrothermal method for a longer reaction time of 100 h and, as observed from Figure 7, the amount of photocatalytic H_2 generated was 2.1 times greater than that obtained with BiOCl synthesized with a shorter time span of 10 h (5.99 μmol g^{-1} h^{-1}) [192]. Conventionally, the square plates of BiOCl with exposed {001} top facets correspond to the most positive CB position, while the lateral {110} facets form the most negative VB position, facilitating charge separation between in the binary {001}/{110} facet junction. On the other hand, the eighteen-faceted BiOCl were composed of {001} top facets and unusual {102} and {112} oblique facets owing to which the CB position was in the order (001) facet > (102) facet > (112) facet, while the VB position order was (001) facet < (102) facet < (112) facet. Therefore, the well-matched {001}/{102}/{112} ternary facet junction in the eighteen-faceted BiOCl facilitated the efficient cascade charge flow, ensuring enhanced photocatalytic H_2 generation. In another report, hierarchical BiOI microspheres synthesized through a microwave-assisted solvothermal method with ethylene glycol and ethanol as solvents were reported to exhibit visible light mediated photocatalytic water splitting to generate H_2 with maximum (1316.9 μmol g^{-1}) at pH 7 with a dosage of 0.2 gL^{-1}. The narrow bandgap of BiOI (2.04 eV) microspheres, the surprisingly sufficient overpotential due to negative CB position and the higher separation of the photogenerated charges aided H_2 generation [193]. Bai et al. synthesized non-stoichiometric $Bi_4O_5X_2$ (X = Br, I) nanosheets through the molecular precursor method, which generated H_2 under a 300 W lamp emitting simulated solar light irradiation [67]. Using 10% methanol as the sacrificial agent, the amount of H_2 generated with 40 mg of $Bi_4O_5Br_2$ and $Bi_4O_5I_2$ was 4.21 and 2.79 μmol g^{-1} h^{-1}, respectively. The enhanced photocatalytic performance of $Bi_4O_5Br_2$ nanosheets with a quantum efficiency of 0.93% at 420 nm in comparison to $Bi_4O_5I_2$ (just 0.52%) was attributed to the greater separation of photogenerated charge carriers. $Bi_{24}O_{31}Br_{10}$ nanoplates synthesized through the chemical precipitation method generated H_2 by the photocatalytic reduction of water at a rate of 3.3 μmol h^{-1} with 50 mg catalyst loading, while pristine BiOBr and Bi_2O_3 displayed no activity. The uplifting of the CB of $Bi_{24}O_{31}Br_{10}$ due to the presence of Bi 6p and Br 4s orbitals fulfilled the electric potential requirements for splitting water to H_2 in comparison to pristine BiOBr and Bi_2O_3 with positive CB positions [68]. Di et al. reported the synthesis of a defect-rich single-unit-cell of Bi_3O_4Br with a thickness of ~1.7 nm that displayed superior photocatalytic H_2 generation of up to 380 μmol g^{-1} h^{-1}, which was ~2 and 4.9 times greater than defect-deficient Bi_3O_4Br and bulk Bi_3O_4Br, respectively [97]. The enhanced photocatalytic activity of defect-rich single-unit-cell Bi_3O_4Br was immensely facilitated by the generation of oxygen defects due to bismuth vacancy in addition to their atomically thin architecture that favourably tuned the electronic band structure. In another study, a bilayer junction formed by the selectively assembly of metallic phase enriched MoS_2 and oxygen-deficient $Bi_{12}O_{17}Cl_2$ monolayers exhibited photocatalytic H_2 evolution at a rate of 33 mmol h^{-1} g^{-1} under visible light, with a superior quantum efficiency of 36% at 420 nm that was superior to the pristine monolayers of MoS_2 and $Bi_xO_yX_z$-based systems [194]. The enhanced performance of the bilayer $MoS_2/Bi_{12}O_{17}Cl_2$ junction can be attributed to the enhanced charge separation in oxygen-deficient $Bi_{12}O_{17}Cl_2$ monolayers ensured by the IEF and the collective role of both IEF and Bi-S bonds for pushing the electrons to catalyse the H_2 evolution. However, surprisingly, to date no reports have been found on photocatalytic H_2 generation using a $BiOX/Bi_xO_yX_z$-g-C_3N_4 heterojunction photocatalyst, given the fact that pristine g-C_3N_4 is an excellent H_2 evolution photocatalyst that has been studied extensively.

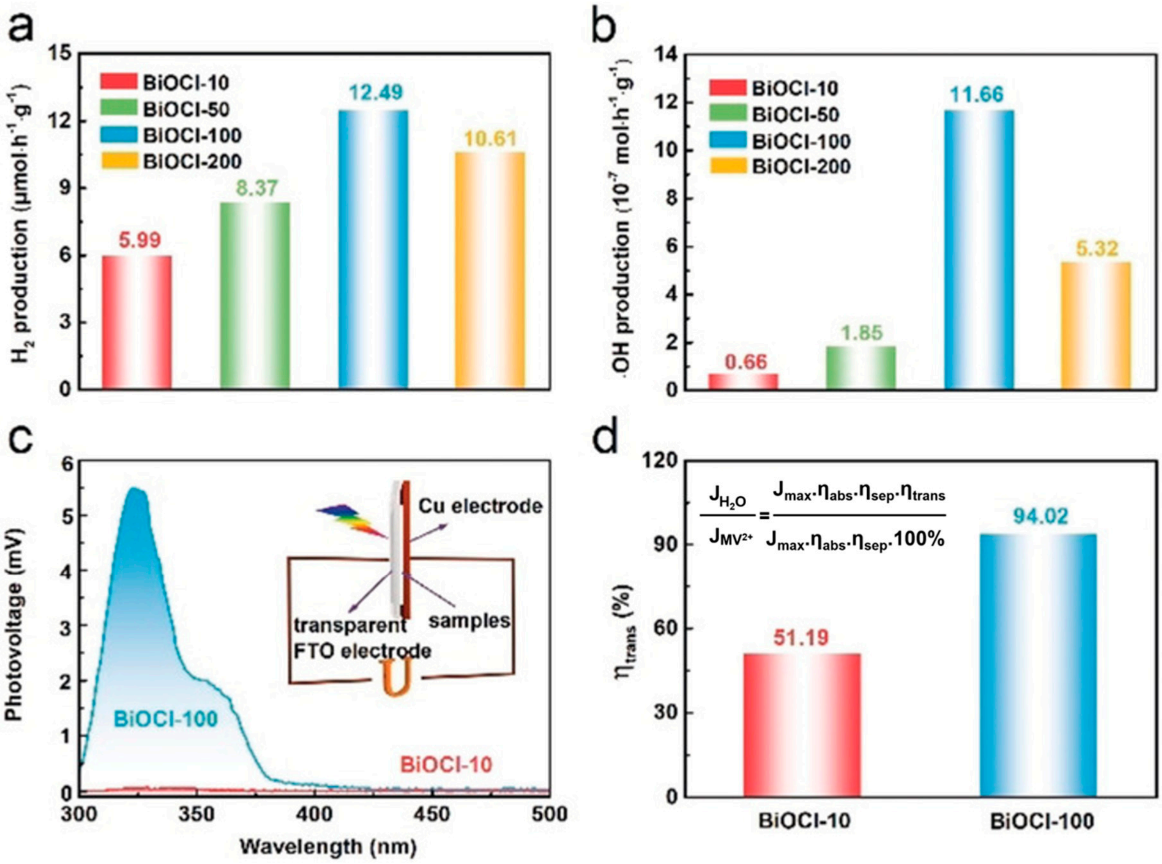

Figure 7. Rate constants for generation of (**a**) H_2 and (**b**) hydroxyl ions over different BiOCl photocatalysts under simulated solar light irradiation. (**c**) Surface photovoltage spectra of BiOCl synthesized with time span of 10 h (BiOCl-10) and 100 h (BiOCl-100) indicating the degree of charge separation. (**d**) Surface charge transfer efficiency of BiOCl-10 and BiOCl-100. Reprinted from Ref. [192] with permission from John Wiley & Sons.

4.4. Oxygen Evolution

In addition to H_2 generation, sunlight-driven photocatalytic water splitting allows the generation of oxygen (O_2). However, the water oxidation for O_2 evolution is more difficult due to the multistep transfer of four h^+ in comparison to the transfer of two e^- for H_2 generation. The oxygen evolution reaction demands the accumulation of cationic h^+ on the surface (i.e., surface-trapped holes), which is absolutely essential to be utilized for the reduction of adsorbed water via $H_2O_{ad} + 2h^+ \rightarrow {}^1/_2\, O_2 + 2H^+$ [195]. The basic requirement for photocatalytic O_2 evolution is ensuring that the VB edge of the photocatalyst is located at a more positive position than the oxidation potential of H_2O (1.23 V vs. normal hydrogen electrode at pH = 0). Further, a significant overpotential is required for overcoming the activation energies in the charge-transfer process between the photocatalyst and water molecules. Due to the stringent demands, only very few materials are capable of directly oxidizing water into O_2 under light irradiation. Di et al. reported the fabrication of atomically thin defect-rich BiOCl nanosheets through the hydrothermal approach by treating pre-synthesized BiOCl nanosheets in ethylene glycol and studied their performance towards the photooxidation of H_2O [196]. The amount of O_2 generated with defect-rich BiOCl nanosheets (56.85 μmol g^{-1} h^{-1}) was nearly 3 and 8 times greater than that generated with defect-free BiOCl nanosheets and bulk BiOCl. The enhanced performance of defect-rich BiOCl in the photooxidation of water can be attributed to the synergetic effect of an atomically thin thickness of ~2 nm, defects on BiOCl basal planes shortening the migration distance of holes for promoting charge separation and hole utilization, and the presence of abundant coordination-unsaturated active atoms. In another study, Ag and PdO_x nanocubes selectively deposited on the (001) and (110) facets of BiOCl nanoplates formed a ternary hybrid Ag-BiOCl-PdO_x photocatalyst that was employed in the photocatalytic O_2 evolution under visible light with $NaIO_3$ as the electron sacrificial agent [197]. Interestingly, Ag-(110)BiOCl(110)-PdO_x exhibited a highest average O_2 rate of 68.2 μmol g^{-1} h^{-1}, which was almost 5.9, 1.9 and 1.6 times higher than Ag-(001)BiOCl(001)-PdO_x, Ag-(001)BiOCl(110)-PdO_x and Ag-(110)BiOCl(001)-PdO_x, respectively. The schematic in Figure 8 illustrates the reasons for the enhanced photocatalytic O_2 generation, which can be attributed to stronger electronic coupling at the BiOCl(110)-based interfaces as a result of the thinner contact barrier between Ag and PdO_x and the shortest average hole diffusion distance realized by Ag and PdO_x on the BiOCl(110) plane.

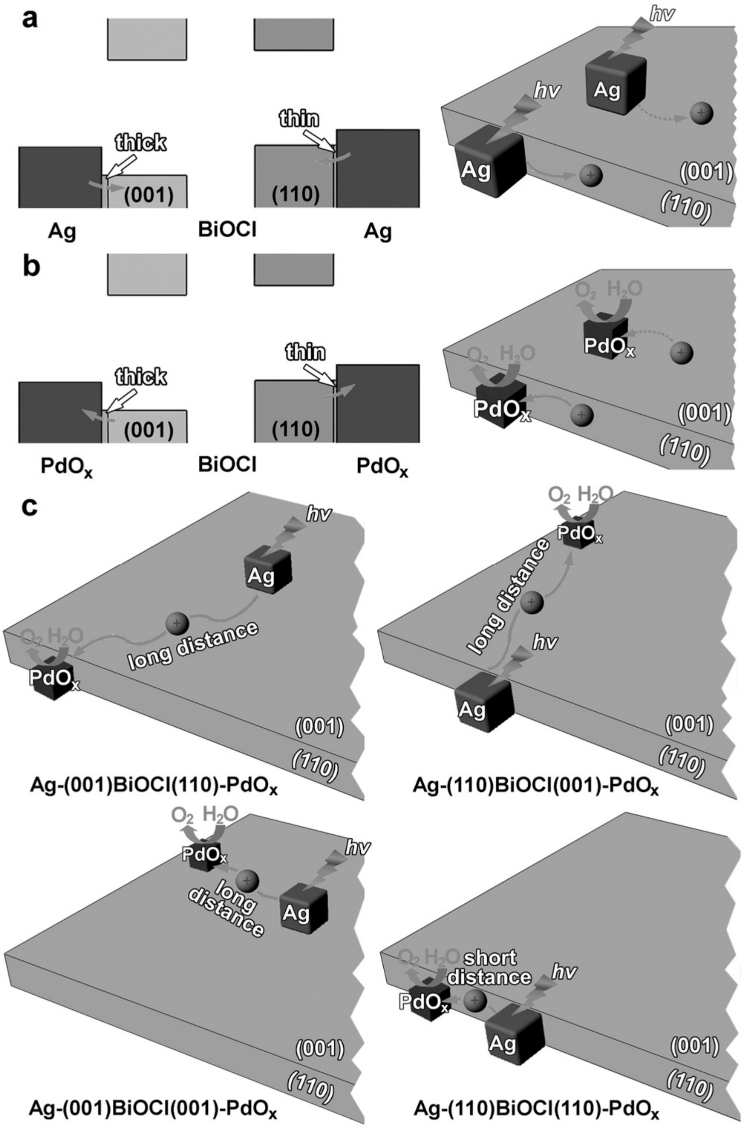

Figure 8. Schematic depicting the facet-dependent interfacial hole transfer ability as a result of the difference in thickness of the contact barrier layer on (**a**) Ag-BiOCl and (**b**) BiOCl-PdO_x interfaces. (**c**) Schematic representation of the different average diffusion distances of hole in different Ag-BiOCl-PdO_x photocatalysts. Reprinted from Ref. [197] with permission from John Wiley & Sons.

Cui et al. reported the solvothermal synthesis of BiOCl nanosheets with abundant oxygen vacancies using ethylene glycol as the solvent and studied their photooxidation ability [198]. The rate of O_2 evolved under visible light with oxygen vacancy-rich BiOCl nanosheets in the presence of $AgNO_3$ as the electron acceptor was 1.72 mmol g^{-1} after 5 h, which was 3.3 times higher than oxygen vacancy-poor BiOCl nanosheets despite the fact that their surface area was almost identical. Abundant oxygen vacancies in BiOCl nanosheets were reported to create many electron donor levels and allowed the excitation of electrons, which subsequently formed holes in the VB for the O_2 evolution reaction. Similarly, Ji et al. reported the synthesis of oxygen vacancy-rich and oxygen vacancy-less $Bi_7O_9I_3$ microspheres through the ionic liquid assisted solvothermal method and studied their performance in the photocatalytic O_2 evolution. As expected, the O_2 evolution rate of oxygen vacancy-rich $Bi_7O_9I_3$ microspheres at 199.2 μmol g^{-1} h^{-1} was ~1.5 times greater than that of oxygen vacancy-less $Bi_7O_9I_3$ microspheres, despite the fact that their surface area was comparable [199]. In another study, Bi_3O_4Br nanorings were synthesized through the solvothermal method using cetyltrimethylammonium bromide and polyvinyl pyrrolidone as surfactants, and their performance was assessed through photocatalytic O_2 evolution.

Interestingly, Bi_3O_4Br exhibited O_2 efficient oxygen evolution at a rate of 72.54 μmol g^{-1} h^{-1} that was attributed primarily to its single-crystalline nature, (001) facets exposure, ring structure, appropriate light response range and band potential, which facilitated the migration of charge carriers [200]. Ning et al. constructed a 2D-2D heterostructure photocatalyst by coupling Bi_3O_4Cl and BiOCl nanosheets through alkaline chemical etching and solvent exfoliation for O_2 evolution under visible light [201]. The rate of O_2 evolved with ultrathin Bi_3O_4Cl/BiOCl in the presence of $FeCl_3$ as the electron scavenger reached 58.6 μmol g^{-1} h^{-1}, which was about 3 times higher than that of nanocrystal Bi_3O_4Cl/BiOCl. Electron spin resonance spectroscopy detected $^{\bullet}O_2{}^{-}$ as the primary active species, which strongly suggested the mechanism of charge transfer during the photocatalytic oxidation reaction to be the Z-scheme heterojunction. In the Bi_3O_4Cl/BiOCl Z-scheme heterojunction, photogenerated electron-hole pairs generated by the built-in electric field under visible light irradiation enabled the rapid transfer of photogenerated electrons to the {001}-BiOCl facets that were partly trapped by Fe^{3+}, while the holes gathered on the {001}-Bi_3O_4Cl facets accommodated plenty of active sites for the photocatalytic O_2 evolution [201]. Though g-C_3N_4 has been extensively studied for its ability to oxidize water under light irradiation [202–204], it is unfortunate that no work on photocatalytic water oxidation has been carried out by designing suitable BiOX/$Bi_xO_yX_z$-g-C_3N_4 heterojunction photocatalysts. However, there is enough scope for constructing efficient heterojunction photocatalysts using BiOX/$Bi_xO_yX_z$ with exposed facets and functionalized g-C_3N_4 that could achieve enhanced quantum efficiencies.

4.5. Nitrogen Reduction

The photoreduction of nitrogen (N_2) to produce ammonia (NH_3), commonly referred to as nitrogen fixation, is a green alternative to the standard Haber–Bosch process, which consumes large amounts of fossil fuels and releases CO_2 into the atmosphere. Li et al. reported the solvothermal synthesis of {001} facet exposed BiOBr nanosheets with and without oxygen vacancies for studying their photocatalytic performance in reducing N_2 under visible light irradiation with water as the solvent and proton source. Interestingly, {001}-BiOBr without oxygen vacancies did not exhibit photocatalytic activity, while {001}-BiOBr with oxygen vacancies generated a significant amount of NH_3 at rate of 104.2 and 223.3 μmol g^{-1} h^{-1} under visible light and UV-vis light irradiation, respectively, with an external quantum efficiency of 0.23% at 420 nm [205]. N_2 was adsorbed on the oxygen vacancies by combining with the two nearest Bi atoms in the sublayer to form a terminal end-on bound structure, and the reduction capacity of N_2 over {001}-BiOBr was directly dependent on the amount of oxygen vacancies as they acted as catalytic centres capable of adsorbing and activating N_2 by inhibiting electron-hole recombination and promoting the interfacial charge transfer. Similarly, the Zhang group also studied photocatalytic N_2 fixation using oxygen vacancy-rich BiOCl nanosheets with {001} and {010} exposed facets and, interestingly, it was found that the rate of NH_3 generation with {010}-BiOCl (0.95 μmol g^{-1} h^{-1}) was only half of {001}-BiOCl (1.89 μmol g^{-1} h^{-1}), but after 30 min the rate of NH_3 generation with {010}-BiOCl at 2.29 μmol g^{-1} h^{-1} was 1.21 times greater than {001}-BiOCl. The reason for the slower rate of NH_3 generation during the initial 30 min was attributed to the different chemistry of N_2 fixation on {001} and {010} facets, while the enhanced NH_3 generation was attributed to the more stable side-on bridging of N_2 by combining with the two nearest Bi atoms in the outer layer and the nearest Bi atom in the sublayer on the (010) surface [206]. Bai et al. synthesized bismuth-rich Bi_5O_7I with {001} and {100} exposed facets through the solvothermal treatment of molecular precursors in glycerol, and studied their photocatalytic activity for N_2 fixation. The NH_3 generation rate using {001}-Bi_5O_7I (111.5 μmol g^{-1} h^{-1}) was ~2.3 times greater than {100}-Bi_5O_7I (47.6 μmol g^{-1} h^{-1}), and the apparent quantum efficiency was 5.1% at 365 nm. Band structure studies through VB X-ray photoelectron spectroscopy revealed the more negative CB position of {001}-Bi_5O_7I nanosheets that enhanced their reduction power, while the photocurrent response and electrochemical impedance spectroscopy results indicated their enhanced separation of photogenerated charge carriers and lower resistance for electron-transfer. Therefore, it was concluded that the enhanced photocatalytic N_2 fixation in Bi-rich $Bi_xO_yX_z$ was due to the facet effect in comparison to BiOX, wherein oxygen vacancies play a dominant role [207]. Another study on Bi-rich $Bi_xO_yX_z$ reported by Wang et al. demonstrated that engineering oxygen vacancies into Bi_5O_7Br nanotubes with a uniform diameter of ~5 nm could generate NH_3 up to 1.38 mmol h^{-1} g^{-1} under visible light with pure water without any organic scavengers or cocatalysts with an apparent quantum efficiency of over 2.3% at 420 nm [83]. Interestingly, the Bi_5O_7Br nanotube dispersion in water exhibited a colour change from light yellow to dark grey under light irradiation that induced oxygen vacancies by seizing O atoms from water. In addition to the more negative CB position, the enhanced chemisorption of N_2 on the oxygen vacancy sites due to the large surface area of Bi_5O_7Br nanotubes (96.56 m^2 g^{-1}), forming a bond with Bi-metal (sideward transition metal), enabled it to donate electrons from its bonding orbitals and accept electrons to its antibonding π-orbitals, which gradually wakened the N-N triple bond due to electron exchange and led to the enhanced generation of NH_3. Zhang et al. reported photocatalytic N_2 fixation by simultaneously introducing oxygen vacancy and doping Fe into BiOCl nanosheets that generated NH_3 at a rate of 1.02 mmol g^{-1} h^{-1} under light irradiation using a 300 W Xe lamp [208]. The mechanism of N_2 fixation was similar to the report on Bi_5O_7Br nanotubes, and the dispersion of Fe-doped BiOCl also exhibited a colour change from white to dark grey under light irradiation for the generation of oxygen vacancies. Typically, the N_2 fixation involved four main steps, viz., (i) the generation of oxygen vacancies on the catalyst surface during light irradiation, (ii) the chemisorption of N_2 on the catalyst surface activated by oxygen vacancies, (iii) the injection of photogenerated electrons into the orbitals of activated N_2 for their reduction, and (iv) the refilling of oxygen vacancies by adjacent O atoms from H_2O or O_2. Similarly, Fe-doped BiOBr microspheres composed of nanosheets were synthesized through the solvothermal method with polyethylene glycol for the photocatalytic conversion of N_2 to NH_3 at a rate of 382.68 μmol^{-1} g^{-1} h^{-1}, which was eight times greater than pristine BiOBr (51.6 μmol^{-1} g^{-1} h^{-1}), under visible light radiation obtained from a 300 W xenon lamp equipped with a 420 nm cutoff filter [209]. The charge density map of Fe-doped BiOBr nanosheets shown in Figure 9a indicated that Fe withdrew electrons from nearby atoms to form electron-rich Fe(II) that injected localized electrons to the π N-N antibonding orbital of the adsorbed N_2 via electron donation for obtaining enhanced NH_3 generation, as observed from Figure 9b. Further, the more negative CB position of Fe-doped BiOBr nanosheets (Figure 9c) in comparison to pristine BiOBr and enhanced visible light absorption demonstrated the vital role played by Fe atoms. Similar to defect-rich nanostructures of BiOX and $Bi_xO_yX_z$, defect-rich g-C_3N_4 has demonstrated excellent performance in the photocatalytic N_2 fixation under visible light [210,211]. However, to date no work has been reported on photocatalytic N_2 fixation with suitable BiOX/$Bi_xO_yX_z$-g-C_3N_4 heterojunction photocatalysts, which allows room for significant research to be conducted in this direction.

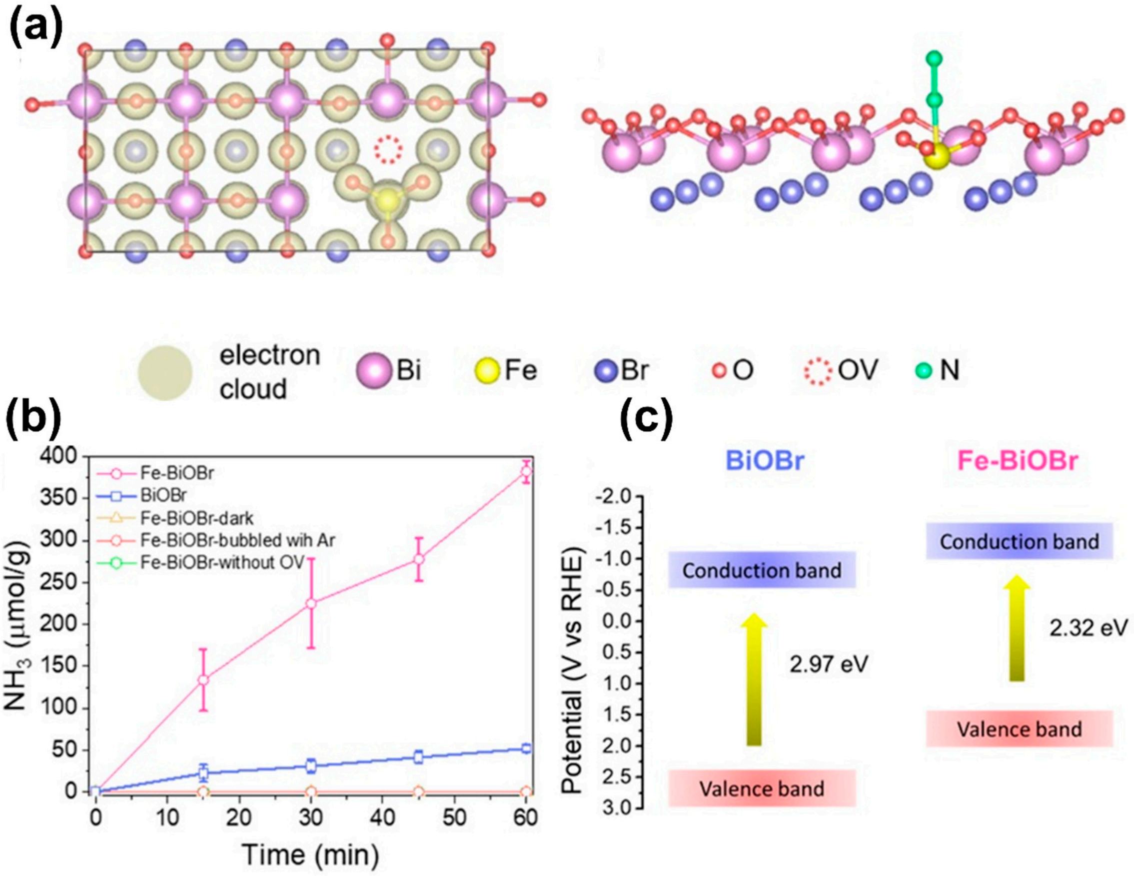

Figure 9. (**a**) Charge density map of Fe-doped BiOBr nanosheets and the schematic of N_2 binding to the oxygen vacancy connected Fe atom in Fe-BiOBr, (**b**) plot depicting the photocatalytic NH_3 generation using Fe-doped BiOBr nanosheets and (**c**) band structure of BiOBr and Fe-doped BiOBr nanosheets. Reprinted from Ref. [209] with permission from American Chemical Society.

4.6. Organic Synthesis

Semiconductor-based photocatalysis to achieve highly efficient organic reaction has gained significant research attention. The oxidation of alcohols to their corresponding aldehydes is the major area of organic synthesis. Xiao et al. hydrothermally synthesized nanobelt-like structures of $Bi_{12}O_{17}Cl_2$ and evaluated their performance towards the photocatalytic oxidation of benzyl alcohol in acetonitrile to benzaldehyde under visible light at 50 °C. The bandgap energy of the $Bi_{12}O_{17}Cl_2$ photocatalyst was found to be 2.43 eV, and the conversion rate to benzaldehyde was 44% under oxygen atmosphere via direct hole oxidation. When $Bi_{12}O_{17}Cl_2$ nanobelts were subjected to visible light irradiation, the e^- excited to the CB would be trapped by electrophilic O_2, while the h^+ in the VB reacted with alkoxide anions to form carbon radicals through deprotonation, and, subsequently, benzaldehyde was formed by the reaction of these carbon radicals with h^+ [212]. Han et al. reported the synthesis of BiOBr photocatalysts with three different exposed facets, viz., {001}, {010} and {110} for the selective aerobic photooxidation of benzylamine in acetonitrile solution to N-benzylidenebenzylamine at room temperature and atmospheric air as the oxidizing agent. Although BiOCl and BiOI were found to exhibit almost 100% selectivity for the photooxidation of benzylamine, only BiOBr exhibited 100% conversion and selectivity. Results indicated that the orientation of the exposed planes played a significant role as BiOBr-{001} exhibited the highest activity based on unit surface area. However, solvothermally synthesized BiOBr-{110} microspheres achieved 100% selectivity and conversion efficiency in the oxidation of benzylamine due to their high surface area [213]. BiOBr nanoplates with (001) exposed facets synthesized through the modified hydrothermal approach were treated in O_2 and inert atmosphere for fabricating defect-free and defect-rich BiOBr. Interestingly, the defect-rich BiOBr nanoplates exhibited high efficiency and selectivity for the oxidation of benzylamine to N-benzylidenebenzylamine, while the yield of corresponding imine was much lower with defect-free BiOBr. Photoluminescence spectroscopy and photoelectrochemical studies confirmed that oxygen-vacancy mediated exciton dissociation resulted in promoted charge-carrier generation in the system that led to a selective oxidative-coupling reaction through $^{\bullet}O_2{}^{-}$ generation [214]. Similarly, BiOCl colloidal ultrathin nanosheets with hydrophobic surface properties fabricated with abundant oxygen vacancies by the hydrolysis of $BiCl_3$ in octadecylene solution enabled them to display superior photocatalytic activity for the aerobic oxidation of secondary amines to corresponding imines under visible light irradiation [215]. $Bi_{24}O_{31}Br_{10}(OH)_{\delta}$ microspheres containing porous nanosheet substructures with a surface area of 45 m^2g^{-1} and abundant active lattice oxygen sites were reported to exhibit the selective photooxidation of various alcohols in air under visible light irradiation [216]. Mott–Schottky analysis suggested the thermodynamically feasible band structure of $Bi_{24}O_{31}Br_{10}(OH)_{\delta}$, while its loose and porous architecture allowed the easy diffusion of bulky alcohols for accessing the abundant active surface sites. Therefore, a remarkably high quantum efficiency of 71% was achieved under visible light irradiation for isopropanol oxidation. A BiOBr/g-C_3N_4 heterojunction photocatalyst synthesized through a two-step combustion-coprecipitation method was reported to exhibit excellent photooxidation of benzylamine to N-benzylidenebenzylamine with a conversion rate of 94% and a yield of 82% within 4 h of visible light irradiation obtained from white LED under atmospheric air [217]. The enhanced performance of the BiOBr/g-C_3N_4 photocatalyst was ascribed to the improved charge transfer and separation driven by its apt band structure. Interestingly, bezylamine oxidation happened under both aerobic and anaerobic conditions driven by the $^{\bullet}O_2{}^{-}$ radicals (produced by the reaction of CB e^-) with amine cations and the reaction of VB h^+ with nitrogen-centred radicals, respectively, to form N- benzylidenebenzylamine.

5. Strategies for Improving the Performance of BiOX/$Bi_xO_yX_z$-g-C_3N_4 Heterojunction Photocatalysts

The photocatalytic performance of BiOX/$Bi_xO_yX_z$ nanomaterials has received substantial research interest owing to their suitable band structure for absorbing sunlight to start the photocatalytic reaction. Unfortunately, their practical applications are still confined by a few drawbacks, including a mismatch between the band edge position and light harvesting, ineffective charge separation and transportation, fewer active sites, and poor selectivity of the desired reaction. In this context, numerous strategies have been developed to engineer the layered structure and overcome the aforementioned drawbacks. The following sections emphasize each strategy accordingly.

5.1. Microstructure Modulation

Due to the strong connection between the physical and chemical properties and the microstructure (shape, size, surface area, and dimensionality) of the materials, the rational synthesis of the nano- or microstructure has constantly received great significance from the prospect of both scientific research and industrial applications. Further, the inherent nature of nanoscale materials to exhibit higher surface-to-volume ratio and provide abundant active sites enables the effective separation of the photoinduced carriers, thereby enhancing their photocatalytic efficiency. Table 1 provides the summary of various methods for fabricating BiOX/$Bi_xO_yX_z$-g-C_3N_4 heterojunction photocatalysts which were briefly introduced in Section 4.1. Since many articles have already reviewed the importance of microstructure modulation, our discussions in this section are confined to just a few articles mainly focusing on the fabrication of the heterojunction between BiOX/$Bi_xO_yX_z$

and g-C_3N_4. In addition to the conjunction 2D-2D heterojunction, the embedment of 3D hierarchical structures on 2D structures has also sparked interest owing to the distinctive 3D architecture formed by the self-assembly of 1D and 2D sub-structures.

For example, a Bi_5O_7I/g-C_3N_4 heterojunction photocatalyst was synthesized by two different approaches, adopting in situ co-thermolysis [106] and the one-pot ethylene glycol assisted hydrothermal approach [107]. In the in situ co-thermolysis method, BiOI precursor (pre-synthesized through the coprecipitation method) was mixed with melamine and ground with an agate mortar, and the powdered material taken in a crucible was heated in a muffle furnace at 520 °C for 4 h for obtaining Bi_5O_7I/g-C_3N_4. On the other hand, in the one-pot ethylene glycol assisted hydrothermal approach, a final solution of ethylene glycol made by the dropwise addition of KI solution to a solution containing $Bi(NO_3)_3{\bullet}5H_2O$ with pre-synthesized g-C_3N_4 was treated hydrothermally at 150 °C for 12 h. Interestingly, the morphology of the final structure of Bi_5O_7I/g-C_3N_4 resembled microspheres with nanosheet substructures of the individual components. Additionally, interestingly, the estimated values of the VB and CB potentials for g-C_3N_4 (1.54 eV and -1.19 eV) and Bi_5O_7I (3.17 eV and 0.29 eV) were identical. However, the mechanism of charge transfer described for the Bi_5O_7I/g-C_3N_4 heterojunction photocatalyst synthesized through in situ co-theromolysis was ascribed to the type-II heterojunction, while the charge transfer mechanism in hydrothermally synthesized Bi_5O_7I/g-C_3N_4 was ascribed to the Z-scheme. In another study, BiOBr/g-C_3N_4 heterojunction photocatalysts were fabricated by dispersing pre-synthesized BiOBr nanoflowers enriched with oxygen vacancies synthesized by the solvothermal treatment of precursors ($Bi(NO_3)_3{\bullet}5H_2O$, polyvinylpyrrolidone and KBr) dispersed in mixed solvent (ethylene glycol and water) at 160 °C for 3 h, in g-C_3N_4 dispersion and stirring at room temperature for 6 h, followed by washing and drying [218].

TEM analysis indicates the layered g-C_3N_4 structure with ultrathin nanosheets (Figure 10a), the nanoflower-like morphology of BiOBr enriched with oxygen vacancies (Figure 10c) and their perfect heterojunction, indicating the embedment of the oxygen vacancy enriched nanoflowers on g-C_3N_4 nanosheets (Figure 10d). Comparatively, the morphology of defect-free BiOBr/g-C_3N_4 indicates the formation of nanoplates, as observed from Figure 10b. HRTEM micrographs (Figure 10e,f) of oxygen vacancy enriched BiOBr/g-C_3N_4 depict the lattice spacing of d = 0.28 and 0.352 nm corresponding to the (102) and (101) crystal planes of the tetragonal phase of BiOBr, respectively. Further, the purity and co-existence of all the elements in BiOBr/g-C_3N_4 were confirmed from EDS elemental mapping, as shown in Figure 10g. The photocatalytic activity of oxygen vacancy enriched BiOBr/g-C_3N_4 in the removal of NO under visible light irradiation at 63% was 1.8, 1.6, 1.6 and 1.5 times greater than pristine g-C_3N_4, pristine oxygen vacancy enriched BiOBr, defect-free BiOBr/g-C_3N_4 and a physical mixture of g-C_3N_4 with oxygen vacancy enriched BiOBr. Similarly, photocatalytic CO_2 reduction using oxygen vacancy enriched BiOBr/g-C_3N_4 generated CO and CH_4 at a rate of 61.8 and 27.1 $\mu molh^{-1}g^{-1}$, respectively, which was greater than the control samples. Abundant oxygen vacancies in BiOBr and the heterojunction with ultrathin g-C_3N_4 nanosheets were attributed to the enhanced photocatalytic activity, while the $^{\bullet}OH$ and $^{\bullet}O_2^-$ radicals were reported to be the main active species involved in the removal of NO and the reduction of CO_2, respectively.

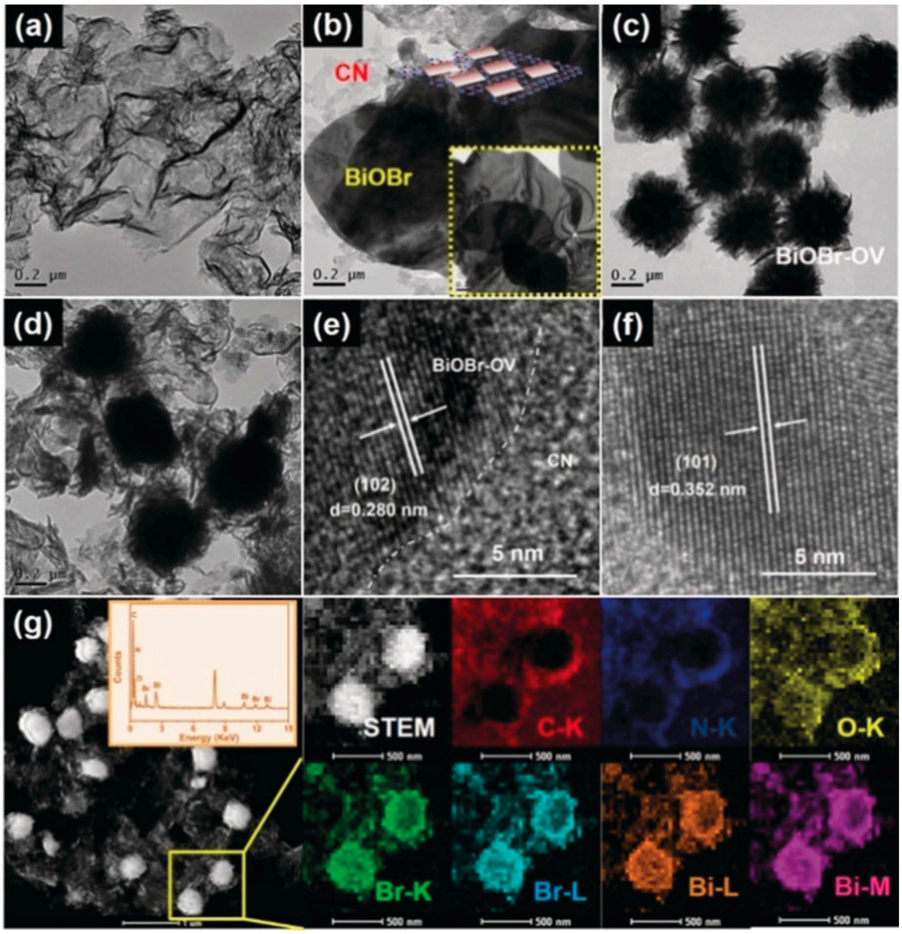

Figure 10. TEM micrographs of (**a**) pristine g-C_3N_4, (**b**) defect free-BiOBr/g-C_3N_4, (**c**) pristine BiOBr enriched with oxygen vacancies, (**d**) oxygen vacancy enriched BiOBr/g-C_3N_4, (**e**,**f**) HRTEM micrographs of oxygen vacancy enriched BiOBr/g-C_3N_4 depicting the lattice spacing and (**g**) the corresponding elemental maps of C, N, O, Br and Bi. Reprinted from Ref. [218] with permission from Wiley-VCH.

5.2. Facet and Defect Control

Crystal facets are an important feature of crystalline materials, and different crystal facets have different geometric and electronic structures, exhibiting intrinsic reactivity and surface physical and chemical properties associated with the crystallographic orientation. As a basic feature of crystalline materials, the exposed crystal facets play an important role in photocatalytic efficiency since photocatalysis occurs on the surface of BiOX photocatalysts. BiOCl nanosheets with tunable {001} facet percentages were synthesized by hydrolyzing molecular precursors $Bi_n(Tu)_xCl_{3n}$ (Tu = thiourea). Exposed {001} facets of BiOCl exhibited high oxygen atom density, and under UV light irradiation, plenty of oxygen vacancy sites were created [219]. These oxygen vacancies formed a defect state near the bottom of the CB of BiOCl and played a significant role in capturing the photogenerated electrons for enhancing the photocatalytic activity of BiOCl due to the improved separation of photogenerated charge carriers. Jiang et al. reported the hydrothermal synthesis of BiOCl single-crystalline nanosheets with exposed {001} facets, which exhibited higher activity for direct semiconductor photoexcitation pollutant degradation under UV light, while the counterpart with exposed {010} facets possessed superior activity for indirect dye photosensitization degradation under visible light [220]. Zhao et al. obtained rose-like BiOBr nanostructures with exposed {111} facets using sodium dodecyl sulphate as the surfactant, which exhibited better photocatalytic activity than exposed {001} facets under both visible light and monochromatic light [221]. Although high-energy facets exhibited higher activity than low-energy facets, they are easily eliminated because the fastest crystal growth would occur in the direction perpendicular to the high-energy facet. Therefore, glucose as the capping and structure-directing agent was employed in synthesizing 1D rod-like BiOBr with exposed {110} facets, and it was revealed that glucose not only suppressed the growth of {001} facets of BiOBr nanosheets but also induced these nanosheets to self-assemble along the [1] orientation, displaying better photocatalytic activity towards the photodegradation of rhodamine B and methyl orange [222]. Defects in the exposed facets of semiconductors can significantly enhance the photocatalytic activity by changing their electronic structures, the recombination efficiency of charge carriers, and surface properties [223]. As a typical defect, oxygen vacancies are reported to enhance the photo-absorption and photocatalytic performance of the photocatalysts. Li et al. reported the fabrication of BiOBr nanosheets with oxygen vacancies via a hydrothermal-reduction route. Their study revealed that only those oxygen vacancies created on the surface of the photocatalyst could inhibit the charge carrier recombination by trapping the photogenerated electrons, while the bulk oxygen vacancies which can also trap photogenerated charges act as recombination centres, resulting in a decrease in photoactivity [205]. Wang et al. reported the introduction of surface oxygen vacancies over the BiOBr nanosheets exposed with {001} facets by surface modification using polybasic carboxylic acids. These surface oxygen vacancies on BiOBr intensified the separation efficiency of photogenerated carriers and promoted the dioxygen reduction towards the degradation of MO dye [224]. Further, density functional theory calculations revealed that the presence of oxygen vacancies can ensure the increased density of states at the conduction band edge relative to the BiOBr atomic layers and bulk counterpart, which helps in enhancing the electron transport pathways.

Additionally, the introduced oxygen vacancies created new defect levels which allowed a narrower bandgap, hence giving the possibility for realizing visible light CO_2 reduction. Wu et al. reported that oxygen-deficient BiOBr atomic layers triggered visible-light-driven CO_2 reduction into CO with a rate of 87.4 μmol g^{-1} h^{-1}, which was 20 times and 24 times higher than that of BiOBr atomic layers and bulk BiOBr. Thus, defect engineering was proved to promote CO_2 photoreduction efficiency through fully addressing the poor photo-absorption, sluggish electron-hole separation, and high CO_2 activation barrier, giving new possibilities for achieving high performance in solar CO_2 reduction [225].

Li et al. reported the synthesis of a BiOCl single crystal with eighteen-facets by prolonging the hydrothermal reaction time (10–200 h), which exhibited enhanced H_2 generation that was higher than previously reported BiOCl with a [1] top facet and [121] lateral facets. SEM micrographs of BiOCl crystals synthesized at different time intervals are represented in Figure 11a–d. Both TEM and HRTEM micrographs confirmed the formation of well-shaped oblique facets at an angle of ~45° from the top facets, as observed from Figure 11e–h. The schematic illustration of eighteen-faceted BiOCl and the {001}, {102} and {112} facets in BiOCl is represented in Figure 11i,j. The well-indexed XRD patterns indicated the formation of a pure phase of BiOCl (Figure 11k). Therefore, with the help of the ternary facet junction, the electron-hole pairs in the eighteen-faceted BiOCl single crystal were effectively separated and displayed outstanding photocatalytic activity in the generation of H_2 [192].

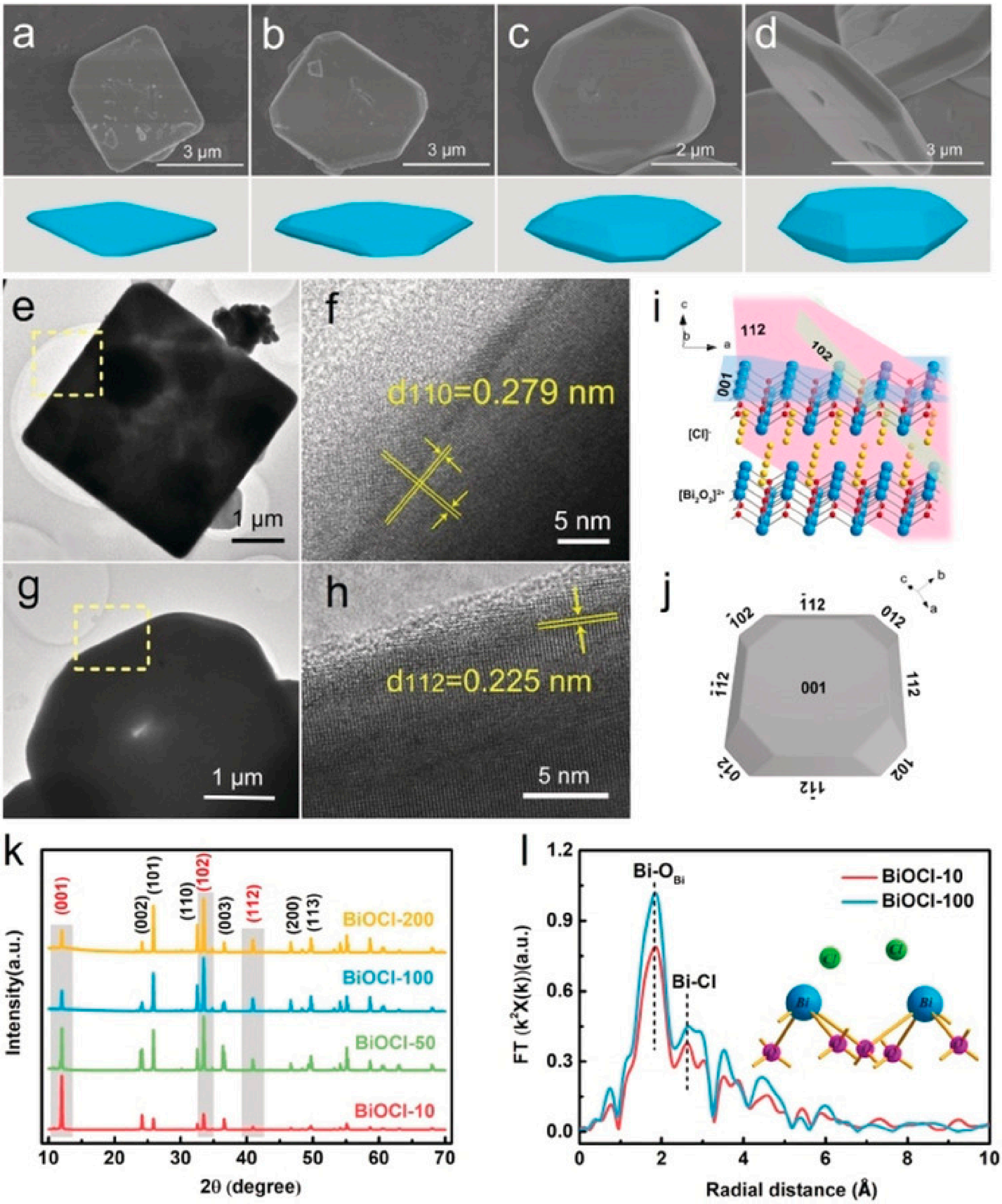

Figure 11. SEM images and the corresponding schematic representation for BiOCl treated at different time intervals (**a**) 10 h, (**b**) 50 h, (**c**) 100 h, and (**d**) 200 h; (**e**) TEM image and (**f**) HRTEM image of BiOCl treated for 10 h; (**g**) spherical aberration correction TEM image and (**h**) HRTEM image of BiOCl treated for 100 h; (**i**) crystal structure and facets of BiOCl; (**j**) Schematic representation of the different facets of eighteen-faceted BiOCl; (**k**) XRD patterns of BiOCl series samples; (**l**) Fourier transformed profiles for Bi coordination environments in normalized Bi L3-edge XAFS spectra of BiOCl treated at 10 and 100 h. Reprinted from Ref. [192] with permission from John Wiley & Sons.

5.3. Integration with Noble Metal Nanostructures

Depositing the noble metal over the surface of the semiconductor surface is an effective approach for modifying the photon harvesting capacity and for increasing the charge carrier separation kinetics. Noble metals coupled with semiconductor photocatalysts could form a high-speed charge-transfer channel for accelerated transport. Further, in many semiconductor systems, the noble metal nanoparticles have been usually used as charge-transfer mediators owing to their excellent electron conductivity, thereby offering a new approach to overcome the limit of traditional heterojunction photocatalysts. Additionally, due to the unique phenomenon of surface plasmon resonance (SPR) and its induced local electric field, the noble metal nanoparticles bridged with semiconductor photocatalysts can strengthen the photon absorption range and boost the photoinduced electron transfer [226,227]. Jiang et al. coupled Pt nanoparticles as the apt co-catalyst in the ternary Z-scheme photocatalytic system with BiOI (5.65 eV) and g-C_3N_4 (4.52 eV), since the work function of Pt (5.20 eV) was in between that of the individual semiconductors. Interestingly, the efficiency of the BiOI/Pt/g-C_3N_4 system was much higher than that of pristine g-C_3N_4, Pt/g-C_3N_4, and BiOI/g-C_3N_4 in the photodegradation of phenol and tetracycline hydrochloride, which was attributed to the efficient separation and transfer of charge carriers in an unobstructed Z-scheme route. The electric fields in the opposite direction for Pt/BiOI and Pt/g-C_3N_4 interfaces were formed due to the difference in the work function. The higher work function of Pt in contact with g-C_3N_4 formed a Schottky barrier and forced the transfer of electrons accumulated in the space charge region, resulting in the upward band bending in the Pt/g-C_3N_4 interface. Similarly, the depletion layer at Pt/BiOI was formed due to the higher work function of BiOI in comparison to Pt. Under visible light irradiation, the inverse electric field at Pt/g-C_3N_4 and Pt/BiOI would induce the e^- in BiOI and h^+ in g-C_3N_4 to combine at the Pt metal. Since this charge transfer process occurred without overcoming the Schottky barrier, it was termed as an unobstructed Z-scheme heterojunction and enabled the photogenerated e^- in the CB of g-C_3N_4 and h^+ in the VB of BiOI to form $^\bullet O_2{}^-$ and $^\bullet OH$ radicals that efficiently degraded the organic contaminants [136].

5.4. Carbonaceous Materials Compounding

Carbonaceous materials, such as graphene, carbon nanotubes (CNTs), carbon quantum dots (CQDs), carbon fibres, multi-walled carbon nanotubes (MWCNTs), carbon spheres, etc., are reported to play a vital role in enhancing the photocatalytic performance of BiOX/$Bi_xO_yX_z$ nanomaterials [94,145,147,148]. Graphene or reduced graphene oxide (rGO) has been considered a good electron collector and charge transport medium in photocatalysis owing to its high conductivity, excellent electron mobility, and large specific surface area. BiOCl/carbon-based photocatalysts have gained enormous interest due to their enhanced performance, which was attributed to their strong adsorption, excellent light absorption, and rapid transfer of photogenerated charges [228,229]. A BiOCl/CQDs/rGO ternary heterojunction photocatalyst driven by visible light exhibited enhanced ciprofloxacin removal efficiency, which was attributed to the excellent adsorption, enhanced charge separation and charge injection induced by the presence of CQDs and rGO. The photocatalytic efficiency of BiOCl/CQDs/rGO was 3.8 and 10.4 times greater in comparison to BiOCl/CQDs and BiOCl, respectively, while the removal efficiency was ~87% [230]. Yu et al. hydrothermally synthesized 3D BiOBr/rGO heterostructured aerogel using dopamine as both a reducing agent and cross-linker. The rate of the photodegradation of MO (80%) using 3D BiOBr/rGO was much higher compared to RhB (50%) and phenol (35%) under 60 min of visible light irradiation. Strong π-π interaction through the conjugative aromatic structure was attributed to the highly efficient selective adsorption of anionic MO [231]. Similarly, the addition of 1 wt% rGO relative to BiOBr sheets with exposed {001} facets with a core/shell structure exhibited the highest activity for the photodegradation of orange II dye (97% in 90 min) and the removal of acetaminophen (93% in 105 min). The enhanced photocatalytic activity of (1 wt%) rGO/BiOBr was attributed to increased visible light absorption, effective separation, the transportation of photogenerated charge carriers and the formation of a Schottky barrier at the interface between BiOBr and rGO, which enabled the transfer of e^- from the CB of BiOBr to rGO (due to its higher work function) and the internal electric field at the interface. The capability of rGO to store and shuttle e^- enabled the formation of $^\bullet O_2{}^-$ radicals by reacting with adsorbed O_2 molecules, while allowing the h^+ to react with OH to form $^\bullet OH$, the two main species responsible for the oxidation of organic contaminants [232]. Z-scheme heterojunction photocatalysts with solid-state electron mediators bridging two semiconductors were proposed for enhancing the performance through the efficient transport and separation of the photogenerated charge carriers. For instance, a

2D/2D Z-scheme heterojunction was constructed between BiOBr and g-C_3N_4 using carbon dots as the solid-state electron mediator, and it exhibited enhanced photocatalytic performance in the degradation of ciprofloxacin (~84% in 105 min) and tetracycline (~83% in 60 min) under visible light degradation. Under visible light irradiation, the photogenerated e^- in the CB of BiOBr with low reduction ability and photogenerated h^+ in the VB of g-C_3N_4 with low oxidation ability are transferred to the carbon dots, while the e^- and h^+ with high reduction and oxidation ability produce $^{\bullet}O_2^-$ and $^{\bullet}OH$ active species that react with the organic contaminants for their mineralization into CO_2 and H_2O [145]. Similarly, the unique electron mediating feature of carbon dots coupled with BiOBr (20 wt%) and g-C_3N_4 nanosheets facilitated the improved separation of photogenerated charge carriers for superior performance towards the degradation of organic contaminants (rhodamine B, methylene blue and methyl orange) and the photoreduction of Cr(VI) to Cr(III) under visible light, with $^{\bullet}O_2^-$ and $^{\bullet}OH$ being the active species [94]. Likewise, rGO was employed as an electron transfer mediator in the heterojunction formed between BiOBr (10 wt%) with protonated g-C_3N_4 for the photodegradation of tetracycline (59% mineralized) and BiOCl with protonated g-C_3N_4 for the photodegradation of tetracycline (96% in 180 min) and the selective oxidation of benzyl alcohol (conversation rate 76% and selectivity 99%). In both cases, the mechanism of photocatalysis followed the Z-scheme heterojunction, with $^{\bullet}O_2^-$ and $^{\bullet}OH$ being the primary active species [144,233]. On the other hand, MWCNTs were also reported to have been employed as electron mediators in the heterojunction between g-C_3N_4 and BiOI (20 wt%). The heterojunction exhibited improved visible light photocatalytic activity towards the degradation of methylene blue (10 ppm, 70% in 3 h) under visible light (>420 nm) through the Z-scheme mediated charge transfer [142]. A p-n junction formed by coupling g-C_3N_4 and BiOBr with rGO as the conductive support exhibited enhanced photocatalytic activity in the degradation of rhodamine B (10 ppm, 66% in 60 min) under visible light. The sp^2-hybridized carbon atoms in graphene capable of storing and shuttling electrons enabled the photogenerated electrons from the CB of BiOBr to flow into it and formed a Schottky barrier at the interface for preventing their backflow. Meanwhile, the electrons with high reduction potential and holes with high oxidation potential reacted with dissolved O_2 and OH^- to form $^{\bullet}O_2^-$ and $^{\bullet}OH$ radicals, which were actively involved in the photodegradation of rhodamine B [146]. In comparison to CNTs, carbon dots and rGO, mussel-inspired biometric carbon material polydopamine, also possessing a conjugated π structure and good electron transport ability, has attracted significant interest owing to its excellent adhesion ability, strong light-harvesting capacity, photoconductivity and biocompatibility. The Z-scheme heterojunction photocatalyst g-C_3N_4@polydopamine/BiOBr showed high activity in the photocatalytic degradation of sulfamethoxazole under visible light. Polydopamine was reported to promote the efficient separation of the photogenerated charge carriers for ensuring efficient redox capability of the photocatalyst, while the mechanism studied through radical quenching experiments confirmed that the h^+ and $^{\bullet}O_2^-$ were the major reactive species for oxidizing sulfamethoxazole [169].

5.5. Integration of Other Semiconductor Nanostructures

Single component photocatalysts fail to exhibit higher photocatalytic efficiency due to the rapid recombination of the photogenerated charge carriers. In order to achieve enhanced photocatalytic efficiency, one of the most common strategies is to construct a heterojunction photocatalytic system by coupling two or more semiconductors [234]. Typically, in a heterojunction photocatalytic system, the photogenerated electrons in the CB of photocatalyst A migrate to the CB of photocatalyst B, while the photogenerated holes in the VB of photocatalyst B move to the VB of photocatalyst A, curbing their recombination due to spatial isolation. However, after the charge transfer, the redox ability of the photogenerated charges becomes weakened since the top of the VB potential of photocatalyst A is less positive than that of photocatalyst B, and the bottom of the CB potential of photocatalyst B is less negative than that of photocatalyst A. Due to this drawback, the heterojunction photocatalytic system (referred to as type-II heterojunction) fails to simultaneously possess high charge-separation efficiency and strong redox ability. Therefore, a Z-scheme photocatalytic process was proposed by carefully studying the natural photosynthesis reaction in plants, which also features the spatial isolation of the photogenerated charges to hinder their recombination. Although the structure of direct Z-scheme photocatalyst is similar to that of a type-II heterojunction photocatalyst, its charge-carrier migration mechanism is different and the pathway resembles the letter "Z". During the photocatalytic reaction, the photogenerated electrons in photocatalyst B with lower reduction ability recombine with the photogenerated holes in photocatalyst A with lower oxidation ability. Therefore, the photogenerated electrons in photocatalyst A with high reduction ability and the photogenerated holes in photocatalyst B with high oxidation ability can perform the redox reactions without any hindrance, and the performance of the resulting Z-scheme photocatalytic system can be optimized. Further, the large number of defects aggregated at the contact interface exhibits properties similar to that of conductors with low electrical resistance owing to the fact that energy levels at the interface become quasi-continuous [235,236].

Since 2D nanostructures can offer an apt platform for establishing surface contact with other species, the idea of constructing a heterojunction by the hybridization of two types of 2D photocatalysts is an appropriate strategy for increasing the interface area. Recently, the combination of g-C_3N_4 with BiOX/$Bi_xO_yX_z$ for the construction of 2D/2D heterojunction photocatalysts has attracted considerable research attention [237–240]. Liu et al. reported the fabrication of a BiOBr/g-C_3N_4 heterojunction through a simple reflux process, and its photocatalytic performance was studied by the degradation of rhodamine B and bisphenol A under visible light irradiation. The enhanced photocatalytic performance of the heterojunction composite was obviously attributed to the efficient charge generation and separation, while the active species involved during the photodegradation of rhodamine B and bisphenol A were found to be in the order $^\bullet$OH > h^+ > $^\bullet O_2^-$. For determining whether the photocatalytic mechanism followed the type-II heterojunction or Z-scheme system, the migration channel of the photogenerated electron-hole pairs was analysed through UV-Vis diffused reflectance spectroscopy and X-ray photoelectron spectroscopy. The results revealed that the values of CB and VB potentials of pristine BiOBr nanoplates were 0.30 eV and 3.07 eV, while those of pristine g-C_3N_4 nanosheets were −1.12 eV and 1.58 eV, respectively. After the hybridization of g-C_3N_4 with BiOBr, the VB edge of the BiOBr/g-C_3N_4 heterojunction was found to be shifted to 1.32 eV due to the alignment of the Fermi levels at the interface. Under visible light irradiation, the photogenerated electrons moved from the CB of g-C_3N_4 to that of BiOBr, while the photogenerated holes moved from the VB of BiOBr to that of g-C_3N_4 across the intimate well-aligned band structure due to the potential difference. As observed from Figure 12a, if BiOBr/g-C_3N_4 had formed a type-II heterojunction, the formation of $^\bullet O_2^-$ and $^\bullet$OH would not have been possible due to the insufficient reduction and oxidation potential of BiOBr and g-C_3N_4. Therefore, the Z-scheme photocatalytic system was found to be constructed as shown in Figure 12b, wherein the electrons accumulated in the CB of g-C_3N_4 (−1.12 eV vs. NHE) reacted with oxygen molecules to form $^\bullet O_2^-$, and the holes in the VB of BiOBr (3.07 eV vs. NHE) reacted with OH^- to generate $^\bullet$OH radicals [123].

A direct solid-state Z-scheme heterojunction photocatalyst was constructed by coupling nanosheets of BiOI and g-C_3N_4 for the photodegradation of toxic microcystin-LR under visible light irradiation. The rate constant of the best performing g-C_3N_4/BiOI heterojunction photocatalyst (0.4357 h^{-1}) was three and five times greater than pristine BiOI and g-C_3N_4, respectively, and radical scavenger studies revealed that $^\bullet O_2^-$ played the major role in the degradation of microcystin-LR. If BiOI/g-C_3N_4 had formed a type-II heterojunction, the formation of $^\bullet$OH and $^\bullet O_2^-$ would not have been possible due to the insufficient reduction and oxidation potential of BiOI and g-C_3N_4. Therefore, the direct Z-scheme charge transfer mechanism occurred, wherein the photogenerated charges formed in the CB of g-C_3N_4 and the VB of BiOI with high reduction and oxidation ability reacted with O_2 and OH^- to generate $^{\bullet}O_2^-$ and $^{\bullet}OH$, respectively, while the photogenerated charges with low reduction and oxidation ability recombined at the interface [111]. Tian et al. reported the fabrication of two p-n junction photocatalysts by coupling different facets of BiOI with g-C_3N_4 through a simple precipitation method, and studied their feasibility for the photodegradation of various organic contaminants such as 2,4-dichlorophenol, bisphenol A, rhodamine B and tetracycline hydrochloride [112]. Typically, the {001} facet of BiOI was coupled with the {002} facet of g-C_3N_4 to form a (001)-BiOI/(002)-g-C_3N_4 photocatalyst through parallel assembly, and (110)-BiOI/$(002)^+$-g-C_3N_4 was fabricated by the vertical assembly of the {110} facet of BiOI on the positively charged {002} facet of g-C_3N_4. The results indicated that the top-top facets coupled (001)-BiOI/(002)-g-C_3N_4 photocatalyst exhibited more than four times enhanced performance in the photodegradation of bisphenol A and tetracycline hydrochloride in comparison to the laterally assembled (110)-BiOI-$(002)^+$-g-C_3N_4.

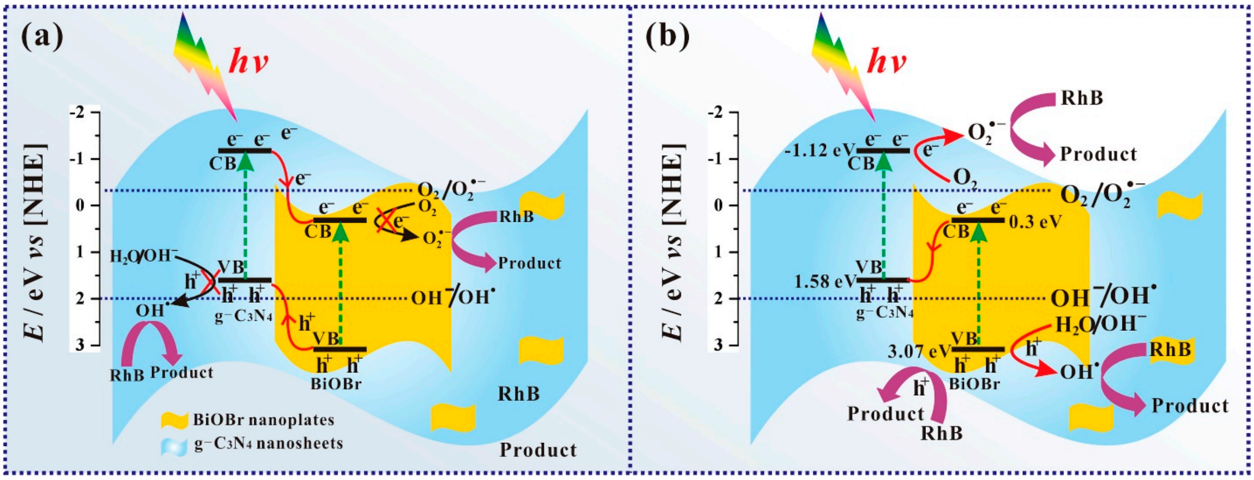

Figure 12. Schematic depicting (**a**) type-II heterojunction and (**b**) Z-scheme system, the two possible photocatalytic charge transfer processes in the heterojunction between BiOBr nanoplates and g-C_3N_4 nanosheets under visible light irradiation. Reprinted from Ref. [123] with permission from Elsevier.

As shown in Figure 13a, the fermi energy level of BiOI as a p-type semiconductor is located close to the VB, while in the case of g-C_3N_4, it is located close to the CB and the energy levels of both the semiconductors achieve an equilibrium to form a (001)-BiOI/(002)-g-C_3N_4 p-n heterojunction photocatalyst. The formation of the p-n junction effectively separates the photogenerated electron-hole pairs in both the heterojunction photocatalysts, but the transfer rate of the photogenerated electrons was found to be distinctly different in the two heterojunctions. In the case of the (001)-BiOI/(002)-g-C_3N_4 p-n heterojunction photocatalyst shown in Figure 13b, the IEF of BiOI along the [1] direction lying perpendicular to the g-C_3N_4 nanosheets results in the rapid enrichment of the electrons on g-C_3N_4 that benefitted the subsequent reduction reactions for the generation of $^1O_2$ and $^{\bullet}O_2^-$ radical species. On the other hand, in the case of the (110)-BiOI/$(002)^+$-g-C_3N_4 p-n heterojunction photocatalyst shown in Figure 13c, the charge transfer direction was parallel, and due to the long diffusion distance, some of the electrons recombined with the holes, leading to inefficient charge transfer in the heterojunction.

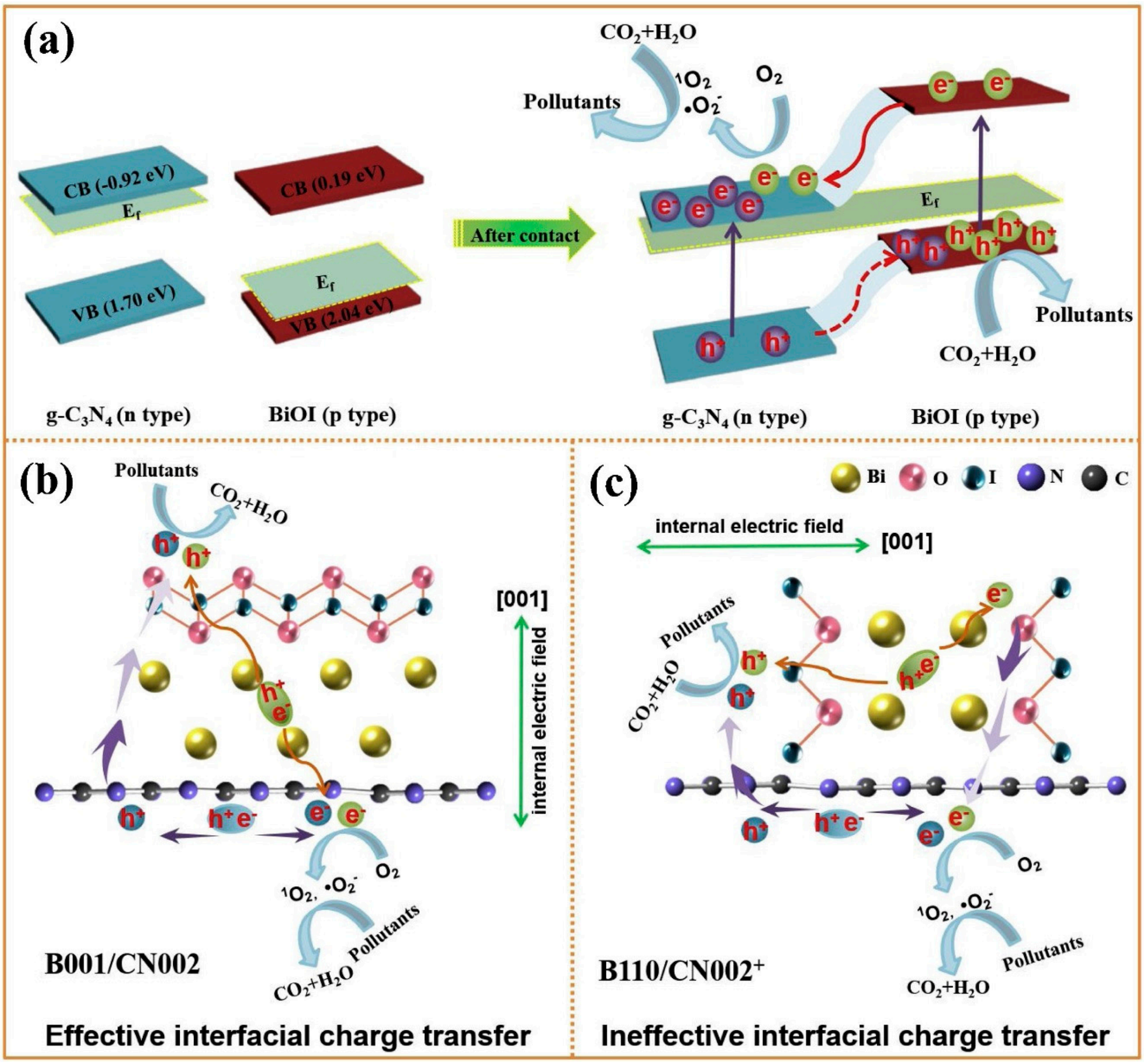

Figure 13. (**a**) Schematic depicting the formation of p-n junction and the proposed charge separation process in a heterojunction formed by coupling the top-top facets of BiOI and g-C_3N_4, i.e., (001)-BiOI/(002)-g-C_3N_4 under visible light irradiation. Schematic depicting the proposed photodegradation mechanism over (**b**) (001)-BiOI/(002)-g-C_3N_4 and (**c**) (110)-BiOI/$(002)^+$-g-C_3N_4 (positively charged g-C_3N_4). Reprinted from Ref. [112] with permission from Elsevier.

The development of ternary or multicomponent heterojunction systems was considered owing to the possibility of enhancing the charge separation and transfer ability and extending the scope of light absorption as compared to binary systems. For instance, the AgBr@g-C_3N_4/BiOBr ternary composite was fabricated through hydrothermal processing and an in situ ion-exchange route for dispersing AgBr nanoparticles between the g-C_3N_4/BiOBr (2D/2D) heterojunction. Interestingly, BiOBr played a central role between g-C_3N_4 and AgBr for providing a high-speed charge transfer channel and isolating the photogenerated charge carriers, resulting in high photocatalytic efficiency for the degradation of rhodamine B (10 ppm, 94% in 30 min) and tetracycline hydrochloride (10 ppm, 78% in 2 h) [160]. The ternary heterojunction between $Bi_{24}O_{31}Cl_{10}$, MoS_2 and g-C_3N_4 was synthesized through the impregnation-calcination method. The higher photocatalytic efficiency of the g-C_3N_4/MoS_2/$Bi_{24}O_{31}Cl_{10}$ ternary heterojunction photocatalyst in the degradation of tetracycline hydrochloride (20 ppm, ~97% in 50 min) under visible light was attributed to its enhanced light absorption capacity, the rapid separation of the photogenerated charges and the strong redox ability. The mechanism of charge transfer was reported to follow a dual Z-scheme pathway as depicted in Figure 14, wherein the photogenerated e^- with less reduction ability from the CB of g-C_3N_4 and MoS_2 jump to the VB of $Bi_{24}O_{31}Cl_{10}$ for recombining with the holes, while the e$^-$ with strong reduction ability and h$^+$ with strong oxidation stability are spared. Scavenger studies and electron spin resonance spectroscopy confirmed the involvement of $^{\bullet}O_2^-$ and $^{\bullet}OH$ radical species, which also confirms the transfer of the photogenerated charge carriers through the dual Z-scheme pathway for ensuring enhanced photocatalytic efficiency [155].

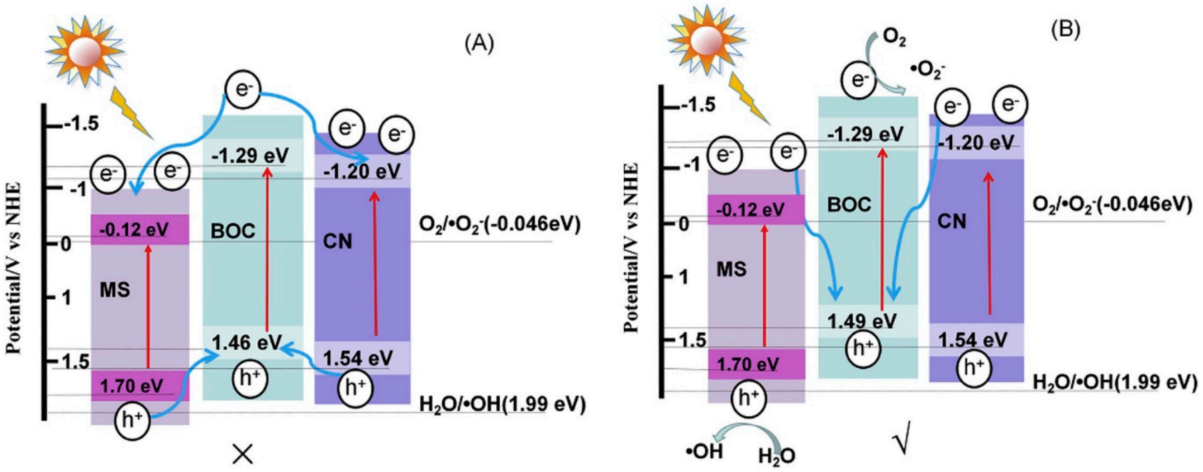

Figure 14. Schematic representation of the possible steps involved during the photocatalytic process and the charge transfer mechanism in the g-C_3N_4/MoS_2/$Bi_{24}O_{31}Cl_{10}$ composite: (**A**) traditional pathway and (**B**) dual Z-scheme pathway. Reprinted from Ref. [155] with permission from Elsevier.

Recent reports on nanostructured heterojunctions of g-C_3N_4/BiOI show their poor dispersion in water, and they easily aggregate because of their higher surface energy. This leads to a remarkable reduction in their photocatalytic activity. In contrast, 1D nanofibres with a high surface area and high aspect ratios have potential in overcoming these problems. In particular, the 3D macroscopic structure of electrospun polyacrylonitrile nanofibres with excellent hydrophobicity can minimize agglomeration and improve the separation of the nanostructured heterojunctions of g-C_3N_4/BiOI in water for practical applications [150]. The fabrication of sandwich-like BiOI/AgI/g-C_3N_4 through the in situ crystallization approach showed good photocatalytic performance in degrading MO and the reduction of Cr(VI) ions under visible light irradiation. The AgI in the composite served as a charge transmission bridge between BiOI and g-C_3N_4 that resulted in more efficient charge transfer and better separation of charge carriers [152]. Jiang et al. developed a novel ternary BiOI/g-C_3N_4/CeO_2 photocatalyst through calcination and hydrothermal treatment. This composite exhibited superior photocatalytic performance, which was far higher than that of either the single component or two component systems. For this photocatalytic BiOI/g-C_3N_4/CeO_2 heterojunction system, 91.6% of tetracycline was degraded in 120 min, owing to the double charge transfer process between the g-C_3N_4 and the other catalysts in the ternary heterojunction and the enhanced separation efficiency of photogenerated electron-hole pairs [153].

5.6. Coupling BiOX and BiOY with g-C_3N_4

The approach of coupling two semiconductors to form a layered structure with an interfacial electric field is particularly promising since this enhances the possibility of satisfying the band alignment requirements for water splitting through the band structure, and subsequently boosts the separation between the photogenerated electron-hole pairs. In this context, heterolayers of $BiOX_1$/$BiOX_2$ (with X_1 and X_2 being different halides) are plausibly superior in comparison to homogeneous BiOX bilayers owing to the possibility of heterojunction induced separation of photogenerated electron-hole pairs [241]. For instance, a ternary heterojunction between BiOI, BiOCl and g-C_3N_4 with different weight ratios was fabricated through the precipitation technique, among which BiOI(50)-BiOCl(30)/g-

C_3N_4(20) exhibited enhanced photodegradation of acid orange 7 (10 ppm, 97% in 140 min) under visible light irradiation in comparison to pristine and other binary/ternary heterojunction counterparts. Under visible light exposure, the photogenerated e^- in the CB of g-C_3N_4 with low reduction ability were transferred to the CB of BiOCl and BiOI, while the h^+ with low oxidation ability were transferred from the VB of BiOI to the VB of g-C_3N_4, resulting in efficient charge separation and enabling the e^- and h^+ with higher reduction and oxidation capabilities to participate in the photodegradation of acid orange 7 [91]. Similarly, a ternary composite of g-C_3N_4/BiOI/BiOBr synthesized through the hydrothermal approach exhibited enhanced performance in the photodegradation of methylene blue (20 ppm, 80% in 150 min) under visible light irradiation. Matching band positions of g-C_3N_4, BiOI and BiOBr allowed the transfer of charge carriers through a direct Z-scheme that favoured the efficient separation and transfer of the photogenerated charge carriers for the effective generation of reactive oxygen species [167]. The deposition-precipitation process was reported for synthesizing 2D g-C_3N_4@BiOCl/$Bi_{12}O_{17}Cl_2$ composites that were employed in the removal of nitric oxide with fixed concentration mixed with air stream under ambient temperature in a continuous flow reactor. The nitric oxide removal efficiency using the g-C_3N_4@BiOCl/$Bi_{12}O_{17}Cl_2$ heterojunction photocatalyst (46.8% in 30 min) was found to be greater than pristine BiOCl/$Bi_{12}O_{17}Cl_2$ (36.2%) and g-C_3N_4 (14.6%) under visible light irradiation, and was attributed to the intimate contact interface, suitable band structure, larger pore volume and improved visible light absorption [165]. Chou et al. reported the fabrication of various types of BiO_xI_y/g-C_3N_4 heterojunction composites through the hydrothermal method towards the photodegradation of crystal violet. Interestingly, $Bi_7O_9I_3$/Bi_5O_7I/g-C_3N_4 was found to exhibit superior performance in comparison to BiOI/g-C_3N_4, $Bi_7O_9I_3$/g-C_3N_4 and Bi_5O_7I/g-C_3N_4 under visible light irradiation, which was ascribed primarily to the formation of a synergistic ternary heterojunction that ensured the separation of photogenerated charge carriers [163].

6. Conclusions and Future Perspectives

Recent years have witnessed significant progress in visible light driven photocatalysis aided by the comprehensive understanding of the structure-to-property relationship of nanostructured materials. Progress on molecularly thin 2D nanosheets has been phenomenal since the discovery of graphene, and studies in the past decade explored their customizable ultrathin architecture, composition and functionality driven by the exceptional physical, chemical, optical and electronic properties arising due to the unique ability of the nanosheets to confine electrons. Advancement towards 2D/2D heterojunction photocatalysts originated as a solution for tackling the rapid recombination of the photogenerated charge carriers in single component systems. However, many interesting studies pertaining to various 2D nanostructured photocatalysts are being pursued, and herein we have presented a comprehensive overview on the recent advances in the design, preparation, and photocatalytic applications of BiOX/$Bi_xO_yX_z$-g-C_3N_4 heterojunction photocatalysts. The band structure of the individual components, the resulting properties and plausible outcomes during heterojunction formation were summarized. Then, various methods for fabricating BiOX/$Bi_xO_yX_z$-g-C_3N_4 heterojunction photocatalysts were thoroughly discussed, emphasizing the dimensional anisotropy and morphological evolution that led to enhanced performance. Applications of the BiOX/$Bi_xO_yX_z$-g-C_3N_4 photocatalysts in the degradation of various organic contaminants, H_2 generation, CO_2 reduction, N_2 fixation and organic synthesis were summarized. Further, the improvement in the performance of BiOX/$Bi_xO_yX_z$-g-C_3N_4 due to defects, facets and by the integration of metals, semiconductors and carbon materials is emphasized. The formation of the type-II heterojunction and Z-scheme bridge complimented with their structural stability is specified at relevant sections, and several salient studies are featured to stimulate the desire of the researchers to find a breakthrough.

Several studies were reported on the usage of BiOX/$Bi_xO_yX_z$-g-C_3N_4 heterojunction photocatalysts for organic contaminant degradation, and some reports were available on the photocatalytic reduction of CO_2 as summarized in Tables 1 and 2. Despite the encouraging results on photocatalytic H_2 generation, O_2 evolution and N_2 fixation using $Bi_xO_yX_z$ and g-C_3N_4, it was surprising that no studies were reported to date on BiOX/$Bi_xO_yX_z$-g-C_3N_4 heterojunction photocatalysts. Therefore, plenty of opportunity exists for designing efficient heterojunction photocatalysts by strategically coupling engineered $Bi_xO_yX_z$ and g-C_3N_4, as detailed below.

(1) Many recent studies reported the synthesis of defect-rich g-C_3N_4 for realizing enhanced activity for H_2 generation [242–245]. The introduction of defects in the form of nitrogen vacancies in g-C_3N_4 induced the formation of midgap states under the CB that resulted in the extension of the visible light absorption, and trapped the photogenerated e^- to minimize recombination loss while facilitating its rapid transfer. Forming a heterojunction by combining defect-rich g-C_3N_4 with defect-rich BiOX/$Bi_xO_yX_z$ can enhance H_2 generation.

(2) The inherent drawback of g-C_3N_4 has been its poor mass diffusion and charge separation efficiency for achieving enhanced photocatalytic O_2 evolution efficiency. Modulating the band structures of g-C_3N_4 (by protonation or the addition of defects and dopants) was reported to enhance its efficiency [246], and therefore a heterojunction photocatalyst constructed between $Bi_xO_yX_z$ with exposed facets and band structure modulated g-C_3N_4 could achieve enhanced quantum efficiencies.

(3) Despite the CB of g-C_3N_4 being more negative than N_2/NH_3 reduction potential, its low conductivity and high recombination rate are some of the impediments that deter its potential for photocatalytic N_2 fixation. The concurrent addition of dopants and defects (carbon/nitrogen vacancies) was reported to improve its photocatalytic N_2 fixation efficiency [247,248]. Heterojunction photocatalysts constructed between doped BiOX/$Bi_xO_yX_z$ with exposed facets and doped/defect-rich g-C_3N_4 are expected to exhibit enhanced photocatalytic N_2 fixation efficiency.

(4) Another interesting opportunity is the construction of a heterojunction between an atomically thin layer of $Bi_xO_yX_z$ and g-C_3N_4, which can be very challenging. However, the unique physical and chemical properties in addition to the easy formation of surface defects could pave the way towards enhanced quantum efficiencies.

Funding: This research received no external funding.

Acknowledgments: This work was supported by the Department of Science and Technology, Government of India through the DST INSPIRE Faculty project (No. IFA15 MS-41) and was funded by the MEXT Promotion of Distinctive Joint Research Center Program Grant Number JPMXP 0618217662. SP acknowledges the European Regional Development Grant for providing Ser Cymru-II Rising Star Fellowship through the Welsh Government (80761-SU-102-West).

Conflicts of Interest: The authors declare no conflict of interest.

References

1. Taylor, D. The Pharmaceutical Industry and the Future of Drug Development. *Issues Environ. Sci. Technol.* **2016**, *2016*, 1–33.
2. Zhang, G.; Wang, J.; Zhang, H.; Zhang, T.; Jiang, S.; Li, B.; Zhang, H.; Cao, J. Facile Synthesize Hierarchical Tubular Micro-Nano Structured AgCl/Ag/TiO2 Hybrid with Favorable Visible Light Photocatalytic Performance. *J. Alloys Compd.* **2021**, *855*, 157512. [CrossRef]
3. Zhang, Q.-Q.; Ying, G.-G.; Pan, C.-G.; Liu, Y.-S.; Zhao, J.-L. Comprehensive Evaluation of Antibiotics Emission and Fate in the River Basins of China: Source Analysis, Multimedia Modeling, and Linkage to Bacterial Resistance. *Environ. Sci. Technol.* **2015**, *49*, 6772–6782. [CrossRef] [PubMed]
4. Bound, J.P.; Voulvoulis, N. Pharmaceuticals in the Aquatic Environment—-A Comparison of Risk Assessment Strategies. *Chemosphere* **2004**, *56*, 1143–1155. [CrossRef] [PubMed]
5. Saxena, R.; Saxena, M.; Lochab, A. Recent Progress in Nanomaterials for Adsorptive Removal of Organic Contaminants from Wastewater. *ChemistrySelect* **2020**, *5*, 335–353. [CrossRef]
6. Kanaujiya, D.K.; Paul, T.; Sinharoy, A.; Pakshirajan, K. Biological Treatment Processes for the Removal of Organic Micropollutants from Wastewater: A Review. *Curr. Pollut. Rep.* **2019**, *5*, 112–128. [CrossRef]
7. Deng, Y.; Zhao, R. Advanced Oxidation Processes (AOPs) in Wastewater Treatment. *Curr. Pollut. Rep.* **2015**, *1*, 167–176. [CrossRef]
8. Fujishima, A.; Honda, K. Electrochemical Photolysis of Water at a Semiconductor Electrode. *Nature* **1972**, *238*, 37–38. [CrossRef]

9. Dong, S.; Feng, J.; Fan, M.; Pi, Y.; Hu, L.; Han, X.; Liu, M.; Sun, J.; Sun, J. Recent Developments in Heterogeneous Photocatalytic Water Treatment Using Visible Light-Responsive Photocatalysts: A Review. *RSC Adv.* **2015**, *5*, 14610–14630. [CrossRef]
10. Chatterjee, D.; Dasgupta, S. Visible Light Induced Photocatalytic Degradation of Organic Pollutants. *J. Photochem. Photobiol. C Photochem. Rev.* **2005**, *6*, 186–205. [CrossRef]
11. Bora, L.V.; Mewada, R.K. Visible/Solar Light Active Photocatalysts for Organic Effluent Treatment: Fundamentals, Mechanisms and Parametric Review. *Renew. Sustain. Energy Rev.* **2017**, *76*, 1393–1421. [CrossRef]
12. Ong, W.-J.; Shak, K.P.Y. 2D/2D Heterostructured Photocatalysts: An Emerging Platform for Artificial Photosynthesis. *Sol. Rrl* **2020**, *4*, 2000132. [CrossRef]
13. Li, X.; Yu, J.; Wageh, S.; Al-Ghamdi, A.A.; Xie, J. Graphene in Photocatalysis: A Review. *Small* **2016**, *12*, 6640–6696. [CrossRef]
14. Di, J.; Xia, J.; Li, H.; Guo, S.; Dai, S. Bismuth Oxyhalide Layered Materials for Energy and Environmental Applications. *Nano Energy* **2017**, *41*, 172–192. [CrossRef]
15. Ye, L.; Su, Y.; Jin, X.; Xie, H.; Zhang, C. Recent Advances in BiOX (X = Cl, Br and I) Photocatalysts: Synthesis, Modification, Facet Effects and Mechanisms. *Environ. Sci. Nano* **2014**, *1*, 90–112. [CrossRef]
16. Li, J.; Yu, Y.; Zhang, L. Bismuth Oxyhalide Nanomaterials: Layered Structures Meet Photocatalysis. *Nanoscale* **2014**, *6*, 8473–8488. [CrossRef]
17. Gondal, M.A.; Xiaofeng, C.; Dastageer, M.A. *Novel Bismuth-Oxyhalide-Based Materials and Their Applications, Advanced Structured Materials*; Springer: New Delhi, India, 2017; Volume 76, ISBN 978-81-322-3737-2.
18. Guo, M.; He, H.; Cao, J.; Lin, H.; Chen, S. Novel I-Doped Bi12O17Cl2 Photocatalysts with Enhanced Photocatalytic Activity for Contaminants Removal. *Mater. Res. Bull.* **2019**, *112*, 205–212. [CrossRef]
19. Ong, W.J.; Tan, L.L.; Ng, Y.H.; Yong, S.T.; Chai, S.P. Graphitic Carbon Nitride (g-C3N4)-Based Photocatalysts for Artificial Photosynthesis and Environmental Remediation: Are We a Step Closer to Achieving Sustainability? *Chem. Rev.* **2016**, *116*, 7159–7329. [CrossRef]
20. Mishra, A.; Mehta, A.; Basu, S.; Shetti, N.P.; Reddy, K.R.; Aminabhavi, T.M. Graphitic Carbon Nitride (g–C3N4)–Based Metal-Free Photocatalysts for Water Splitting: A Review. *Carbon* **2019**, *149*, 693–721. [CrossRef]
21. Yi, J.; El-Alami, W.; Song, Y.; Li, H.; Ajayan, P.M.; Xu, H. Emerging Surface Strategies on Graphitic Carbon Nitride for Solar Driven Water Splitting. *Chem. Eng. J.* **2020**, *382*, 122812. [CrossRef]
22. Liu, J.; Wang, H.; Antonietti, M. Graphitic Carbon Nitride "Reloaded": Emerging Applications beyond (Photo)Catalysis. *Chem. Soc. Rev.* **2016**, *45*, 2308–2326. [CrossRef] [PubMed]
23. Ong, W.J. 2D/2D Graphitic Carbon Nitride (g-C3 N4) Heterojunction Nanocomposites for Photocatalysis: Why Does Face-to-Face Interface Matter? *Front. Mater.* **2017**, *4*, 11. [CrossRef]
24. Yao, W.; Zhang, J.; Wang, Y.; Ren, F. Hybrid Density Functional Study on the Mechanism for the Enhanced Photocatalytic Properties of the Ultrathin Hybrid Layered Nanocomposite G-C3N4/BiOCl. *Appl. Surf. Sci.* **2018**, *435*, 1351–1360. [CrossRef]
25. Zheng, C.Z.; Zhang, C.Y.; Zhang, G.H.; Zhao, D.J.; Wang, Y.Z. Enhanced Photocatalytic Performance of G-C3N4 with BiOCl Quantum Dots Modification. *Mater. Res. Bull.* **2014**, *55*, 212–215. [CrossRef]
26. Shi, S.; Gondal, M.A.; Al-Saadi, A.A.; Fajgar, R.; Kupcik, J.; Chang, X.; Shen, K.; Xu, Q.; Seddigi, Z.S. Facile Preparation of G-C3N4 Modified BiOCl Hybrid Photocatalyst and Vital Role of Frontier Orbital Energy Levels of Model Compounds in Photoactivity Enhancement. *J. Colloid Interface Sci.* **2014**, *416*, 212–219. [CrossRef] [PubMed]
27. Zhang, H.; Zhao, L.; Wang, L.; Hao, J.; Meng, X. Fabrication of Oxygen-Vacancy-Rich Black-BiOBr/BiOBr Heterojunction with Enhanced Photocatalytic Activity. *J. Mater. Sci.* **2020**, *55*, 10785–10795. [CrossRef]
28. Yang, W.; Shan, X.; Chen, Y.; Gao, Y. Enhanced Photocatalytic Performance of C3N4 via Doping with π-Deficient Conjugated Pyridine Ring and BiOCl Composite Heterogeneous Materials. *Diam. Relat. Mater.* **2020**, *108*, 107926. [CrossRef]
29. Song, L.; Zheng, Y.; Chen, C. Sonication-Assisted Deposition–Precipitation Synthesis of Graphitic C3N4/BiOCl Heterostructured Photocatalysts with Enhanced Rhodamine B Photodegradation Activity. *J. Mater. Sci. Mater. Electron.* **2017**, *28*, 15861–15869. [CrossRef]
30. Liu, R.; Chen, Z.; Yao, Y.; Li, Y.; Cheema, W.A.; Wang, D.; Zhu, S. Recent Advancements in G-C3N4-Based Photocatalysts for Photocatalytic CO2reduction: A Mini Review. *RSC Adv.* **2020**, *10*, 29408–29418. [CrossRef]
31. Zhang, X.; Yuan, X.; Jiang, L.; Zhang, J.; Yu, H.; Wang, H.; Zeng, G. Powerful Combination of 2D G-C3N4 and 2D Nanomaterials for Photocatalysis: Recent Advances. *Chem. Eng. J.* **2020**, *390*, 124475. [CrossRef]
32. Lam, S.S.; Nguyen, V.H.; Nguyen Dinh, M.T.; Khieu, D.Q.; La, D.D.; Nguyen, H.T.; Vo, D.V.N.; Xia, C.; Varma, R.S.; Shokouhimehr, M.; et al. Mainstream Avenues for Boosting Graphitic Carbon Nitride Efficiency: Towards Enhanced Solar Light-Driven Photocatalytic Hydrogen Production and Environmental Remediation. *J. Mater. Chem. A* **2020**, *8*, 10571–10603. [CrossRef]
33. Chen, Z.; Zhang, S.; Liu, Y.; Alharbi, N.S.; Rabah, S.O.; Wang, S.; Wang, X. Synthesis and Fabrication of G-C3N4-Based Materials and Their Application in Elimination of Pollutants. *Sci. Total Environ.* **2020**, *731*, 139054. [CrossRef]
34. Fronczak, M. Adsorption Performance of Graphitic Carbon Nitride-Based Materials: Current State of the Art. *J. Environ. Chem. Eng.* **2020**, *8*, 104411. [CrossRef]
35. Stroyuk, O.; Raievska, O.; Zahn, D.R.T. Graphitic Carbon Nitride Nanotubes: A New Material for Emerging Applications. *RSC Adv.* **2020**, *10*, 34059–34087. [CrossRef]
36. Kong, L.; Song, P.; Ma, F.; Sun, M. Graphitic Carbon Nitride-Based 2D Catalysts for Green Energy: Physical Mechanism and Applications. *Mater. Today Energy* **2020**, *17*, 100488. [CrossRef]

37. Starukh, H.; Praus, P. Doping of Graphitic Carbon Nitride with Non-Metal Elements and Its Applications in Photocatalysis. *Catalysts* **2020**, *10*, 1119. [CrossRef]
38. Huang, X.; Gu, W.; Ma, Y.; Liu, D.; Ding, N.; Zhou, L.; Lei, J.; Wang, L.; Zhang, J. Recent Advances of Doped Graphite Carbon Nitride for Photocatalytic Reduction of CO2: A Review. *Res. Chem. Intermed.* **2020**, *46*, 5133–5164. [CrossRef]
39. Ismael, M. A Review on Graphitic Carbon Nitride (g-C3N4) Based Nanocomposites: Synthesis, Categories, and Their Application in Photocatalysis. *J. Alloys Compd.* **2020**, *846*, 156446. [CrossRef]
40. Zhang, W.; Mohamed, A.R.; Ong, W. Z-Scheme Photocatalytic Systems for Carbon Dioxide Reduction: Where Are We Now? *Angew. Chem. Int. Ed.* **2020**, anie.201914925. [CrossRef]
41. Li, Y.; Zhou, M.; Cheng, B.; Shao, Y. Recent Advances in G-C3N4-Based Heterojunction Photocatalysts. *J. Mater. Sci. Technol.* **2020**, *56*, 1–17. [CrossRef]
42. Li, Y.; Li, X.; Zhang, H.; Fan, J.; Xiang, Q. Design and Application of Active Sites in G-C3N4-Based Photocatalysts. *J. Mater. Sci. Technol.* **2020**, *56*, 69–88. [CrossRef]
43. Jourshabani, M.; Lee, B.K.; Shariatinia, Z. From Traditional Strategies to Z-Scheme Configuration in Graphitic Carbon Nitride Photocatalysts: Recent Progress and Future Challenges. *Appl. Catal. B Environ.* **2020**, *276*, 119157. [CrossRef]
44. Singh, S.; Sharma, R.; Khanuja, M. A Review and Recent Developments on Strategies to Improve the Photocatalytic Elimination of Organic Dye Pollutants by BiOX (X = Cl, Br, I, F) Nanostructures. *Korean J. Chem. Eng.* **2018**, *35*, 1955–1968. [CrossRef]
45. Bismuth Oxyhalide Compounds as Photocatalysts–≪Progress in Chemistry≫. September 2009. Available online: https://en.cnki.com.cn/Article_en/CJFDTotal-HXJZ200909004.htm (accessed on 21 November 2020).
46. Liu, J.Q.; Wu, Y.C. Recent Advances in the High Performance BiOX (X = Cl, Br, I) Based Photo-Catalysts. *Wuji Cailiao Xuebao/J. Inorg. Mater.* **2015**, *30*, 1009–1017.
47. Cheng, H.; Huang, B.; Dai, Y. Engineering BiOX (X = Cl, Br, I) Nanostructures for Highly Efficient Photocatalytic Applications. *Nanoscale* **2014**, *6*, 2009–2026. [CrossRef]
48. Zhao, Z.; Sun, Y.; Dong, F. Graphitic Carbon Nitride Based Nanocomposites: A Review. *Nanoscale* **2015**, *7*, 15–37. [CrossRef]
49. Meng, X.; Zhang, Z. Bismuth-Based Photocatalytic Semiconductors: Introduction, Challenges and Possible Approaches. *J. Mol. Catal. A Chem.* **2016**, *423*, 533–549. [CrossRef]
50. Chen, Y.; Jia, G.; Hu, Y.; Fan, G.; Tsang, Y.H.; Li, Z.; Zou, Z. Two-Dimensional Nanomaterials for Photocatalytic CO2 Reduction to Solar Fuels. *Sustain. Energy Fuels* **2017**, *1*, 1875–1898. [CrossRef]
51. Yang, Y.; Zhang, C.; Lai, C.; Zeng, G.; Huang, D.; Cheng, M.; Wang, J.; Chen, F.; Zhou, C.; Xiong, W. BiOX (X = Cl, Br, I) Photocatalytic Nanomaterials: Applications for Fuels and Environmental Management. *Adv. Colloid Interface Sci.* **2018**, *254*, 76–93. [CrossRef]
52. Arthur, R.; Ahern, J.; Patterson, H. Application of BiOX Photocatalysts in Remediation of Persistent Organic Pollutants. *Catalysts* **2018**, *8*, 604. [CrossRef]
53. Garg, S.; Yadav, M.; Chandra, A.; Hernadi, K. A Review on BiOX (X = Cl, Br and I) Nano-/Microstructures for Their Photocatalytic Applications. *J. Nanosci. Nanotechnol.* **2018**, *19*, 280–294. [CrossRef] [PubMed]
54. Ye, L.; Deng, Y.; Wang, L.; Xie, H.; Su, F. Bismuth-Based Photocatalysts for Solar Photocatalytic Carbon Dioxide Conversion. *ChemSusChem* **2019**, *12*, 3671–3701. [CrossRef] [PubMed]
55. Wang, Z.; Chen, M.; Huang, D.; Zeng, G.; Xu, P.; Zhou, C.; Lai, C.; Wang, H.; Cheng, M.; Wang, W. Multiply Structural Optimized Strategies for Bismuth Oxyhalide Photocatalysis and Their Environmental Application. *Chem. Eng. J.* **2019**, *374*, 1025–1045. [CrossRef]
56. Sharma, K.; Dutta, V.; Sharma, S.; Raizada, P.; Hosseini-Bandegharaei, A.; Thakur, P.; Singh, P. Recent Advances in Enhanced Photocatalytic Activity of Bismuth Oxyhalides for Efficient Photocatalysis of Organic Pollutants in Water: A Review. *J. Ind. Eng. Chem.* **2019**, *78*, 1–20. [CrossRef]
57. Zhao, Y.; Zhang, S.; Shi, R.; Waterhouse, G.I.N.; Tang, J.; Zhang, T. Two-Dimensional Photocatalyst Design: A Critical Review of Recent Experimental and Computational Advances. *Mater. Today* **2020**, *34*, 78–91. [CrossRef]
58. Xiong, J.; Song, P.; Di, J.; Li, H. Bismuth-Rich Bismuth Oxyhalides: A New Opportunity to Trigger High-Efficiency Photocatalysis. *J. Mater. Chem. A* **2020**, *8*, 21434–21454. [CrossRef]
59. Ren, K.; Liu, J.; Liang, J.; Zhang, K.; Zheng, X.; Luo, H.; Huang, Y.; Liu, P.; Yu, X. Synthesis of the Bismuth Oxyhalide Solid Solutions with Tunable Band Gap and Photocatalytic Activities. *Dalton Trans.* **2013**, *42*, 9706–9712. [CrossRef]
60. Shi, L.; Si, W.; Wang, F.; Qi, W. Construction of 2D/2D Layered g-C3N4/Bi12O17Cl2 Hybrid Material with Matched Energy Band Structure and Its Improved Photocatalytic Performance. *RSC Adv.* **2018**, *8*, 24500–24508. [CrossRef]
61. Chen, X.; Zhang, J.; Liu, L.; Hu, B.; Zhao, Y.; Zhao, S.; Zhao, W.; Li, S.; Hai, X. Tailored Fabrication of Interface-Rich Hierarchical Bi24O31Br10 with Enhanced Photocatalytic Performance. *Appl. Surf. Sci.* **2019**, *491*, 1–8. [CrossRef]
62. Yang, L.; Liang, L.; Wang, L.; Zhu, J.; Gao, S.; Xia, X. Accelerated Photocatalytic Oxidation of Carbamazepine by a Novel 3D Hierarchical Protonated G-C3N4/BiOBr Heterojunction: Performance and Mechanism. *Appl. Surf. Sci.* **2019**, *473*, 527–539. [CrossRef]
63. Hu, L.; He, H.; Xia, D.; Huang, Y.; Xu, J.; Li, H.; He, C.; Yang, W.; Shu, D.; Wong, P.K. Highly Efficient Performance and Conversion Pathway of Photocatalytic CH3SH Oxidation on Self-Stabilized Indirect Z-Scheme g-C3N4/I3–BiOI. *Acs Appl. Mater. Interfaces* **2018**, *10*, 18693–18708. [CrossRef]

64. Yin, R.; Li, Y.; Zhong, K.; Yao, H.; Zhang, Y.; Lai, K. Multifunctional Property Exploration: Bi4O5I2 with High Visible Light Photocatalytic Performance and a Large Nonlinear Optical Effect. *Rsc Adv.* **2019**, *9*, 4539–4544. [CrossRef]
65. Di, J.; Zhu, C.; Ji, M.; Duan, M.; Long, R.; Yan, C.; Gu, K.; Xiong, J.; She, Y.; Xia, J.; et al. Defect-Rich Bi12O17Cl2 Nanotubes Self-Accelerating Charge Separation for Boosting Photocatalytic CO2 Reduction. *Angew. Chem. Int. Ed.* **2018**, *57*, 14847–14851. [CrossRef]
66. Shang, J.; Hao, W.; Lv, X.; Wang, T.; Wang, X.; Du, Y.; Dou, S.; Xie, T.; Wang, D.; Wang, J. Bismuth Oxybromide with Reasonable Photocatalytic Reduction Activity under Visible Light. *Acs Catal.* **2014**, *4*, 954–961. [CrossRef]
67. Bai, Y.; Chen, T.; Wang, P.; Wang, L.; Ye, L. Bismuth-Rich Bi4O5X2 (X = Br, and I) Nanosheets with Dominant {1 0 1} Facets Exposure for Photocatalytic H2 Evolution. *Chem. Eng. J.* **2016**, *304*, 454–460. [CrossRef]
68. Mi, Y.; Li, H.; Zhang, Y.; Hou, W. Synthesis of Belt-like Bismuth-Rich Bismuth Oxybromide Hierarchical Nanostructures with High Photocatalytic Activities. *J. Colloid Interface Sci.* **2019**, *534*, 301–311. [CrossRef]
69. Wang, X.; Maeda, K.; Thomas, A.; Takanabe, K.; Xin, G.; Carlsson, J.M.; Domen, K.; Antonietti, M. A Metal-Free Polymeric Photocatalyst for Hydrogen Production from Water under Visible Light. *Nat. Mater.* **2009**, *8*, 76–80. [CrossRef] [PubMed]
70. Teixeira, I.F.; Barbosa, E.C.M.; Tsang, S.C.E.; Camargo, P.H.C. Carbon Nitrides and Metal Nanoparticles: From Controlled Synthesis to Design Principles for Improved Photocatalysis. *Chem. Soc. Rev.* **2018**, *47*, 7783–7817. [CrossRef]
71. Wen, J.; Xie, J.; Chen, X.; Li, X. A Review on G-C3 N4 -Based Photocatalysts. *Appl. Surf. Sci.* **2017**, *391*, 72–123. [CrossRef]
72. Yan, S.C.; Lv, S.B.; Li, Z.S.; Zou, Z.G. Organic-Inorganic Composite Photocatalyst of g-C3N4 and TaON with Improved Visible Light Photocatalytic Activities. *Dalton Trans.* **2010**, *39*, 1488–1491. [CrossRef] [PubMed]
73. Sudhaik, A.; Raizada, P.; Shandilya, P.; Jeong, D.-Y.; Lim, J.-H.; Singh, P. Review on Fabrication of Graphitic Carbon Nitride Based Efficient Nanocomposites for Photodegradation of Aqueous Phase Organic Pollutants. *J. Ind. Eng. Chem.* **2018**, *67*, 28–51. [CrossRef]
74. Dong, G.; Zhang, Y.; Pan, Q.; Qiu, J. A Fantastic Graphitic Carbon Nitride (g-C3N4) Material: Electronic Structure, Photocatalytic and Photoelectronic Properties. *J. Photochem. Photobiol. C Photochem. Rev.* **2014**, *20*, 33–50. [CrossRef]
75. You, Z.; Wu, C.; Shen, Q.; Yu, Y.; Chen, H.; Su, Y.; Wang, H.; Wu, C.; Zhang, F.; Yang, H. A Novel Efficient G-C3N4@BiOI p–n Heterojunction Photocatalyst Constructed through the Assembly of g-C3N4 Nanoparticles. *Dalton Trans.* **2018**, *47*, 7353–7361. [CrossRef]
76. Rabenau, A. The Role of Hydrothermal Synthesis in Preparative Chemistry. *Angew. Chem. Int. Ed. Engl.* **1985**, *24*, 1026–1040. [CrossRef]
77. Yang, Y.; Matsubara, S.; Xiong, L.; Hayakawa, T.; Nogami, M. Solvothermal Synthesis of Multiple Shapes of Silver Nanoparticles and Their SERS Properties. *J. Phys. Chem. C* **2007**, *111*, 9095–9104. [CrossRef]
78. Xiao, X.; Liu, C.; Hu, R.; Zuo, X.; Nan, J.; Li, L.; Wang, L. Oxygen-Rich Bismuth Oxyhalides: Generalized One-Pot Synthesis, Band Structures and Visible-Light Photocatalytic Properties. *J. Mater. Chem.* **2012**, *22*, 22840–22843. [CrossRef]
79. Huo, Y.; Zhang, J.; Miao, M.; Jin, Y. Solvothermal Synthesis of Flower-like BiOBr Microspheres with Highly Visible-Light Photocatalytic Performances. *Appl. Catal. B Environ.* **2012**, *111–112*, 334–341. [CrossRef]
80. Shi, X.; Chen, X.; Chen, X.; Zhou, S.; Lou, S.; Wang, Y.; Yuan, L. PVP Assisted Hydrothermal Synthesis of BiOBr Hierarchical Nanostructures and High Photocatalytic Capacity. *Chem. Eng. J.* **2013**, *222*, 120–127. [CrossRef]
81. Li, H.; Ma, A.; Zhang, D.; Gao, Y.; Dong, Y. Rational Design Direct Z-Scheme BiOBr/g-C3N4 Heterojunction with Enhanced Visible Photocatalytic Activity for Organic Pollutants Elimination. *Rsc Adv.* **2020**, *10*, 4681–4689. [CrossRef]
82. Li, X.; Yu, J.; Jaroniec, M. Hierarchical Photocatalysts. *Chem. Soc. Rev.* **2016**, *45*, 2603–2636. [CrossRef]
83. Wang, S.; Hai, X.; Ding, X.; Chang, K.; Xiang, Y.; Meng, X.; Yang, Z.; Chen, H.; Ye, J. Light-Switchable Oxygen Vacancies in Ultrafine Bi5O7Br Nanotubes for Boosting Solar-Driven Nitrogen Fixation in Pure Water. *Adv. Mater.* **2017**, *29*. [CrossRef]
84. Liu, H.; Zhou, H.; Liu, X.; Li, H.; Ren, C.; Li, X.; Li, W.; Lian, Z.; Zhang, M. Engineering Design of Hierarchical G-C3N4@Bi/BiOBr Ternary Heterojunction with Z-Scheme System for Efficient Visible-Light Photocatalytic Performance. *J. Alloys Compd.* **2019**, *798*, 741–749. [CrossRef]
85. Ji, M.; Di, J.; Ge, Y.; Xia, J.; Li, H. 2D-2D Stacking of Graphene-like g-C3N4/Ultrathin Bi4O5Br2 with Matched Energy Band Structure towards Antibiotic Removal. *Appl. Surf. Sci.* **2017**, *413*, 372–380. [CrossRef]
86. Wang, X.J.; Wang, Q.; Li, F.T.; Yang, W.Y.; Zhao, Y.; Hao, Y.J.; Liu, S.J. Novel BiOCl-C3N4 Heterojunction Photocatalysts: In Situ Preparation via an Ionic-Liquid-Assisted Solvent-Thermal Route and Their Visible-Light Photocatalytic Activities. *Chem. Eng. J.* **2013**, *234*, 361–371. [CrossRef]
87. Xia, J.; Ji, M.; Di, J.; Wang, B.; Yin, S.; Zhang, Q.; He, M.; Li, H. Construction of Ultrathin C3N4/Bi4O5I2 Layered Nanojunctions via Ionic Liquid with Enhanced Photocatalytic Performance and Mechanism Insight. *Appl. Catal. B Environ.* **2016**, *191*, 235–245. [CrossRef]
88. Di, J.; Xia, J.; Yin, S.; Xu, H.; He, M.; Li, H.; Xu, L.; Jiang, Y. A G-C3N4/BiOBr Visible-Light-Driven Composite: Synthesis via a Reactable Ionic Liquid and Improved Photocatalytic Activity. *RSC Adv.* **2013**, *3*, 19624–19631. [CrossRef]
89. Yin, S.; Di, J.; Li, M.; Sun, Y.; Xia, J.; Xu, H.; Fan, W.; Li, H. Ionic Liquid-Assisted Synthesis and Improved Photocatalytic Activity of p-n Junction g-C3N4/BiOCl. *J. Mater. Sci.* **2016**, *51*, 4769–4777. [CrossRef]
90. Ren, X.; Gao, M.; Zhang, Y.; Zhang, Z.; Cao, X.; Wang, B.; Wang, X. Photocatalytic Reduction of CO2 on BiOX: Effect of Halogen Element Type and Surface Oxygen Vacancy Mediated Mechanism. *Appl. Catal. B Environ.* **2020**, *274*, 119063. [CrossRef]

91. Aghdam, S.M.; Haghighi, M.; Allahyari, S.; Yosefi, L. Precipitation Dispersion of Various Ratios of BiOI/BiOCl Nanocomposite over g-C3N4 for Promoted Visible Light Nanophotocatalyst Used in Removal of Acid Orange 7 from Water. *J. Photochem. Photobiol. A Chem.* **2017**, *338*, 201–212. [CrossRef]
92. Mousavi, M.; Habibi-Yangjeh, A. Magnetically Separable Ternary G-C3N4/Fe3O4/BiOI Nanocomposites: Novel Visible-Light-Driven Photocatalysts Based on Graphitic Carbon Nitride. *J. Colloid Interface Sci.* **2016**, *465*, 83–92. [CrossRef]
93. Asadzadeh-Khaneghah, S.; Habibi-Yangjeh, A.; Yubuta, K. Novel G-C3N4 Nanosheets/CDs/BiOCl Photocatalysts with Exceptional Activity under Visible Light. *J. Am. Ceram. Soc.* **2019**, *102*, 1435–1453. [CrossRef]
94. Asadzadeh-Khaneghah, S.; Habibi-Yangjeh, A.; Nakata, K. Graphitic Carbon Nitride Nanosheets Anchored with BiOBr and Carbon Dots: Exceptional Visible-Light-Driven Photocatalytic Performances for Oxidation and Reduction Reactions. *J. Colloid Interface Sci.* **2018**, *530*, 642–657. [CrossRef]
95. Di, J.; Xia, J.; Chisholm, M.F.; Zhong, J.; Chen, C.; Cao, X.; Dong, F.; Chi, Z.; Chen, H.; Weng, Y.; et al. Defect-Tailoring Mediated Electron–Hole Separation in Single-Unit-Cell Bi_3O_4 Br Nanosheets for Boosting Photocatalytic Hydrogen Evolution and Nitrogen Fixation. *Adv. Mater.* **2019**, *31*, 1807576. [CrossRef]
96. Che, H.; Che, G.; Dong, H.; Hu, W.; Hu, H.; Liu, C.; Li, C. Fabrication of Z-Scheme Bi3O4Cl/g-C3N4 2D/2D Heterojunctions with Enhanced Interfacial Charge Separation and Photocatalytic Degradation Various Organic Pollutants Activity. *Appl. Surf. Sci.* **2018**, *455*, 705–716. [CrossRef]
97. Bang, J.H.; Suslick, K.S. Applications of Ultrasound to the Synthesis of Nanostructured Materials. *Adv. Mater.* **2010**, *22*, 1039–1059. [CrossRef]
98. Pereira, C.; Pereira, A.M.; Fernandes, C.; Rocha, M.; Mendes, R.; Fernández-García, M.P.; Guedes, A.; Tavares, P.B.; Grenéche, J.M.; Araújo, J.P.; et al. Superparamagnetic MFe 2O4 (M = Fe, Co, Mn) Nanoparticles: Tuning the Particle Size and Magnetic Properties through a Novel One-Step Coprecipitation Route. *Chem. Mater.* **2012**, *24*, 1496–1504. [CrossRef]
99. Liu, X.; Ni, Z.; He, Y.; Su, N.; Guo, R.; Wang, Q.; Yi, T. Ultrasound-Assisted Two-Step Water-Bath Synthesis of g-C3N4/BiOBr Composites: Visible Light-Driven Photocatalysis, Sterilization, and Reaction Mechanism. *New J. Chem.* **2019**, *43*, 8711–8721. [CrossRef]
100. Pelaez, M.; Nolan, N.T.; Pillai, S.C.; Seery, M.K.; Falaras, P.; Kontos, A.G.; Dunlop, P.S.M.; Hamilton, J.W.J.; Byrne, J.A.; O'Shea, K.; et al. A Review on the Visible Light Active Titanium Dioxide Photocatalysts for Environmental Applications. *Appl. Catal. B Environ.* **2012**, *125*, 331–349. [CrossRef]
101. Banerjee, S.; Pillai, S.C.; Falaras, P.; O'shea, K.E.; Byrne, J.A.; Dionysiou, D.D. New Insights into the Mechanism of Visible Light Photocatalysis. *J. Phys. Chem. Lett.* **2014**, *5*, 2543–2554. [CrossRef] [PubMed]
102. Di, J.; Xia, J.; Ji, M.; Yin, S.; Li, H.; Xu, H.; Zhang, Q.; Li, H. Controllable Synthesis of Bi4O5Br2 Ultrathin Nanosheets for Photocatalytic Removal of Ciprofloxacin and Mechanism Insight. *J. Mater. Chem. A* **2015**, *3*, 15108–15118. [CrossRef]
103. Wang, C.Y.; Zhang, X.; Qiu, H.B.; Huang, G.X.; Yu, H.Q. Bi24O31Br10 Nanosheets with Controllable Thickness for Visible–Light–Driven Catalytic Degradation of Tetracycline Hydrochloride. *Appl. Catal. B Environ.* **2017**, *205*, 615–623. [CrossRef]
104. Ye, L.; Liu, J.; Jiang, Z.; Peng, T.; Zan, L. Facets Coupling of BiOBr-g-C3N4 Composite Photocatalyst for Enhanced Visible-Light-Driven Photocatalytic Activity. *Appl. Catal. B Environ.* **2013**, *142–143*, 1–7. [CrossRef]
105. Di, J.; Xia, J.; Yin, S.; Xu, H.; Xu, L.; Xu, Y.; He, M.; Li, H. Preparation of Sphere-like g-C3N4/BiOI Photocatalysts via a Reactable Ionic Liquid for Visible-Light-Driven Photocatalytic Degradation of Pollutants. *J. Mater. Chem. A* **2014**, *2*, 5340–5351. [CrossRef]
106. Liu, C.; Huang, H.; Du, X.; Zhang, T.; Tian, N.; Guo, Y.; Zhang, Y. In Situ Co-Crystallization for Fabrication of g-C3N4/Bi5O7I Heterojunction for Enhanced Visible-Light Photocatalysis. *J. Phys. Chem. C* **2015**, *119*, 17156–17165. [CrossRef]
107. Geng, X.; Chen, S.; Lv, X.; Jiang, W.; Wang, T. Synthesis of G-C3N4/Bi5O7I Microspheres with Enhanced Photocatalytic Activity under Visible Light. *Appl. Surf. Sci.* **2018**, *462*, 18–28. [CrossRef]
108. Zhou, M.; Wu, J.; Wang, H.; Guan, D.; Dong, X.; Wang, J.; Jia, T.; Liu, Q. Fabrication of Z-Scheme Heterojunction g-C3N4/Yb3+-Bi5O7I Photocatalysts with Enhanced Photocatalytic Performance under Visible Irradiation for Hg0Removal. *Energy Fuels* **2020**, *34*, 16445–16455. [CrossRef]
109. Zhang, Z.; Pan, Z.; Guo, Y.; Wong, P.K.; Zhou, X.; Bai, R. In-Situ Growth of All-Solid Z-Scheme Heterojunction Photocatalyst of Bi7O9I3/g-C3N4 and High Efficient Degradation of Antibiotic under Visible Light. *Appl. Catal. B Environ.* **2020**, *261*, 118212. [CrossRef]
110. Feng, Z.; Zeng, L.; Zhang, Q.; Ge, S.; Zhao, X.; Lin, H.; He, Y. In Situ Preparation of G-C3N4/Bi4O5I2 Complex and Its Elevated Photoactivity in Methyl Orange Degradation under Visible Light. *J. Environ. Sci.* **2020**, *87*, 149–162. [CrossRef] [PubMed]
111. Zhang, F.; Wang, L.; Xiao, M.; Liu, F.; Xu, X.; Du, E. Construction of Direct Solid-State Z-Scheme g-C3N4/BiOI with Improved Photocatalytic Activity for Microcystin-LR Degradation. *J. Mater. Res.* **2018**, *33*, 201–212. [CrossRef]
112. Tian, N.; Huang, H.; Wang, S.; Zhang, T.; Du, X.; Zhang, Y. Facet-Charge-Induced Coupling Dependent Interfacial Photocharge Separation: A Case of BiOI/g-C3N4 p-n Junction. *Appl. Catal. B Environ.* **2020**, *267*, 118697. [CrossRef]
113. He, R.; Cheng, K.; Wei, Z.; Zhang, S.; Xu, D. Room-Temperature in Situ Fabrication and Enhanced Photocatalytic Activity of Direct Z-Scheme BiOI/g-C3N4 Photocatalyst. *Appl. Surf. Sci.* **2019**, *465*, 964–972. [CrossRef]
114. An, H.; Lin, B.; Xue, C.; Yan, X.; Dai, Y.; Wei, J.; Yang, G. Formation of BiOI/g-C3N4 Nanosheet Composites with High Visible-Light-Driven Photocatalytic Activity. *Chin. J. Catal.* **2018**, *39*, 654–663. [CrossRef]
115. Zhang, J.; Fu, J.; Wang, Z.; Cheng, B.; Dai, K.; Ho, W. Direct Z-Scheme Porous g-C3N4/BiOI Heterojunction for Enhanced Visible-Light Photocatalytic Activity. *J. Alloys Compd.* **2018**, *766*, 841–850. [CrossRef]

116. Jiang, J.; Mu, Z.; Zhao, P.; Wang, H.; Lin, Y. Photogenerated Charge Behavior of BiOI/g-C3N4 Photocatalyst in Photoreduction of Cr (VI): A Novel Understanding for High-Performance. *Mater. Chem. Phys.* **2020**, *252*, 123194. [CrossRef]
117. Liu, W.; Qiao, L.; Zhu, A.; Liu, Y.; Pan, J. Constructing 2D BiOCl/C3N4 Layered Composite with Large Contact Surface for Visible-Light-Driven Photocatalytic Degradation. *Appl. Surf. Sci.* **2017**, *426*, 897–905. [CrossRef]
118. Wang, Q.; Wang, W.; Zhong, L.; Liu, D.; Cao, X.; Cui, F. Oxygen Vacancy-Rich 2D/2D BiOCl-g-C3N4 Ultrathin Heterostructure Nanosheets for Enhanced Visible-Light-Driven Photocatalytic Activity in Environmental Remediation. *Appl. Catal. B Environ.* **2018**, *220*, 290–302. [CrossRef]
119. Song, L.; Pang, Y.; Zheng, Y.; Ge, L. Hydrothermal Synthesis of Novel G-C3N4/BiOCl Heterostructure Nanodiscs for Efficient Visible Light Photodegradation of Rhodamine B. *Appl. Phys. A* **2017**, *123*, 500. [CrossRef]
120. Zhang, X.; An, D.; Feng, D.; Liang, F.; Chen, Z.; Liu, W.; Yang, Z.; Xian, M. In Situ Surfactant-Free Synthesis of Ultrathin BiOCl/g-C3N4 Nanosheets for Enhanced Visible-Light Photodegradation of Rhodamine B. *Appl. Surf. Sci.* **2019**, *476*, 706–715. [CrossRef]
121. Hou, W.; Deng, C.; Xu, H.; Li, D.; Zou, Z.; Xia, H.; Xia, D. N–p BiOCl@g-C_3 N_4 Heterostructure with Rich-oxygen Vacancies for Photodegradation of Carbamazepine. *ChemistrySelect* **2020**, *5*, 2767–2777. [CrossRef]
122. Al Marzouqi, F.; Al Farsi, B.; Kuvarega, A.T.; Al Lawati, H.A.J.; Al Kindy, S.M.Z.; Kim, Y.; Selvaraj, R. Controlled Microwave-Assisted Synthesis of the 2D-BiOCl/2D-g-C3 N4 Heterostructure for the Degradation of Amine-Based Pharmaceuticals under Solar Light Illumination. *ACS Omega* **2019**, *4*, 4671–4678. [CrossRef] [PubMed]
123. Liu, C.; Wu, Q.; Ji, M.; Zhu, H.; Hou, H.; Yang, Q.; Jiang, C.; Wang, J.; Tian, L.; Chen, J.; et al. Constructing Z-Scheme Charge Separation in 2D Layered Porous BiOBr/Graphitic C3N4 Nanosheets Nanojunction with Enhanced Photocatalytic Activity. *J. Alloys Compd.* **2017**, *723*, 1121–1131. [CrossRef]
124. Wu, J.; Xie, Y.; Ling, Y.; Dong, Y.; Li, J.; Li, S.; Zhao, J. Synthesis of Flower-Like g-C3N4/BiOBr and Enhancement of the Activity for the Degradation of Bisphenol A Under Visible Light Irradiation. *Front. Chem.* **2019**, *7*, 649. [CrossRef] [PubMed]
125. Jiang, M.; Shi, Y.; Huang, J.; Wang, L.; She, H.; Tong, J.; Su, B.; Wang, Q. Synthesis of Flowerlike G-C3N4/BiOBr with Enhanced Visible Light Photocatalytic Activity for Dye Degradation. *Eur. J. Inorg. Chem.* **2018**, *2018*, 1834–1841. [CrossRef]
126. Zhou, M.; Huang, W.; Zhao, Y.; Jin, Z.; Hua, X.; Li, K.; Tang, L.; Cai, Z. 2D G-C3N4/BiOBr Heterojunctions with Enhanced Visible Light Photocatalytic Activity. *J. Nanoparticle Res.* **2020**, *22*, 13. [CrossRef]
127. Lv, J.; Dai, K.; Zhang, J.; Liu, Q.; Liang, C.; Zhu, G. Facile Constructing Novel 2D Porous G-C3N4/BiOBr Hybrid with Enhanced Visible-Light-Driven Photocatalytic Activity. *Sep. Purif. Technol.* **2017**, *178*, 6–17. [CrossRef]
128. Kanagaraj, T.; Thiripuranthagan, S.; Paskalis, S.M.K.; Abe, H. Visible Light Photocatalytic Activities of Template Free Porous Graphitic Carbon Nitride—BiOBr Composite Catalysts towards the Mineralization of Reactive Dyes. *Appl. Surf. Sci.* **2017**, *426*, 1030–1045. [CrossRef]
129. Chen, B.; Zhou, L.; Tian, Y.; Yu, J.; Lei, J.; Wang, L.; Liu, Y.; Zhang, J. Z-Scheme Inverse Opal CN/BiOBr Photocatalysts for Highly Efficient Degradation of Antibiotics. *Phys. Chem. Chem. Phys.* **2019**, *21*, 12818–12825. [CrossRef]
130. Dong, Z.; Pan, J.; Wang, B.; Jiang, Z.; Zhao, C.; Wang, J.; Song, C.; Zheng, Y.; Cui, C.; Li, C. The P-n-Type Bi5O7I-Modified Porous C3N4 Nano-Heterojunction for Enhanced Visible Light Photocatalysis. *J. Alloys Compd.* **2018**, *747*, 788–795. [CrossRef]
131. Salimi, M.; Esrafili, A.; Sobhi, H.R.; Behbahani, M.; Gholami, M.; Farzadkia, M.; Jafari, A.J.; Kalantary, R.R. Photocatalytic Degradation of Metronidazole Using D-g-C_3N_4-Bi_5O_7I Composites Under Visible Light Irradiation: Degradation Product, and Mechanisms. *ChemistrySelect* **2019**, *4*, 10288–10295. [CrossRef]
132. Tian, N.; Zhang, Y.; Liu, C.; Yu, S.; Li, M.; Huang, H. G-C3N4/Bi4O5I2 2D-2D Heterojunctional Nanosheets with Enhanced Visible-Light Photocatalytic Activity. *RSC Adv.* **2016**, *6*, 10895–10903. [CrossRef]
133. Ma, Y.; Chen, Y.; Feng, Z.; Zeng, L.; Chen, Q.; Jin, R.; Lu, Y.; Huang, Y.; Wu, Y.; He, Y. Preparation, Characterization of Bi3O4Cl/g-C3N4 Composite and Its Photocatalytic Activity in Dye Degradation. *J. Water Process Eng.* **2017**, *18*, 65–72. [CrossRef]
134. Zhao, J.; Ji, M.; Di, J.; Ge, Y.; Zhang, P.; Xia, J.; Li, H. Synthesis of G-C3N4/Bi4O5Br2 via Reactable Ionic Liquid and Its Cooperation Effect for the Enhanced Photocatalytic Behavior towards Ciprofloxacin Degradation. *J. Photochem. Photobiol. A Chem.* **2017**, *347*, 168–176. [CrossRef]
135. Yi, F.; Ma, J.; Lin, C.; Wang, L.; Zhang, H.; Qian, Y.; Zhang, K. Insights into the Enhanced Adsorption/Photocatalysis Mechanism of a Bi4O5Br2/g-C3N4 Nanosheet. *J. Alloys Compd.* **2020**, *821*, 153557. [CrossRef]
136. Jiang, J.; Song, Y.; Wang, X.; Li, T.; Li, M.; Lin, Y.; Xie, T.; Dong, S. Enhancing Aqueous Pollutant Photodegradation via a Fermi Level Matched Z-Scheme BiOI/Pt/g-C3N4 Photocatalyst: Unobstructed Photogenerated Charge Behavior and Degradation Pathway Exploration. *Catal. Sci. Technol.* **2020**, *10*, 3324–3333. [CrossRef]
137. Li, Z.; Jin, C.; Lv, C.; Wang, M.; Kang, J.; Liu, S.; Xie, Y.; Zhu, T. Construction of G-C3N4/Eu(III) Doped Bi24O31Cl10 Heterojunction for the Enhanced Visible-Light Photocatalytic Performance. *Mater. Chem. Phys.* **2019**, *237*, 121829. [CrossRef]
138. Wang, L.; Zhang, H.; Guo, C.; Feng, L.; Li, C.; Wang, W. Facile Constructing Plasmonic Z-Scheme Au NPs/g-C3N4/BiOBr for Enhanced Visible Light Photocatalytic Activity. *J. Fuel Chem. Technol.* **2019**, *47*, 834–842. [CrossRef]
139. Bai, Y.; Chen, T.; Wang, P.; Wang, L.; Ye, L.; Shi, X.; Bai, W. Size-Dependent Role of Gold in g-C3N4/BiOBr/Au System for Photocatalytic CO2 Reduction and Dye Degradation. *Sol. Energy Mater. Sol. Cells* **2016**, *157*, 406–414. [CrossRef]
140. Asadzadeh-Khaneghah, S.; Habibi-Yangjeh, A.; Seifzadeh, D. Graphitic Carbon Nitride Nanosheets Coupled with Carbon Dots and BiOI Nanoparticles: Boosting Visible-Light-Driven Photocatalytic Activity. *J. Taiwan Inst. Chem. Eng.* **2018**, *87*, 98–111. [CrossRef]

141. Wang, Q.; Li, Y.; Huang, L.; Zhang, F.; Wang, H.; Wang, C.; Zhang, Y.; Xie, M.; Li, H. Enhanced Photocatalytic Degradation and Antibacterial Performance by GO/CN/BiOI Composites under LED Light. *Appl. Surf. Sci.* **2019**, *497*, 143753. [CrossRef]
142. You, Z.; Shen, Q.; Su, Y.; Yu, Y.; Wang, H.; Qin, T.; Zhang, F.; Cheng, D.; Yang, H. Construction of a Z-Scheme Core–Shell g-C3N4/MCNTs/BiOI Nanocomposite Semiconductor with Enhanced Visible-Light Photocatalytic Activity. *New J. Chem.* **2017**, *42*, 489–496. [CrossRef]
143. Hu, X.; Hu, J.; Peng, Q.; Ma, X.; Dong, S.; Wang, H. Construction of 2D All-Solid-State Z-Scheme g-C3N4/BiOI/RGO Hybrid Structure Immobilized on Ni Foam for CO2 Reduction and Pollutant Degradation. *Mater. Res. Bull.* **2020**, *122*, 110682. [CrossRef]
144. Bao, Y.; Chen, K. Novel Z-Scheme BiOBr/Reduced Graphene Oxide/Protonated g-C3N4 Photocatalyst: Synthesis, Characterization, Visible Light Photocatalytic Activity and Mechanism. *Appl. Surf. Sci.* **2018**, *437*, 51–61. [CrossRef]
145. Zhang, M.; Lai, C.; Li, B.; Huang, D.; Zeng, G.; Xu, P.; Qin, L.; Liu, S.; Liu, X.; Yi, H.; et al. Rational Design 2D/2D BiOBr/CDs/g-C3N4 Z-Scheme Heterojunction Photocatalyst with Carbon Dots as Solid-State Electron Mediators for Enhanced Visible and NIR Photocatalytic Activity: Kinetics, Intermediates, and Mechanism Insight. *J. Catal.* **2019**, *369*, 469–481. [CrossRef]
146. Yu, X.; Wu, P.; Qi, C.; Shi, J.; Feng, L.; Li, C.; Wang, L. Ternary-Component Reduced Graphene Oxide Aerogel Constructed by g-C3N4/BiOBr Heterojunction and Graphene Oxide with Enhanced Photocatalytic Performance. *J. Alloys Compd.* **2017**, *729*, 162–170. [CrossRef]
147. Shi, Z.; Zhang, Y.; Shen, X.; Duoerkun, G.; Zhu, B.; Zhang, L.; Li, M.; Chen, Z. Fabrication of G-C3N4/BiOBr Heterojunctions on Carbon Fibers as Weaveable Photocatalyst for Degrading Tetracycline Hydrochloride under Visible Light. *Chem. Eng. J.* **2020**, *386*, 124010. [CrossRef]
148. Chen, Y.; Ji, X.; Vadivel, S.; Paul, B. Anchoring Carbon Spheres on BiOBr/g-C3N4 Matrix for High-Performance Visible Light Photocatalysis. *Ceram. Int.* **2018**, *44*, 23320–23323. [CrossRef]
149. Li, J.; Yu, X.; Zhu, Y.; Fu, X.; Zhang, Y. 3D-2D-3D BiOI/Porous g-C3N4/Graphene Hydrogel Composite Photocatalyst with Synergy of Adsorption-Photocatalysis in Static and Flow Systems. *J. Alloys Compd.* **2021**, *850*, 156778. [CrossRef]
150. Zhou, X.; Shao, C.; Yang, S.; Li, X.; Guo, X.; Wang, X.; Li, X.; Liu, Y. Heterojunction of G-C3N4/BiOI Immobilized on Flexible Electrospun Polyacrylonitrile Nanofibers: Facile Preparation and Enhanced Visible Photocatalytic Activity for Floating Photocatalysis. *Acs Sustain. Chem. Eng.* **2018**, *6*, 2316–2323. [CrossRef]
151. Wang, X.; Zhou, X.; Shao, C.; Li, X.; Liu, Y. Graphitic Carbon Nitride/BiOI Loaded on Electrospun Silica Nanofibers with Enhanced Photocatalytic Activity. *Appl. Surf. Sci.* **2018**, *455*, 952–962. [CrossRef]
152. Huang, Y.; Zhang, X.; Zhang, K.; Lu, P.; Zhang, D. Facile Fabrication of Sandwich-like BiOI/AgI/g-C3N4 Composites for Efficient Photocatalytic Degradation of Methyl Orange and Reduction of Cr(VI). *J. Nanoparticle Res.* **2018**, *20*, 328. [CrossRef]
153. Jiang, X.; Lai, S.; Xu, W.; Fang, J.; Chen, X.; Beiyuan, J.; Zhou, X.; Lin, K.; Liu, J.; Guan, G. Novel Ternary BiOI/g-C3N4/CeO2 Catalysts for Enhanced Photocatalytic Degradation of Tetracycline under Visible-Light Radiation via Double Charge Transfer Process. *J. Alloys Compd.* **2019**, *809*, 151804. [CrossRef]
154. Gholizadeh Khasevani, S.; Gholami, M.R. Engineering a Highly Dispersed Core@shell Structure for Efficient Photocatalysis: A Case Study of Ternary Novel BiOI@MIL-88A(Fe)@g-C3N4 Nanocomposite. *Mater. Res. Bull.* **2018**, *106*, 93–102. [CrossRef]
155. Kang, J.; Jin, C.; Li, Z.; Wang, M.; Chen, Z.; Wang, Y. Dual Z-Scheme MoS2/g-C3N4/Bi24O31Cl10 Ternary Heterojunction Photocatalysts for Enhanced Visible-Light Photodegradation of Antibiotic. *J. Alloys Compd.* **2020**, *825*, 153975. [CrossRef]
156. Zhao, W.; Wang, A.; Wang, Y.; Lv, C.; Zhu, W.; Dou, S.; Wang, Q.; Zhong, Q. Accessible Fabrication and Mechanism Insight of Heterostructured BiOCl/Bi2MoO6/g-C3N4 Nanocomposites with Efficient Photosensitized Activity. *J. Alloys Compd.* **2017**, *726*, 164–172. [CrossRef]
157. Bellamkonda, S.; Ranga Rao, G. Nanojunction-Mediated Visible Light Photocatalytic Enhancement in Heterostructured Ternary BiOCl/ CdS/g-C3N4 Nanocomposites. *Catal. Today* **2019**, *321–322*, 18–25. [CrossRef]
158. Dong, X.; Sun, Z.; Zhang, X.; Li, C.; Zheng, S. Construction of BiOCl/g-C3N4/Kaolinite Composite and Its Enhanced Photocatalysis Performance under Visible-Light Irradiation. *J. Taiwan Inst. Chem. Eng.* **2018**, *84*, 203–211. [CrossRef]
159. He, B.; Du, Y.; Feng, Y.; Du, M.; Wang, J.; Qu, J.; Liu, Y.; Jiang, N.; Wang, J.; Sun, X. Fabrication of Novel Ternary Direct Z-Scheme + isotype Heterojunction Photocatalyst g-C3N4/g-C3N4/BiOBr with Enhanced Photocatalytic Performance. *Appl. Surf. Sci.* **2020**, *506*, 145031. [CrossRef]
160. Tang, G.; Zhang, F.; Huo, P.; Zulfiqarc, S.; Xu, J.; Yan, Y.; Tang, H. Constructing Novel Visible-Light-Driven Ternary Photocatalyst of AgBr Nanoparticles Decorated 2D/2D Heterojunction of g-C3N4/BiOBr Nanosheets with Remarkably Enhanced Photocatalytic Activity for Water-Treatment. *Ceram. Int.* **2019**, *45*, 19197–19205. [CrossRef]
161. Liu, N.; Xie, H.; Li, J.; Zhao, Y.; Wang, N. Synthesis and High Visible Light Photocatalytic Activity of Ternary Brookite-g-C3N4-BiOBr Composite. *Nano* **2020**, *15*, 2050045. [CrossRef]
162. Zhong, S.; Zhou, H.; Shen, M.; Yao, Y.; Gao, Q. Rationally Designed a G-C3N4/BiOI/Bi2O2CO3 Composite with Promoted Photocatalytic Activity. *J. Alloys Compd.* **2021**, *853*, 157307. [CrossRef]
163. Chou, S.-Y.; Chen, C.-C.; Dai, Y.-M.; Lin, J.-H.; Lee, W.W. Novel Synthesis of Bismuth Oxyiodide/Graphitic Carbon Nitride Nanocomposites with Enhanced Visible-Light Photocatalytic Activity. *RSC Adv.* **2016**, *6*, 33478–33491. [CrossRef]
164. Liu, B.; Han, X.; Wang, Y.; Fan, X.; Wang, Z.; Zhang, J.; Shi, H. Synthesis of G-C3N4/BiOI/BiOBr Heterostructures for Efficient Visible-Light-Induced Photocatalytic and Antibacterial Activity. *J. Mater. Sci. Mater. Electron.* **2018**, *29*, 14300–14310. [CrossRef]
165. Zhang, W.; Liang, Y. Facile Synthesis of Ternary G-C3N4@BiOCl/Bi12O17Cl2 Composites with Excellent Visible Light Photocatalytic Activity for NO Removal. *Front. Chem.* **2019**, *7*, 231. [CrossRef]

166. Kumar, A.; Kumar, A.; Sharma, G.; Al-Muhtaseb, A.H.; Naushad, M.U.; Ghfar, A.A.; Stadler, F.J. Quaternary Magnetic BiOCl/g-C3N4/Cu2O/Fe3O4 Nano-Junction for Visible Light and Solar Powered Degradation of Sulfamethoxazole from Aqueous Environment. *Chem. Eng. J.* **2018**, *334*, 462–478. [CrossRef]
167. Yuan, D.; Huang, L.; Li, Y.; Xu, Y.; Xu, H.; Huang, S.; Yan, J.; He, M.; Li, H. Synthesis and Photocatalytic Activity of G-C3N4/BiOI/BiOBr Ternary Composites. *RSC Adv.* **2016**, *6*, 41204–41213. [CrossRef]
168. Qu, J.; Du, Y.; Feng, Y.; Wang, J.; He, B.; Du, M.; Liu, Y.; Jiang, N. Visible-Light-Responsive K-Doped g-C3N4/BiOBr Hybrid Photocatalyst with Highly Efficient Degradation of Rhodamine B and Tetracycline. *Mater. Sci. Semicond. Process.* **2020**, *112*, 105023. [CrossRef]
169. Guo, F.; Chen, J.; Zhao, J.; Chen, Z.; Xia, D.; Zhan, Z.; Wang, Q. Z-Scheme Heterojunction g-C3N4@PDA/BiOBr with Biomimetic Polydopamine as Electron Transfer Mediators for Enhanced Visible-Light Driven Degradation of Sulfamethoxazole. *Chem. Eng. J.* **2020**, *386*, 124014. [CrossRef]
170. Li, H.; Ai, Z.; Zhang, L. Surface Structure-Dependent Photocatalytic O2 Activation for Pollutant Removal with Bismuth Oxyhalides. *Chem. Commun.* **2020**, *56*, 15282. [CrossRef]
171. Ye, L.; Jin, X.; Ji, X.; Liu, C.; Su, Y.; Xie, H.; Liu, C. Facet-Dependent Photocatalytic Reduction of CO2 on BiOI Nanosheets. *Chem. Eng. J.* **2016**, *291*, 39–46. [CrossRef]
172. Ye, L.; Wang, H.; Jin, X.; Su, Y.; Wang, D.; Xie, H.; Liu, X.; Liu, X. Synthesis of Olive-Green Few-Layered BiOI for Efficient Photoreduction of CO2 into Solar Fuels under Visible/near-Infrared Light. *Sol. Energy Mater. Sol. Cells* **2016**, *144*, 732–739. [CrossRef]
173. Yu, H.; Huang, H.; Xu, K.; Hao, W.; Guo, Y.; Wang, S.; Shen, X.; Pan, S.; Zhang, Y. Liquid-Phase Exfoliation into Monolayered BiOBr Nanosheets for Photocatalytic Oxidation and Reduction. *ACS Sustain. Chem. Eng.* **2017**, *5*, 10499–10508. [CrossRef]
174. Kong, X.Y.; Ng, B.J.; Tan, K.H.; Chen, X.; Wang, H.; Mohamed, A.R.; Chai, S.P. Simultaneous Generation of Oxygen Vacancies on Ultrathin BiOBr Nanosheets during Visible-Light-Driven CO2 Photoreduction Evoked Superior Activity and Long-Term Stability. *Catal. Today* **2018**, *314*, 20–27. [CrossRef]
175. Kong, X.Y.; Lee, W.P.C.; Ong, W.-J.; Chai, S.-P.; Mohamed, A.R. Oxygen-Deficient BiOBr as a Highly Stable Photocatalyst for Efficient CO_2 Reduction into Renewable Carbon-Neutral Fuels. *ChemCatChem* **2016**, *8*, 3074–3081. [CrossRef]
176. Gao, M.; Yang, J.; Sun, T.; Zhang, Z.; Zhang, D.; Huang, H.; Lin, H.; Fang, Y.; Wang, X. Persian Buttercup-like BiOBrxCl1-x Solid Solution for Photocatalytic Overall CO2 Reduction to CO and O2. *Appl. Catal. B Environ.* **2019**, *243*, 734–740. [CrossRef]
177. Jin, J.; Wang, Y.; He, T. Preparation of Thickness-Tunable BiOCl Nanosheets with High Photocatalytic Activity for Photoreduction of CO2. *RSC Adv.* **2015**, *5*, 100244–100250. [CrossRef]
178. Ma, Z.; Li, P.; Ye, L.; Zhou, Y.; Su, F.; Ding, C.; Xie, H.; Bai, Y.; Wong, P.K. Oxygen Vacancies Induced Exciton Dissociation of Flexible BiOCl Nanosheets for Effective Photocatalytic CO2 Conversion. *J. Mater. Chem. A* **2017**, *5*, 24995–25004. [CrossRef]
179. Zhang, L.; Wang, W.; Jiang, D.; Gao, E.; Sun, S. Photoreduction of CO2 on BiOCl Nanoplates with the Assistance of Photoinduced Oxygen Vacancies. *Nano Res.* **2015**, *8*, 821–831. [CrossRef]
180. Bai, Y.; Yang, P.; Wang, P.; Xie, H.; Dang, H.; Ye, L. Semimetal Bismuth Mediated UV–Vis-IR Driven Photo-Thermocatalysis of Bi4O5I2 for Carbon Dioxide to Chemical Energy. *J. Co2 Util.* **2018**, *23*, 51–60. [CrossRef]
181. Ye, L.; Jin, X.; Liu, C.; Ding, C.; Xie, H.; Chu, K.H.; Wong, P.K. Thickness-Ultrathin and Bismuth-Rich Strategies for BiOBr to Enhance Photoreduction of CO_2 into Solar Fuels. *Appl. Catal. B Environ.* **2016**, *187*, 281–290. [CrossRef]
182. Bai, Y.; Yang, P.; Wang, L.; Yang, B.; Xie, H.; Zhou, Y.; Ye, L. Ultrathin Bi4O5Br2 Nanosheets for Selective Photocatalytic CO2 Conversion into CO. *Chem. Eng. J.* **2019**, *360*, 473–482. [CrossRef]
183. Ding, C.; Ye, L.; Zhao, Q.; Zhong, Z.; Liu, K.; Xie, H.; Bao, K.; Zhang, X.; Huang, Z. Synthesis of BixOyIz from Molecular Precursor and Selective Photoreduction of CO_2 into CO. *J. Co2 Util.* **2016**, *14*, 135–142. [CrossRef]
184. Bai, Y.; Ye, L.; Wang, L.; Shi, X.; Wang, P.; Bai, W.; Wong, P.K. G-C_3N_4/$Bi_4O_5I_2$ Heterojunction with I3-/I- Redox Mediator for Enhanced Photocatalytic CO2 Conversion. *Appl. Catal. B Environ.* **2016**, *194*, 98–104. [CrossRef]
185. Wang, J.-C.; Yao, H.-C.; Fan, Z.-Y.; Zhang, L.; Wang, J.-S.; Zang, S.-Q.; Li, Z.-J. Indirect Z-Scheme BiOI/g-C_3N_4 Photocatalysts with Enhanced Photoreduction CO2 Activity under Visible Light Irradiation. *ACS Appl. Mater. Interfaces* **2016**, *8*, 3765–3775. [CrossRef] [PubMed]
186. Chen, Y.; Wang, F.; Cao, Y.; Zhang, F.; Zou, Y.; Huang, Z.; Ye, L.; Zhou, Y. Interfacial Oxygen Vacancy Engineered Two-Dimensional g-C3N4/BiOCl Heterostructures with Boosted Photocatalytic Conversion of CO2. *ACS Appl. Energy Mater.* **2020**. [CrossRef]
187. Ayyub, M.M.; Singh, R.; Rao, C.N.R. Hydrogen Generation by Solar Water Splitting Using 2D Nanomaterials. *Sol. Rrl* **2020**, *4*, 2000050. [CrossRef]
188. Pan, H.X.; Feng, L.P.; Zeng, W.; Zhang, Q.C.; Zhang, X.D.; Liu, Z.T. Active Sites in Single-Layer BiOX (X = Cl, Br, and I) Catalysts for the Hydrogen Evolution Reaction. *Inorg. Chem.* **2019**, *58*, 13195–13202. [CrossRef]
189. Fang, W.; Shangguan, W. A Review on Bismuth-Based Composite Oxides for Photocatalytic Hydrogen Generation. *Int. J. Hydrog. Energy* **2019**, *44*, 895–912. [CrossRef]
190. Jin, X.; Ye, L.; Xie, H.; Chen, G. Bismuth-Rich Bismuth Oxyhalides for Environmental and Energy Photocatalysis. *Coord. Chem. Rev.* **2017**, *349*, 84–101. [CrossRef]
191. Ye, L.; Jin, X.; Leng, Y.; Su, Y.; Xie, H.; Liu, C. Synthesis of Black Ultrathin BiOCl Nanosheets for Efficient Photocatalytic H2 Production under Visible Light Irradiation. *J. Power Sources* **2015**, *293*, 409–415. [CrossRef]

192. Li, M.; Yu, S.; Huang, H.; Li, X.; Feng, Y.; Wang, C.; Wang, Y.; Ma, T.; Guo, L.; Zhang, Y. Unprecedented Eighteen-Faceted BiOCl with a Ternary Facet Junction Boosting Cascade Charge Flow and Photo-redox. *Angew. Chem. Int. Ed.* **2019**, *58*, 9517–9521. [CrossRef]
193. Lee, G.J.; Zheng, Y.C.; Wu, J.J. Fabrication of Hierarchical Bismuth Oxyhalides (BiOX, X = Cl, Br, I) Materials and Application of Photocatalytic Hydrogen Production from Water Splitting. *Catal. Today* **2018**, *307*, 197–204. [CrossRef]
194. Li, J.; Zhan, G.; Yu, Y.; Zhang, L. Superior Visible Light Hydrogen Evolution of Janus Bilayer Junctions via Atomic-Level Charge Flow Steering. *Nat. Commun.* **2016**, *7*, 11480. [CrossRef] [PubMed]
195. Li, Y.F.; Liu, Z.P.; Liu, L.; Gao, W. Mechanism and Activity of Photocatalytic Oxygen Evolution on Titania Anatase in Aqueous Surroundings. *J. Am. Chem. Soc.* **2010**, *132*, 13008–13015. [CrossRef]
196. Di, J.; Chen, C.; Yang, S.Z.; Ji, M.; Yan, C.; Gu, K.; Xia, J.; Li, H.; Li, S.; Liu, Z. Defect Engineering in Atomically-Thin Bismuth Oxychloride towards Photocatalytic Oxygen Evolution. *J. Mater. Chem. A* **2017**, *5*, 14144–14151. [CrossRef]
197. Bai, L.; Ye, F.; Li, L.; Lu, J.; Zhong, S.; Bai, S. Facet Engineered Interface Design of Plasmonic Metal and Cocatalyst on BiOCl Nanoplates for Enhanced Visible Photocatalytic Oxygen Evolution. *Small* **2017**, *13*, 1701607. [CrossRef] [PubMed]
198. Cui, D.; Wang, L.; Xu, K.; Ren, L.; Weng, L.; Yu, Y.; Du, Y.; Hao, W. Band-Gap Engineering of BiOCl with Oxygen Vacancies for Efficient Photooxidation Properties under Visible-Light Irradiation. *J. Mater. Chem. A* **2018**, *6*, 2193–2199. [CrossRef]
199. Ji, M.; Chen, R.; Di, J.; Liu, Y.; Li, K.; Chen, Z.; Xia, J.; Li, H. Oxygen Vacancies Modulated Bi-Rich Bismuth Oxyiodide Microspheres with Tunable Valence Band Position to Boost the Photocatalytic Activity. *J. Colloid Interface Sci.* **2019**, *533*, 612–620. [CrossRef]
200. Xiong, X.; Zhou, T.; Liu, X.; Ding, S.; Hu, J. Surfactant-Mediated Synthesis of Single-Crystalline Bi3O4Br Nanorings with Enhanced Photocatalytic Activity. *J. Mater. Chem. A* **2017**, *5*, 15706–15713. [CrossRef]
201. Ning, S.; Shi, X.; Zhang, H.; Lin, H.; Zhang, Z.; Long, J.; Li, Y.; Wang, X. Reconstructing Dual-Induced {0 0 1} Facets Bismuth Oxychloride Nanosheets Heterostructures: An Effective Strategy to Promote Photocatalytic Oxygen Evolution. *Sol. RRL* **2019**, *3*, 1900059. [CrossRef]
202. Dong, G.; Jacobs, D.L.; Zang, L.; Wang, C. Carbon Vacancy Regulated Photoreduction of NO to N2 over Ultrathin G-C3N4 Nanosheets. *Appl. Catal. B Environ.* **2017**, *218*, 515–524. [CrossRef]
203. Ye, C.; Li, J.X.; Li, Z.J.; Li, X.B.; Fan, X.B.; Zhang, L.P.; Chen, B.; Tung, C.H.; Wu, L.Z. Enhanced Driving Force and Charge Separation Efficiency of Protonated G-C3N4 for Photocatalytic O2 Evolution. *ACS Catal.* **2015**, *5*, 6973–6979. [CrossRef]
204. Zhang, J.; Grzelczak, M.; Hou, Y.; Maeda, K.; Domen, K.; Fu, X.; Antonietti, M.; Wang, X. Photocatalytic Oxidation of Water by Polymeric Carbon Nitride Nanohybrids Made of Sustainable Elements. *Chem. Sci.* **2012**, *3*, 443–446. [CrossRef]
205. Li, H.; Shang, J.; Ai, Z.; Zhang, L. Efficient Visible Light Nitrogen Fixation with BiOBr Nanosheets of Oxygen Vacancies on the Exposed {001} Facets. *J. Am. Chem. Soc.* **2015**, *137*, 6393–6399. [CrossRef] [PubMed]
206. Li, H.; Shang, J.; Shi, J.; Zhao, K.; Zhang, L. Facet-Dependent Solar Ammonia Synthesis of BiOCl Nanosheets via a Proton-Assisted Electron Transfer Pathway. *Nanoscale* **2016**, *8*, 1986–1993. [CrossRef]
207. Bai, Y.; Ye, L.; Chen, T.; Wang, L.; Shi, X.; Zhang, X.; Chen, D. Facet-Dependent Photocatalytic N2 Fixation of Bismuth-Rich Bi5O7I Nanosheets. *Acs Appl. Mater. Interfaces* **2016**, *8*, 27661–27668. [CrossRef]
208. Zhang, N.; Li, L.; Shao, Q.; Zhu, T.; Huang, X.; Xiao, X. Fe-Doped BiOCl Nanosheets with Light-Switchable Oxygen Vacancies for Photocatalytic Nitrogen Fixation. *Acs Appl. Energy Mater.* **2019**, *2*, 8394–8398. [CrossRef]
209. Liu, Y.; Hu, Z.; Yu, J.C. Fe Enhanced Visible-Light-Driven Nitrogen Fixation on Biobr Nanosheets. *Chem. Mater.* **2020**, *32*, 1488–1494. [CrossRef]
210. Cao, S.; Fan, B.; Feng, Y.; Chen, H.; Jiang, F.; Wang, X. Sulfur-Doped g-C3N4 Nanosheets with Carbon Vacancies: General Synthesis and Improved Activity for Simulated Solar-Light Photocatalytic Nitrogen Fixation. *Chem. Eng. J.* **2018**, *353*, 147–156. [CrossRef]
211. Xue, Y.; Guo, Y.; Liang, Z.; Cui, H.; Tian, J. Porous G-C3N4 with Nitrogen Defects and Cyano Groups for Excellent Photocatalytic Nitrogen Fixation without Co-Catalysts. *J. Colloid Interface Sci.* **2019**, *556*, 206–213. [CrossRef]
212. Xiao, X.; Jiang, J.; Zhang, L. Selective Oxidation of Benzyl Alcohol into Benzaldehyde over Semiconductors under Visible Light: The Case of Bi12O17Cl2 Nanobelts. *Appl. Catal. B Environ.* **2013**, *142–143*, 487–493. [CrossRef]
213. Han, A.; Zhang, H.; Chuah, G.K.; Jaenicke, S. Influence of the Halide and Exposed Facets on the Visible-Light Photoactivity of Bismuth Oxyhalides for Selective Aerobic Oxidation of Primary Amines. *Appl. Catal. B Environ.* **2017**, *219*, 269–275. [CrossRef]
214. Wang, H.; Yong, D.; Chen, S.; Jiang, S.; Zhang, X.; Shao, W.; Zhang, Q.; Yan, W.; Pan, B.; Xie, Y. Oxygen-Vacancy-Mediated Exciton Dissociation in Biobr for Boosting Charge-Carrier-Involved Molecular Oxygen Activation. *J. Am. Chem. Soc.* **2018**, *140*, 1760–1766. [CrossRef] [PubMed]
215. Wu, Y.; Yuan, B.; Li, M.; Zhang, W.H.; Liu, Y.; Li, C. Well-Defined BiOCl Colloidal Ultrathin Nanosheets: Synthesis, Characterization, and Application in Photocatalytic Aerobic Oxidation of Secondary Amines. *Chem. Sci.* **2015**, *6*, 1873–1878. [CrossRef] [PubMed]
216. Dai, Y.; Ren, P.; Li, Y.; Lv, D.; Shen, Y.; Li, Y.; Niemantsverdriet, H.; Besenbacher, F.; Xiang, H.; Hao, W.; et al. Solid Base Bi24O31Br10(OH)δ with Active Lattice Oxygen for the Efficient Photo-Oxidation of Primary Alcohols to Aldehydes. *Angew. Chem. Int. Ed.* **2019**, *58*, 6265–6270. [CrossRef]
217. Juntrapirom, S.; Anuchai, S.; Thongsook, O.; Pornsuwan, S.; Meepowpan, P.; Thavornyutikarn, P.; Phanichphant, S.; Tantraviwat, D.; Inceesungvorn, B. Photocatalytic Activity Enhancement of G-C3N4/BiOBr in Selective Transformation of Primary Amines to Imines and Its Reaction Mechanism. *Chem. Eng. J.* **2020**, *394*, 124934. [CrossRef]

218. Liu, D.; Chen, D.; Li, N.; Xu, Q.; Li, H.; He, J.; Lu, J. Surface Engineering of G-C3N4 by Stacked BiOBr Sheets Rich in Oxygen Vacancies for Boosting Photocatalytic Performance. *Angew. Chem. Int. Ed.* **2020**, *59*, 4519–4524. [CrossRef]
219. Ye, L.; Zan, L.; Tian, L.; Peng, T.; Zhang, J. The {001} Facets-Dependent High Photoactivity of BiOCl Nanosheets. *Chem. Commun.* **2011**, *47*, 6951–6953. [CrossRef]
220. Jiang, J.; Zhao, K.; Xiao, X.; Zhang, L. Synthesis and Facet-Dependent Photoreactivity of BiOCl Single-Crystalline Nanosheets. *J. Am. Chem. Soc.* **2012**, *134*, 4473–4476. [CrossRef]
221. Zhao, Y.; Yu, T.; Tan, X.; Xie, C.; Wang, S. SDS-Assisted Solvothermal Synthesis of Rose-like BiOBr Partially Enclosed by {111} Facets and Enhanced Visible-Light Photocatalytic Activity. *Dalton Trans.* **2015**, *44*, 20475–20483. [CrossRef]
222. Peng, Y.; Xu, J.; Liu, T.; Mao, Y.G. Controlled Synthesis of One-Dimensional BiOBr with Exposed (110) Facets and Enhanced Photocatalytic Activity. *CrystEngComm* **2017**, *19*, 6473–6480. [CrossRef]
223. Ye, L.; Deng, K.; Xu, F.; Tian, L.; Peng, T.; Zan, L. Increasing Visible-Light Absorption for Photocatalysis with Black BiOCl. *Phys. Chem. Chem. Phys.* **2012**, *14*, 82–85. [CrossRef]
224. Wang, X.J.; Zhao, Y.; Li, F.T.; Dou, L.J.; Li, Y.P.; Zhao, J.; Hao, Y.J. A Chelation Strategy for In-Situ Constructing Surface Oxygen Vacancy on {001} Facets Exposed BiOBr Nanosheets. *Sci. Rep.* **2016**, *6*, 1–11. [CrossRef] [PubMed]
225. Wu, J.; Li, X.; Shi, W.; Ling, P.; Sun, Y.; Jiao, X.; Gao, S.; Liang, L.; Xu, J.; Yan, W.; et al. Efficient Visible-Light-Driven CO_2 Reduction Mediated by Defect-Engineered BiOBr Atomic Layers. *Angew. Chem. Int. Ed.* **2018**, *57*, 8719–8723. [CrossRef] [PubMed]
226. Hu, J.; Zhai, C.; Gao, H.; Zeng, L.; Du, Y.; Zhu, M. Enhanced Photo-Assisted Ethanol Electro-Oxidation Activity by Using Broadband Visible Light Absorption of a Graphitic C3 N4 /BiOI Carrier. *Sustain. Energy Fuels* **2019**, *3*, 439–449. [CrossRef]
227. Wang, K.; Li, J.; Zhang, G. Ag-Bridged Z-Scheme 2D/2D Bi5FeTi3O15/g-C3N4 Heterojunction for Enhanced Photocatalysis: Mediator-Induced Interfacial Charge Transfer and Mechanism Insights. *Acs Appl. Mater. Interfaces* **2019**, *11*, 27686–27696. [CrossRef] [PubMed]
228. Zhang, J.; Wang, Z.; Fan, M.; Tong, P.; Sun, J.; Dong, S.; Sun, J. Ultra-Light and Compressible 3D BiOCl/RGO Aerogel with Enriched Synergistic Effect of Adsorption and Photocatalytic Degradation of Oxytetracycline. *J. Mater. Res. Technol.* **2019**, *8*, 4577–4587. [CrossRef]
229. Di, J.; Xia, J.; Ji, M.; Wang, B.; Yin, S.; Zhang, Q.; Chen, Z.; Li, H. Carbon Quantum Dots Modified BiOCl Ultrathin Nanosheets with Enhanced Molecular Oxygen Activation Ability for Broad Spectrum Photocatalytic Properties and Mechanism Insight. *Acs Appl. Mater. Interfaces* **2015**, *7*, 20111–20123. [CrossRef] [PubMed]
230. Huang, J.; Chen, W.; Yu, X.; Fu, X.; Zhu, Y.; Zhang, Y. Fabrication of a Ternary BiOCl/CQDs/RGO Photocatalyst: The Roles of CQDs and RGO in Adsorption-Photocatalytic Removal of Ciprofloxacin. *Colloids Surf. A Physicochem. Eng. Asp.* **2020**, *597*, 124758. [CrossRef]
231. Yu, X.; Shi, J.; Feng, L.; Li, C.; Wang, L. A Three-Dimensional BiOBr/RGO Heterostructural Aerogel with Enhanced and Selective Photocatalytic Properties under Visible Light. *Appl. Surf. Sci.* **2017**, *396*, 1775–1782. [CrossRef]
232. Allagui, L.; Chouchene, B.; Gries, T.; Medjahdi, G.; Girot, E.; Framboisier, X.; Amara, A.B.H.; Balan, L.; Schneider, R. Core/Shell RGO/BiOBr Particles with Visible Photocatalytic Activity towards Water Pollutants. *Appl. Surf. Sci.* **2019**, *490*, 580–591. [CrossRef]
233. Xue, J.; Li, X.; Ma, S.; Xu, P.; Wang, M.; Ye, Z. Facile Fabrication of BiOCl/RGO/Protonated g-C3N4 Ternary Nanocomposite as Z-Scheme Photocatalyst for Tetracycline Degradation and Benzyl Alcohol Oxidation. *J. Mater. Sci.* **2019**, *54*, 1275–1290. [CrossRef]
234. Huang, H.; Liu, C.; Ou, H.; Ma, T.; Zhang, Y. Self-Sacrifice Transformation for Fabrication of Type-I and Type-II Heterojunctions in Hierarchical Bi x O y I z /g-C3 N4 for Efficient Visible-Light Photocatalysis. *Appl. Surf. Sci.* **2019**, *470*, 1101–1110. [CrossRef]
235. Low, J.; Jiang, C.; Cheng, B.; Wageh, S.; Al-Ghamdi, A.A.; Yu, J. A Review of Direct Z-Scheme Photocatalysts. *Small Methods* **2017**, *1*, 1700080. [CrossRef]
236. Zhou, P.; Yu, J.; Jaroniec, M. All-Solid-State Z-Scheme Photocatalytic Systems. *Adv. Mater.* **2014**, *26*, 4920–4935. [CrossRef]
237. Liang, Q.; Cui, S.; Jin, J.; Liu, C.; Xu, S.; Yao, C.; Li, Z. Fabrication of BiOI@UIO-66(NH_2)@g-C3 N4 Ternary Z-Scheme Heterojunction with Enhanced Visible-Light Photocatalytic Activity. *Appl. Surf. Sci.* **2018**, *456*, 899–907. [CrossRef]
238. Liang, S.; He, M.; Guo, J.; Yue, J.; Pu, X.; Ge, B.; Li, W. Fabrication and Characterization of BiOBr:Yb3+,Er3+/g-C3N4 p-n Junction Photocatalysts with Enhanced Visible-NIR-Light-Driven Photoactivities. *Sep. Purif. Technol.* **2018**, *206*, 69–79. [CrossRef]
239. Bai, Y.; Wang, P.Q.; Liu, J.Y.; Liu, X.J. Enhanced Photocatalytic Performance of Direct Z-Scheme BiOCl-g-C3N4 Photocatalysts. *Rsc Adv.* **2014**, *4*, 19456–19461. [CrossRef]
240. Zhao, W.; Wang, W.; Shi, H. 2D/2D Z-Scheme BiO1-XBr/g-C3N4 Heterojunction with Rich Oxygen Vacancies as Electron Mediator for Enhanced Visible-Light Degradation Activity. *Appl. Surf. Sci.* **2020**, *528*, 146925. [CrossRef]
241. Tang, Z.K.; Yin, W.J.; Zhang, L.; Wen, B.; Zhang, D.Y.; Liu, L.M.; Lau, W.M. Spatial Separation of Photo-Generated Electron-Hole Pairs in BiOBr/BiOI Bilayer to Facilitate Water Splitting. *Sci. Rep.* **2016**, *6*, 1–9. [CrossRef] [PubMed]
242. Tu, W.; Xu, Y.; Wang, J.; Zhang, B.; Zhou, T.; Yin, S.; Wu, S.; Li, C.; Huang, Y.; Zhou, Y.; et al. Investigating the Role of Tunable Nitrogen Vacancies in Graphitic Carbon Nitride Nanosheets for Efficient Visible-Light-Driven H2 Evolution and CO2 Reduction. *ACS Sustain. Chem. Eng.* **2017**, *5*, 7260–7268. [CrossRef]
243. Huang, Y.; Liu, J.; Zhao, C.; Jia, X.; Ma, M.; Qian, Y.; Yang, C.; Liu, K.; Tan, F.; Wang, Z.; et al. Facile Synthesis of Defect-Modified Thin-Layered and Porous g-C3N4with Synergetic Improvement for Photocatalytic H2Production. *ACS Appl. Mater. Interfaces* **2020**. [CrossRef] [PubMed]

244. Jiang, Y.; Sun, Z.; Tang, C.; Zhou, Y.; Zeng, L.; Huang, L. Enhancement of Photocatalytic Hydrogen Evolution Activity of Porous Oxygen Doped G-C3N4 with Nitrogen Defects Induced by Changing Electron Transition. *Appl. Catal. B Environ.* **2019**, *240*, 30–38. [CrossRef]
245. Ruan, D.; Kim, S.; Fujitsuka, M.; Majima, T. Defects Rich G-C3N4 with Mesoporous Structure for Efficient Photocatalytic H2 Production under Visible Light Irradiation. *Appl. Catal. B Environ.* **2018**, *238*, 638–646. [CrossRef]
246. Zhao, D.; Dong, C.; Wang, B.; Chen, C.; Huang, Y.; Diao, Z.; Li, S.; Guo, L.; Shen, S. Synergy of Dopants and Defects in Graphitic Carbon Nitride with Exceptionally Modulated Band Structures for Efficient Photocatalytic Oxygen Evolution. *Adv. Mater.* **2019**, *31*, 1903545. [CrossRef] [PubMed]
247. Shiraishi, Y.; Shiota, S.; Kofuji, Y.; Hashimoto, M.; Chishiro, K.; Hirakawa, H.; Tanaka, S.; Ichikawa, S.; Hirai, T. Nitrogen Fixation with Water on Carbon-Nitride-Based Metal-Free Photocatalysts with 0.1% Solar-to-Ammonia Energy Conversion Efficiency. *ACS Appl. Energy Mater.* **2018**, *1*, 4169–4177. [CrossRef]
248. Hao, D.; Liu, C.; Xu, X.; Kianinia, M.; Aharonovich, I.; Bai, X.; Liu, X.; Chen, Z.; Wei, W.; Jia, G.; et al. Surface Defect-Abundant One-Dimensional Graphitic Carbon Nitride Nanorods Boost Photocatalytic Nitrogen Fixation. *New J. Chem.* **2020**, *44*, 20651. [CrossRef]